Università degli Studi dell'Insubria

Dipartimento di Scienza e Alta Tecnologia
Master Degree in Physics

Characterization of an Oriented Crystal-Based Calorimeter Prototype

CERN-THESIS-2024-110
18/07/2024

Author:
Giulia Lezzani

Supervisor:
Prof.ssa Michela Prest

Co-supervisor:
Dr.ssa Alessia Selmi

Academic Year 2023-2024

Take a sad song and make it better.

Contents

Introduction

Electromagnetic calorimeters are vital components in High-Energy Physics (HEP) experiments, designed to measure the energy of particles such as electrons and photons. These detectors operate by absorbing the whole energy of the incident particles and converting it into detectable signals. Homogeneous electromagnetic calorimeters, in particular, consist of a single type of material that acts as both the absorber and the active medium, providing a high degree of uniformity and potentially better energy resolution compared to sampling calorimeters. Among the available choices of detector materials, inorganic scintillators are the most appealing option in HEP, due to their high density and atomic number Z.

A promising approach to improving the performance of homogeneous electromagnetic calorimeters involves the use of oriented crystalline materials. Crystals with a well-ordered structure can significantly influence the behavior of high-energy particles thanks to a phenomenon known as *channeling*. When charged particles cross specific crystallographic planes or axes, they experience reduced scattering and energy loss compared to the passage through amorphous materials.

The concept of channeling was initially proposed by Johannes Stark in 1912 and later validated in the 1960s through theoretical and experimental studies. The Jens Lindhard theoretical framework provided a comprehensive understanding of how coherent scattering with lattice atoms confines particles within the crystal, thereby modifying their energy dissipation patterns. The observation of channeling radiation in 1986 at the Lawrence Livermore Laboratory further demonstrated the potential of using crystals to control particle trajectories and radiation emission. The periodic motion of particles within the crystal lattice results in the coherent emission of photons, with characteristics that vary significantly based on the initial energy of the charged particles. For electrons or positrons with a low initial energy ($\sim 100\,\mathrm{MeV}$), the emitted spectrum resembles that of electric dipole radiation, producing soft photons with quantized frequencies. As the energy increases to a few GeV, the emission behavior moves to an undulator-like pattern and, at even higher energies, it exhibits synchrotron-like characteristics, leading to the emission of hard photons.

At energies exceeding a few GeV, relativistic effects become significant. The interatomic electric field experienced by an impinging electron is amplified by the Lorentz factor γ and the so-called Strong Field regime is reached. In this regime, also the pair production cross section is altered, increasing the rate of pair production when a photon interacts with the crystal lattice. Consequently, the Strong Field regime enhances the energy deposit and accelerates the development of the electromagnetic shower. This effect can be equivalently described as a reduction in the radiation length X_0 of the crystal compared to amorphous materials. The reduction of the effective radiation length in oriented crystals can be employed to develop a compact electromagnetic calorimeter

This thesis work has been performed within the framework of the INFN OREO (ORiEnted calOrimeter) project, which aims at developing a highly compact electromagnetic calorimeter based on oriented crystals, significantly reducing the material, volume and weight compared to state-of-the-art detectors. In August 2023, two beamtests were performed on the CERN T9 and H2 beamline at CERN to test the initial prototype, consisting of three $PbWO_4$ ultrafast crystals arranged in a row, read out by Silicon PhotoMultipliers (SiPMs).

In the first chapter, a theoretical framework of the effects induced by the crystal lattice on an impinging particle will be provided, including a brief introduction to crystal structures, followed by detailed discussions on the channeling phenomena. Moreover, the radiation emission mechanisms induced by the crystal lattice will be examined. Finally, the chapter will focus on the Strong Field regime and its effects on pair production and shower development.

After introducing homogeneous electromagnetic calorimeters and their main features, the second chapter will present the OREO project. An overview of the experimental methodologies used in the study of oriented crystals will be provided, along with the specific goals and innovations of the OREO project. Potential applications of oriented calorimeters in high-energy physics and satellite-borne experiments will be highlighted.

The third chapter will present the beamtests performed at CERN in 2023. The first part will outline the goals of these tests and provide a comprehensive overview of the prototype, including the crystal samples and the photodetectors system. The second part will discuss the beam facilities and experimental setups in detail.

In the fourth chapter, the preliminary data analysis will be presented: the alignment of the silicon tracker, the characterization of the particle beams, the evaluation of the Cherenkov counters performance, the calibration of the Lead Glass calorimeter and the alignment procedure of the crystals.

Chapter five will focus on the characterization of the OREO layer. The first part will describe the calibration procedures for the SiPMs, necessary to convert the signal from arbitrary units to GeV. The second part will present the study of the energy deposit enhancement in the axial orientation compared to the random one. First, the enhancement will be examined in each of the three crystals to understand their relative alignment. Then it will be analyzed as a function of the energy and the misalignment angles, considering the whole layer. Finally, a preliminary estimate of the prototype energy resolution will be provided.

Chapter 1

The Physics of Oriented Crystals

When a beam of charged particles interacts with a block of material, several phenomena may occur, including scattering, absorption and ionization. These interactions depend on the energy of the particles and the composition of the material. However, when the material has a crystalline structure, the interaction dynamics becomes more complex. The key element in this case is the angle between the direction of the particle and the symmetry axis of the crystal lattice, which influences the physics of the interaction.

Stark was the first to suggest these effects, now known as *channeling*. In 1912, he hypothesized that in a crystal, certain directions might be more transparent to the passage of charged particles compared to what occurs in an amorphous material [1]. At the beginning, the channeling of charged particles in crystals was overlooked, but it regained the stage in the early 1960s, due to computer simulations [2] and experimental studies [3], which revealed anomalously long ion ranges in crystals.

During the 1960s, Lindhard provided a theoretical framework for channeling, demonstrating that the particle confinement results from the coherent scattering with the crystal lattice [4]. These effects were predicted to significantly diminish the yield of nuclear reactions between the incident particle and the atomic nuclei, a forecast promptly validated by experiments [5, 6].

In 1986, at the Lawrence Livermore Laboratory, the phenomenon now known as *channeling radiation* was first observed. This phenomenon occurred during an experiment where electrons and positrons, with energies of 16 and 28 MeV respectively, impinged on an axially oriented silicon crystal [7].

The properties of channeling radiation, which were theoretically predicted by Kumakhov [8] and Terhune and Pantell [9] in the mid-1970s, generated a significant interest and stimulated several experimental investigations at various laboratories.

In this chapter, the phenomenon of channeling and the radiative processes resulting from electrons/positrons and photons interacting within oriented crystals will be discussed. For a complete description see [1, 10, 11].

1.1 The Crystalline Lattice

A crystal is a solid characterized by a regular three-dimensional lattice, also known as a crystalline lattice or Bravais lattice, in which atoms, molecules, or ions are arranged in an orderly and repetitive way. This regular order extends in all directions in space, providing specific properties to the crystal such as transparency and hardness.

A Bravais lattice consists in an infinite array of discrete points generated by a set of discrete translation operations described in a three dimensional space by:

$$\boldsymbol{R} = n_1\boldsymbol{a}_1 + n_2\boldsymbol{a}_2 + n_3\boldsymbol{a}_3$$

where $\boldsymbol{a}_1$, $\boldsymbol{a}_2$ and $\boldsymbol{a}_3$ are any three vectors not all in the same plane, and n_1, n_2 and n_3 are integer values. The $\boldsymbol{a}_i$ vectors are called primitive vectors and are said to generate or span the lattice. An equivalent definition of a Bravais lattice is that it is an infinite array of discrete points with an arrangement and orientation that appears exactly the same, from whichever of the points the array is viewed. There are 14 possible Bravais lattices in the 3-dimensional space [12].

To describe the channeling phenomenon, two subsets of crystal nodes are essential: planes and axes (or strings). Given a particular Bravais lattice, a lattice plane is defined to be any plane containing at least three non collinear Bravais lattice points [12]. To describe a lattice plane, one can use the Miller indices, which are the coordinates of the shortest reciprocal lattice vector normal to that plane, with respect to a specified set of primitive reciprocal lattice vectors. Thus a plane with Miller indices $(h,\ k,\ l)$ is normal to the reciprocal lattice vector $h\boldsymbol{b}_1 + k\boldsymbol{b}_2 + l\boldsymbol{b}_3$. Note that the Miller indices depend on the particular choice of primitive vectors.

It is possible to derive the Miller indices starting from the plane equation:

$$\frac{n_a}{a_0} + \frac{n_b}{b_0} + \frac{n_c}{c_0} = 1 \tag{1.1}$$

where n_a, n_b and n_c are the nodes coordinates, in units of the lattice constant, and $a,\ b,\ c$ are the coordinates of the intersections between the plane and the coordinate axes. Since n_a, n_b and n_c are integers, it is possible

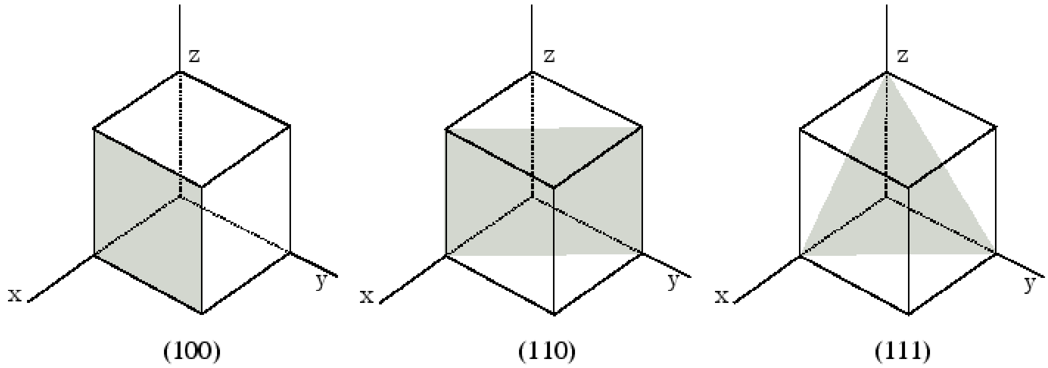

Figure 1.1: Three planes in a cubic crystal system along with their Miller indices [13].

to define four integer numbers (n, h, k, l) such that:

$$\frac{n}{n_a} = h, \qquad \frac{n}{n_b} = k, \qquad \frac{n}{n_c} = l \tag{1.2}$$

By substituting the relations (1.2), equation (1.1) becomes

$$n_a h + n_b k + n_c l = n$$

where (h, k, l) are the Miller indices. The following notation can be adopted to indicate planes and axes:

- (hkl) denotes a plane;
- [hkl] denotes all the axes which are orthogonal to the (hkl) plane;
- <hkl> denotes all the axes which are identical to [hkl], under global rotations.

Figure 1.1 presents the Miller notation corresponding to the main axes and planes of a cubic crystal system.

Considering an external observer, a crystal can have different orientations. In figure 1.2b, the lattice is oriented according to the planes, while in figure 1.2c it is oriented according to the axes. In figure 1.2a, all the main axes and planes are oriented at a large angle with respect to the external observer. This condition is called *random* because the lattice appears and behaves as if it has an unordered structure, that is, as an *amorphous* medium.

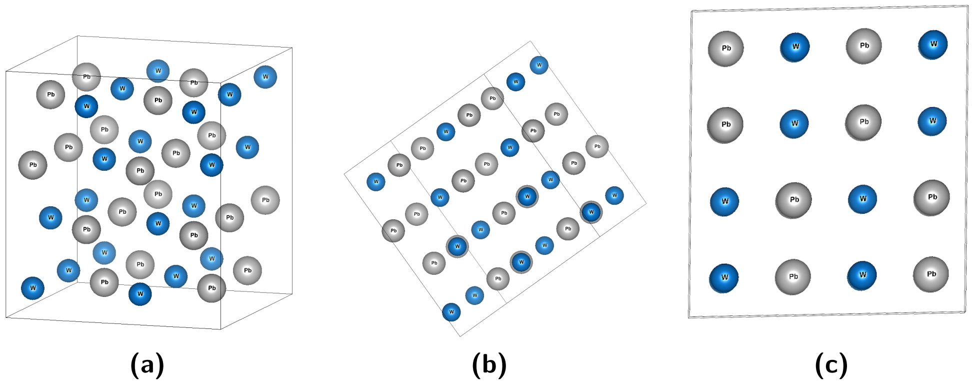

Figure 1.2: Different orientations of the $PbWO_4$ crystal lattice as seen by an external observer: **(a)** amorphous-like, **(b)** arranged in planes, **(c)** arranged in strings [14].

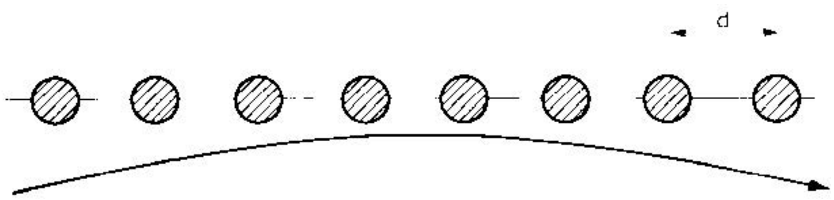

Figure 1.3: Trajectory of a charged particle governed by correlated collisions with a string of atoms [11].

1.2 The Channeling Phenomenon

In this section, the phenomenon of channeling will be explored, with particular attention to axial channeling of positively charged particles. The analysis will begin by examining the so-called *continuum approximation*, which can be used to understand and model the particle behavior within an oriented crystal.

Then, planar channeling and its features compared to axial channeling will be investigated. Moreover, a comparison between the behavior of positively charged particles and negatively charged particles will be performed.

1.2.1 Axial Channeling

Directional effects in aligned single crystals stem from the correlated series of soft collisions experienced by particles crossing the material. In this discussion, positively charged incident particles will be considered. A comparison with negatively charged particles will be made in section 1.2.3.

As shown by Lindhard, the classical frameworks provide insights into how the crystal lattice affects ion trajectories. When a charged particle strikes an aligned single crystal, its path is influenced by correlated collisions with aligned atoms, as depicted in figure 1.3. The particle experiences a sequence of soft collisions while avoiding the harder ones, resulting in smaller deflections. When several atoms contribute, discrete deflections may be substituted by the force derived from the *continuum string potential*, obtained by integrating the atomic interaction potential:

$$U(\boldsymbol{r}_\perp) = \frac{1}{d}\int_{-\infty}^{+\infty} dz\, V(\boldsymbol{r}_\perp, z) \tag{1.3}$$

corresponding to a charge distribution smeared in the z direction; $\boldsymbol{r}_\perp = (x, y)$ is the transverse coordinate vector. The movement across the entire lattice is regulated by the continuum potential derived from the combination of potentials associated with individual strings.

The so-called *standard* expression has often been used for the screened Coulomb potential $V(\boldsymbol{r}_\perp, z)$ [11]:

$$V(\boldsymbol{r}_\perp, z) = \frac{Z_1 Z_2 e^2}{r}\left(1 - \frac{r}{(r^2 + C^2 a^2)^{1/2}}\right) \tag{1.4}$$

where Z_1 and Z_2 denote the incident particle and target (nuclear) charge, respectively, C^2 is a constant normally set equal to 3 and the screening length a is chosen as:

$$a = \frac{0.89\, a_0}{\sqrt{Z_1^{2/3} + Z_2^{2/3}}} \tag{1.5}$$

where a_0 is the Bohr radius for the hydrogen atom. By inserting expression (1.4) into equation (1.3), the standard continuum potential corresponding to a single string is obtained:

$$U(\boldsymbol{r}_\perp) = \frac{Z_1 Z_2\, e^2}{d} \log\left[1 + \left(\frac{Ca}{r_\perp}\right)^2\right] \tag{1.6}$$

The uncertainty in the position of the incident particle due to the thermal vibrations of the target atoms implies a transverse smearing in addition to the longitudinal smearing. The resulting *thermally averaged* continuum potential is computed by convolving the standard potential with a gaussian kernel, which models the thermally-induced displacements of the string atoms [10]:

$$U(\boldsymbol{r}_\perp) = \frac{Z_1\, Z_2\, e^2}{d} \log\left[1 + \frac{C^2 a^2}{|\boldsymbol{r}_\perp|^2 \rho^2/2}\right] \tag{1.7}$$

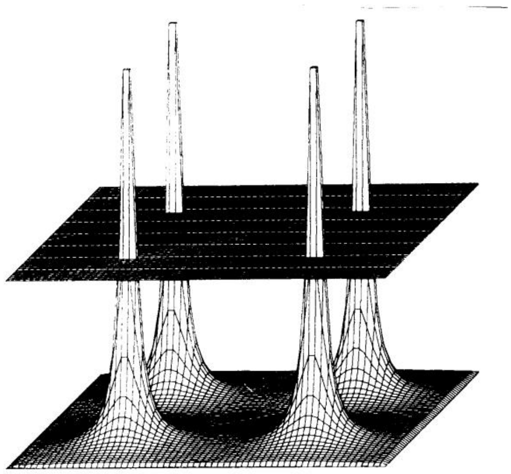

Figure 1.4: Four-string continuum potential for a <100> Cu crystal. The plane corresponds to a given fixed $E_\perp$ [16].

where ρ^2 is the two-dimensional mean square thermal displacement of the string atoms.

There are alternative potentials that may offer higher accuracy. For instance, in ion channeling, the Thomas-Fermi interaction potentials [15] with simple scaling properties are often used. Additionally, when the particle charge is small enough to be considered a perturbation, more precise Hartree-Fock calculations of atomic potentials can be applied [11].

In the non-relativistic continuum approximation, there is a complete separation between the longitudinal and transverse motion. Since the particle-string interaction potential (1.3) is independent on z, the motion parallel to the string is free, so it proceeds with a constant momentum $p_z = \boldsymbol{p}\hat{z}$, where $\boldsymbol{p}$ is the total momentum. As a consequence, the translational energy E_z associated with the longitudinal motion of a particle of mass M, $E_z = p_z^2/2M$, is conserved. As the total particle energy E is a constant of motion along with E_z, the transverse energy is also conserved (figure 1.4):

$$E_\perp = E - E_z = \frac{p_\perp^2}{2M} + U(\boldsymbol{r}_\perp) = const \tag{1.8}$$

Since E is in general very large, compared to U, equation (1.8) may also be expressed as:

$$E_\perp = E\,\psi^2 + U(\boldsymbol{r}_\perp) = \frac{1}{2}\,p\,v\,\psi^2 + U(\boldsymbol{r}_\perp) \tag{1.9}$$

where ψ denotes the local angle with respect to the string.

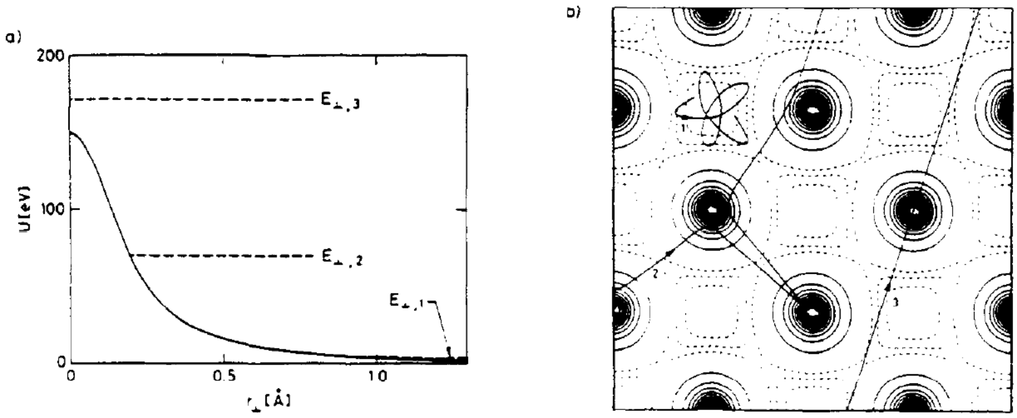

Figure 1.5: Transverse motion in a <100> germanium crystal. (**a**) The potential of an isolated string. (**b**) Contour plot of the complete potential. The trajectories correspond to the three distinct values of $E_\perp$ highlighted in (**a**) [10].

For relativistic particles this argument is still valid and $E_\perp$ takes the form:

$$E_\perp = \frac{p_\perp^2}{2M\gamma} + U(\boldsymbol{r}_\perp) = const \tag{1.10}$$

where γ is the Lorentz factor, $\gamma = \sqrt{1 - v^2/c^2}$. Just like equation (1.8), the expression (1.10) becomes:

$$E_\perp = \frac{1}{2} p\, v\, \psi^2 + U(\boldsymbol{r}_\perp) \tag{1.11}$$

Depending on the value of $E_\perp$ compared to the maximum potential $U(0)$, various particle motion scenarios may arise, as shown in figure 1.5:

- if $E_\perp \ll U(0)$ ($E_{\perp,1}$ in figure 1.5), the particle is confined at the bottom of the potential well and has a highly localized oscillating trajectory, called rosette orbit. This condition is called *hyper-channeling* [17];
- *under-barrier motion* occurs when $E_\perp \lesssim U(0)$ ($E_{\perp,2}$ in figure 1.5): the positively charged particle is kept at a distance from the area near the string of high atomic density. Consequently, the yield of the close-encounter process decreases;
- *over-barrier motion* corresponds to $E_\perp > U(0)$ ($E_{\perp,3}$ in figure 1.5). In this case the particle is unbound and free to move inside the lattice. It interacts with target atoms in a way similar to how it would in an amorphous (random) medium.

More precisely, taking into account that target nuclei may deviate from their average position ($\boldsymbol{r}_\perp = 0$) due to thermal displacements, a slightly smaller critical value of $U(\rho)$ should be chosen. When far away from strings, $E_\perp$ consists purely of kinetic energy and can be expressed as $E_\perp = \frac{1}{2}pv\psi^2$, where ψ represents the polar angle of the incident path (rather than the local path) relative to the string. The characteristic angle for directional effects is then:

$$\psi_c \simeq \sqrt{\frac{2U(\rho)}{pv}} \tag{1.12}$$

For any reasonable choice of potential, this result approximates Lindhard's critical angle ψ_1:

$$\psi_c \simeq \psi_1 = \sqrt{\frac{4Z_1Z_2e^2}{pvd}} \tag{1.13}$$

Using this expression, it is possible to estimate the angular acceptance of the channeling phenomenon.

In the previous considerations, the transverse energy conservation was employed. However, this is an approximation: the particle loses energy by inelastic processes and it can escape from its bound state. Such effect, called *dechanneling*, needs to be considered in a quantitative description. Dechanneling may be caused by scattering with point charges (in contrast to the continuum model), which can include electrons and thermally displaced nuclei, as well as impurities present in the crystal [10].

The $E_\perp$ evolution may be considered as a random-walk process [1] with the $E_\perp$ changes being positive or negative in any single event:

$$\Delta E_\perp = pv\theta\theta_s + \frac{pv}{2}\,\theta_s^2 \tag{1.14}$$

where θ_s is the angle of scattering in the event. As a result of this evolution, $E_\perp$ may exceed the potential well depth, causing the particle to leave the channeling mode. It is also possible for particles that have undergone dechanneling to be re-channeled.

Since the most frequent collisions of the particle are soft, one way to treat scattering in the channeling process is to apply the formalism of the diffusion theory [1]. From this theory, in the crystal volume, the fraction of channeled particles decreases exponentially as $\exp(-z/L_D)$, where L_D is the dechanneling length, which does not depend on the initial particle distribution and is proportional to the interplanar distance [1].

As dechanneling is a complex phenomenon, its full description is achieved through Monte Carlo computer simulations [18].

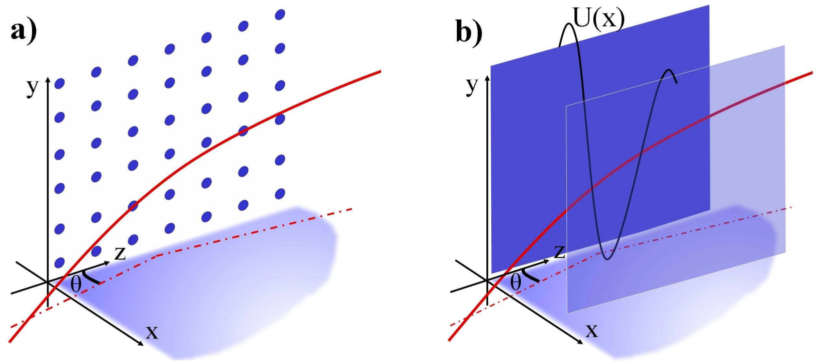

Figure 1.6: Planar channeling. (**a**) A particle impacts with a small angle relative to the plane of the crystal. (**b**) The particle experiences an average potential $U(x)$ [14].

Incorporating the z-dependence of the $E_\perp$ distribution into the previously outlined calculations ensures reliable results, enabling good agreement between theory and experiment for several crystal thicknesses in both the axial and planar cases [10].

1.2.2 Planar Channeling

For ions incident along planar directions in a crystal, a similar continuum approximation applies [10]. In this case the smearing of the atomic charges is over the planes, that is, in two dimensions.

For the planar case the standard continuum potential, shown in figure 1.6, for a single static plane assumes the form:

$$U(x) = 2\pi\, Z_1\, Z_2\, e^2\, n\, d_p \left[\sqrt{x^2 + C^2 a^2} - x\right] \tag{1.15}$$

where x is the distance from the plane, d_p is the distance between planes and n is the atomic density. Also for the planes, a thermal averaging should be performed. However, the effect of the smearing is less dramatic than in the axial case since static planar potentials remain finite at the positions of the planes.

The critical angle ψ_p can be obtained in the same way as for the axial case:

$$\psi_p = \sqrt{\frac{4 Z_1 Z_2 e^2 n\, d_p C a}{pv}} \tag{1.16}$$

For the (110) silicon planes the angle ψ_p goes from 20 µrad at an energy of

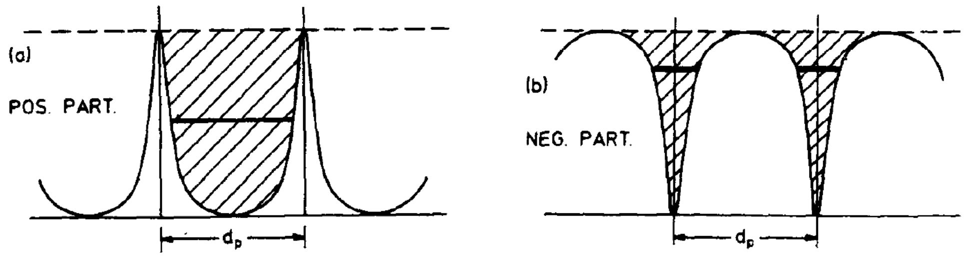

Figure 1.7: Planar continuum potentials for positively (**a**) and negatively (**b**) charged particles. The channeling region is hatched [10].

100 GeV to 7 µrad at 1 TeV [1]. The planar continuum potential is shallower than the one for the axes, resulting in narrower critical angles. Typically $\psi_p \sim \psi_1/3$. In the planar case, $E_\perp < U(0)$ corresponds to the confinement to one channel.

1.2.3 Negative Versus Positive Particle Channeling

So far, only incident positively charged particles have been considered. When negatively charged particles are involved, the interaction potential appears equal in shape but of opposite sign as compared to the potential governing the motion of positively charged particles. In the continuum picture, negative particles experience potentials with minima at the center of strings or planes, as shown schematically in figure 1.7 for the planar case [10].

Indeed, channeled negative particles tend to concentrate around the nuclei, unlike their positive counterparts. Consequently, negative particles exhibit an increased probability of close encounter processes during channeling [19]. The dips in yield observed for closely aligned positive particle beams transform into peaks for beams of negatively charged particles, as illustrated in figure 1.7.

Moreover, the more frequent interaction with target nuclei leads to much more severe dechanneling for negative particles, particularly in the axial case, compared to positive ones. The discrepancy in the channeling behavior between particles of opposite charge is even more evident in the axial scenario. Positively charged particles move freely between channels, whereas negatively charged ones are confined to a single string, or occasionally, a pair of strings [19].

Furthermore, the angular momentum of a negatively charged particle channeling around a string is nearly conserved, as the continuum potential it meets is almost rotationally symmetric, unless the particle is very weakly bound [10].

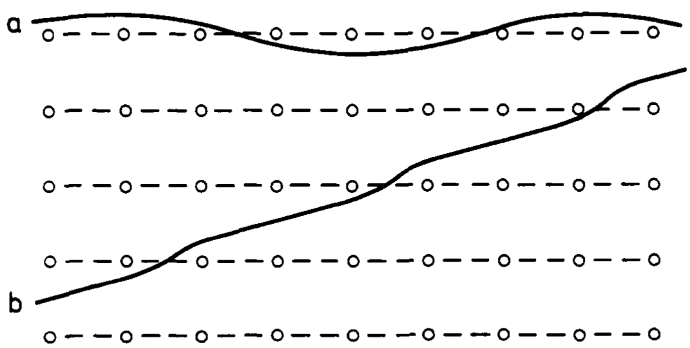

Figure 1.8: Qualitative illustration of the classical electron motion, governed by a continuum planar potential. **(a)** leads to channeling radiation while **(b)** to coherent bremsstrahlung. The angles of the paths with the crystal planes are exaggerated [20].

1.3 The Radiation Emission

As known from classical physics, an electrically charged particle emits radiation when accelerated. Since the emitted power P is instantaneously proportional to the square of the acceleration, $P \propto (F/M)^2$, only the lightest particles, electrons and positrons, are of practical interest as radiators [10].

If the incident particle interacts with an oriented crystal, the radiation may exhibit different characteristics compared to the ones in an amorphous medium. For instance, as shown in figure 1.8, when electrons penetrate a crystal with a small angle with respect to a plane, their trajectory is influenced by the correlated collisions with the atoms of the plane. This results in a motion described by a continuum transverse potential, obtained by averaging the crystal potential over the two dimensions of the plane, as previously discussed.

For incident angles smaller than the channeling critical angle, electrons may become trapped in a bound state, and the radiation emitted due to the acceleration in the transverse potential may be referred to as *channeling radiation*. For larger angles of incidence, the particle will have a too large transverse energy to be channeled and will move across the crystal planes. The periodic perturbation of the straight-line path by the planar potential will result in the emission of radiation, known as *coeherent bremsstrahlung*. A sketch of the different phenomena is shown in figure 1.9.

In both cases, the correlation of deflections by crystal atoms leads to an enhancement of the emitted radiation compared to normal bremsstrahlung. However, the frequency spectrum varies between coherent bremsstrahlung and

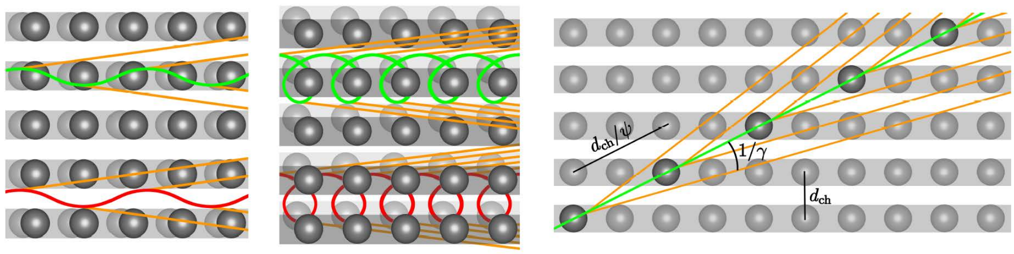

Figure 1.9: Comparison between the emission of axial channeling radiation (left), planar channeling radiation (center) and coherent bremsstrahlung (right) [21]. The electron trajectories are shown in green, the positron trajectories are shown in red and the emitted photons are shown in orange.

channeling radiation. In coherent bremsstrahlung, the spectrum is determined by the crystal periodicity, while in channeling radiation, it is influenced by the characteristics of the local planar potential, including its shape and strength. Typically, the resulting photon frequencies of coherent bremsstrahlung are an order of magnitude higher than the ones of channeling radiation [11].

In the following sections, the theory of bremsstrahlung for incoherent sources will be discussed first, followed by its generalization for coherent sources, and finally, the connection with channeling radiation will be explained. In the final section, radiation production in an oriented crystal under the Strong Field condition will be discussed. For a more comprehensive treatment, refer to [10, 19].

1.3.1 Standard Bremsstrahlung

Bremsstrahlung refers to the emission of electromagnetic radiation due to the scattering of fast charged particles in the electric field of a nucleus [22]. At high velocities, the emission process needs a quantum mechanical explanation. In the Born approximation $Z\alpha \ll 1$, where Z is the atomic number and α is the fine-structure constant, the cross section for photon emission with energy $\hbar\omega$ due to the impact of relativistic particles with a total energy E can be obtained using the Bethe-Heitler formula:

$$\frac{d\sigma}{d\hbar\omega} = \frac{16}{3} Z^2 \alpha \, r_e^2 \frac{1}{\hbar\omega} \left(1 - \frac{\hbar\omega}{E} + \frac{3}{4}\left(\frac{\hbar\omega}{E}\right)^2\right) \ln\left(183\, Z^{-1/3}\right) \tag{1.17}$$

where $r_e = e^2/mc^2 = \alpha^2 a_0$ is the classical electron radius, α is the fine-structure constant and the logaritmic factor indicates that the atomic

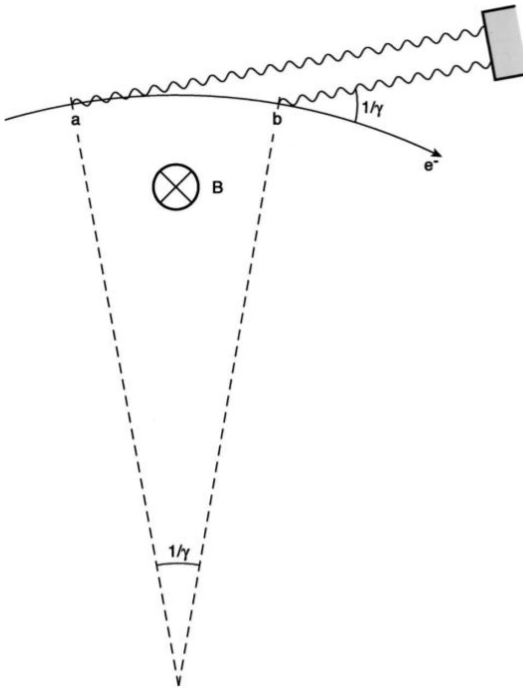

Figure 1.10: Synchrotron-radiation emission by an energetic electron crossing a magnetic field B. The distance ab represents the formation length [19].

(Thomas-Fermi) screening is complete, which requires $\gamma \gg 1$. At a moderate value of γ, equation (1.17) still holds for soft photons, $\hbar\omega/E \ll 1$.

According to equation (1.17) the dependence on the photon energy is essentially $1/\hbar\omega$. At high energies, photons are emitted in a narrow cone with an opening angle $\sim 1/\gamma$ around the initial direction of motion of the particle [23]. The uncertainty on the emission direction is equivalent to an uncertainty on the point of emission. Thus, one can define the so-called *formation length.* Consider the emission of synchrotron radiation in a bending magnet with a field B as, for instance, in a synchrotron light source, as shown in figure 1.10. A detector will not give information on the actual position of radiation emission over the distance a to b, so it is not possible to tell where the photon was emitted over this length, which is called formation length. Since the emission angle $1/\gamma$ connects the gyromagnetic curvature radius $r_c = pc/eB$ and the formation length l_f by $l_f = r_c/\gamma$ for small angles, the result is:

$$l_f = \frac{pc}{eB\gamma} \tag{1.18}$$

where p is the momentum. Since synchrotron radiation has a characteristic frequency $\omega_c = 3\gamma^3 eB/2p$, one obtains:

$$l_f = \frac{3\gamma^2 c}{2\omega} \tag{1.19}$$

In addition, the *radiation length* X_0 can be computed [19]:

$$\frac{1}{X_0} = \frac{n}{E}\int_0^E \hbar\omega \frac{d\sigma}{d\hbar\omega} d\hbar\omega = 4\, Z^2 \alpha\, n\, r_e^2 \ln\left(183\, Z^{-1/3}\right) \tag{1.20}$$

This parameter represents the penetration depth over which an incident particle, on an average, loses all but a fraction 1/e of its initial energy. Equations (1.17) and (1.20) include only the scattering off the nucleus. Radiation may also be emitted as a result of direct scattering on target electrons and this leads to an extra contribution to the cross section of $1/Z$ times the nuclear one. This brings the radiation length into good agreement with tabulated values [24]. In addition, for very light targets ($Z \leq 5$), the description of screening should be more accurate than the one provided by the statistical Thomas-Fermi model [10].

1.3.2 Coherent Bremsstrahlung

When an electron or a positron penetrates a single crystal with an angle larger than the critical angle but small enough for the continuum approximation to be valid, there is a good chance of coherent scattering on many target atoms along its path. The coherence in scattering extends to the radiation emission and, as a result, the emission in a single crystal can greatly exceed the bremsstrahlung emission in a similarly dense but amorphous medium composed of the same type of atoms. In this section, the emission process will be explored in the limit where the incident particle interacts both with the radiation field and with the crystal atoms, a scenario that can be treated in the Born approximation [25]. This case is referred to as coherent bremsstrahlung.

In the perturbation limit, the probability of bremsstrahlung emission is directly related to the square of a second-order matrix element. This element consists of several terms, each proportional to the product of two first-order matrix elements: one for the interaction with the radiation field and the other for the scattering in the atomic field. Since the particle states are plane waves, one finds [10]

$$d\sigma \propto \left| \int V(r) e^{i\boldsymbol{q}\boldsymbol{r}} d^3\boldsymbol{r} \right|^2 \tag{1.21}$$

where V is the atomic potential and $\hbar\boldsymbol{q}$ is the recoil momentum of the atomic nucleus. For N atoms, the single interaction potential V must be replaced by a sum over all the interactions, $\sum_n V(\boldsymbol{r} - \boldsymbol{r}_n)$ where $\boldsymbol{r}_n$ denotes the position of the n$^{\text{th}}$ atom. Thus the differential cross section for N atoms is [10]:

$$\left.\frac{d\sigma}{d\hbar\omega d^3\boldsymbol{q}}\right|_{\text{N atoms}} = \left.\frac{d\sigma}{d\hbar\omega d^3\boldsymbol{q}}\right|_{\text{single atom}} \times \left|\sum_n e^{i\boldsymbol{q}\boldsymbol{r}_n}\right|^2 \tag{1.22}$$

For an amorphous medium, the final factor is equal to N, since the mixed terms correspond to random phases and sum to zero. Therefore, the incoherent cross section (1.17) becomes proportional to the number of atoms within the formation length, which explains the $1/\hbar\omega$ behavior [19]. For a perfect static single crystal, in the limit $N \to \infty$, the last term of equation (1.22) becomes [10]:

$$\left|\sum_n e^{i\boldsymbol{q}\boldsymbol{r}_n}\right|^2 = N\frac{(2\pi)^3}{N_0\Delta}|S(\boldsymbol{g})|^2\sum_{\boldsymbol{g}}\delta(\boldsymbol{q} - \boldsymbol{g}) \tag{1.23}$$

where $\boldsymbol{g}$ is a reciprocal lattice vector, $S(\boldsymbol{g})$ the structure factor, N_0 is the number of atoms contained in a unit cell which has a volume Δ and $\delta(\boldsymbol{q} - \boldsymbol{g})$ is the Dirac delta function.

The coherent cross-section becomes appreciable when the wavelength of the emitted radiation is an integer times the direct lattice spacing of atoms in the chosen direction. An example of coherent bremsstrahlung spectra for high energy particles is shown in figure 1.11: as the angle with respect to the plane increases, the theoretical values based on the first Born approximation, shown by solid lines, become a better approximation to the data, shown by crosses.

1.3.3 Channeling Radiation

The channeling radiation is the coherent emission of photons due to the lattice structure of the crystal when a particle is channeled. Its discovery is attributed to Kumakhov, who was the first to derive the correct relativistic transformation [8]. Since the motion of the channeled particle is governed by the crystal field and cannot be approximated by that of a free particle, the perturbation treatment of the particle-crystal interaction breaks down.

Traditionally, channeling radiation is separated into three groups, depending on the energy of the penetrating particle: as the energy increases, the appropriate description varies from a quantized transverse potential, through the dipole approximation in classical electrodynamics, to a stage where transverse relativistic effects must be taken into account [19].

For the case of electrons or positrons with energies of a few MeV, a quantum description of the particle motion through an oriented crystal is required.

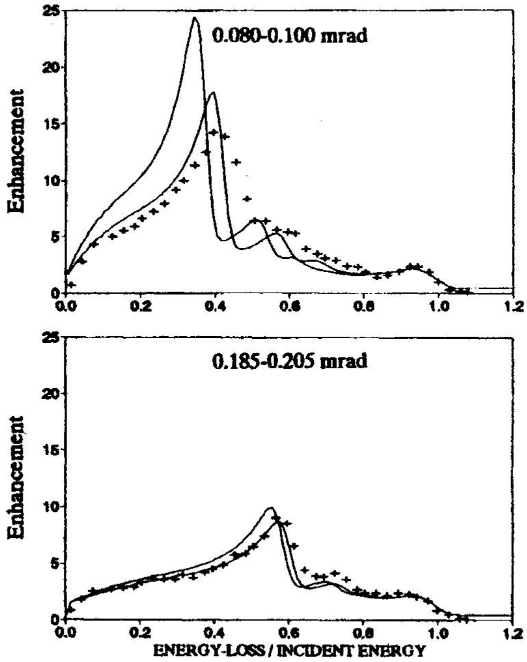

Figure 1.11: Radiation from 150 GeV electrons incident on a 0.6 mm Si crystal in different angular intervals with respect to the (110) plane. The enhancement is computed with respect to the radiation emitted by an amorphous target of the same material [19].

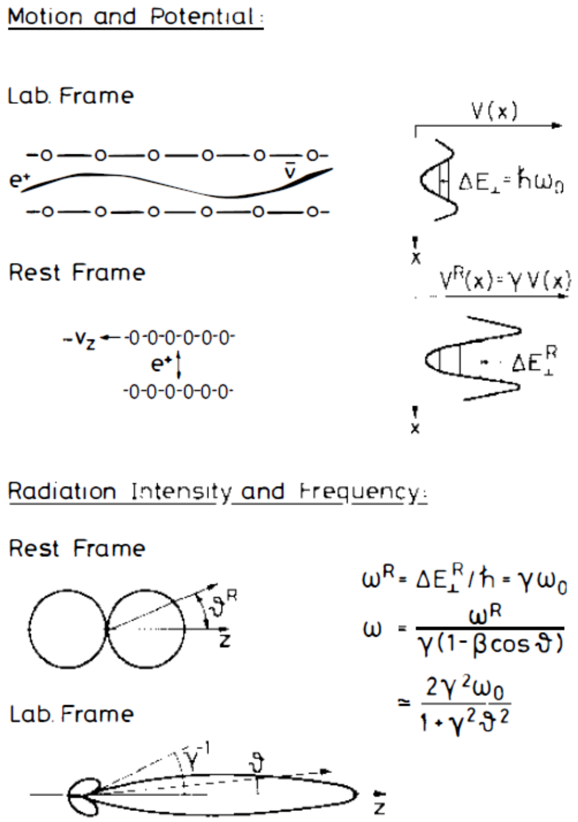

Figure 1.12: Illustration of Lorentz transformations between the laboratory and the rest frame R for a radiating planar-channeled positron with a kinetic energy of 1 MeV, corresponding to $\gamma = 3$ [11].

The crystal potential defines the states of motion through eigenfunctions of the transverse, stationary Schrödinger equation [10]:

$$\left[-\frac{\hbar^2}{2m\gamma}\Delta_{r_\perp} + U(\boldsymbol{r}_\perp)\right] u(\boldsymbol{r}) = E_\perp u(\boldsymbol{r}_\perp) \tag{1.24}$$

which is the quantized version of equation (1.10); $u(\boldsymbol{r}_\perp)$ is an eigenfunction corresponding to a well-defined transverse energy $E_\perp$.

The interaction with the radiation field allows for transitions between eigenstates through photon emission.

To establish the characteristics of channeling radiation, it is useful to introduce the so-called rest-frame (R), which refers to the viewpoint of an observer moving along the channel with the particle. In R the transverse potential is boosted by the Lorentz factor (figure 1.12). Consequently, the

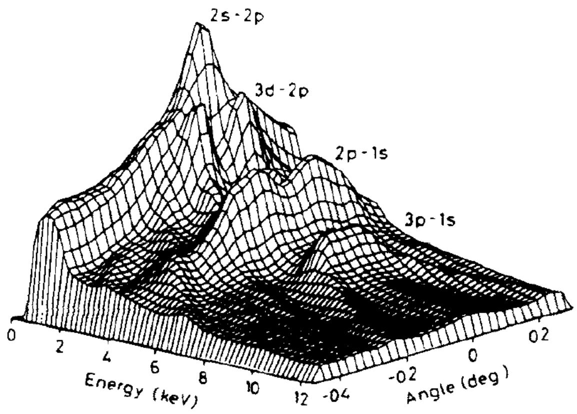

Figure 1.13: Experimental recording of axial channeling radiation generated by 4 MeV electrons incident on a <111> silicon crystal [10].

continuum potential is magnified by a factor γ, as compared to the laboratory one, $U^R = \gamma U$. The kinetic energy is also magnified by a factor γ in R compared to the laboratory frame since in R the motion is non-relativistic. As a result, the transverse energy spectrum is scaled by γ, $E_\perp^R = \gamma E_\perp$, while $\mathrm{u}(\boldsymbol{r}_\perp)$ remains unchanged. The photon energy as measured in R and corresponding to a jump from a state of transverse energy $E_{\perp_i}$ to one of $E_{\perp_f}$ then amounts to:

$$\hbar\omega^R = -\Delta E_\perp^R = -\left(E_{\perp_f}^R - E_{\perp_i}^R\right) = -\gamma \Delta E_\perp \tag{1.25}$$

A Doppler transformation back to the laboratory frame yields the final result:

$$\hbar\omega = \frac{-\Delta E_\perp}{1 - \beta\cos\theta_\gamma} \simeq \frac{2\gamma^2(-\Delta E_\perp)}{1 + (\gamma\theta_\gamma)^2} \tag{1.26}$$

where θ_γ denotes the emission angle relative to the z-axis. The γ^2 factor shifts the energy differences $\Delta E_\perp$, which are typically a few tens of eV, into keV photon energies. The emission pattern in the angular space is determined by the transformation between the two frames. In R, the emission patterns are dipole-like. However, since the photon emission at 90° to the z-axis in R corresponds to the emission at an angle $\sin^{-1}(1/\gamma) \simeq 1/\gamma$ in the laboratory system, channeling radiation is strongly forward directed exactly like normal bremsstrahlung.

Figure 1.13 shows a collection of channeling radiation spectra recorded in the forward direction for 4 MeV electrons incident at various angles with

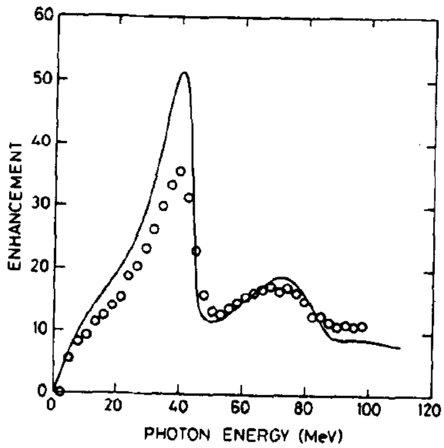

Figure 1.14: Planar channeling radiation from 6.7 GeV positrons incident on a {110} silicon crystal. The solid curve is the theoretical prediction according to standard classical electrodynamics formulas [10].

respect to the <111> axis of a silicon crystal: the quantum jumps are visible above the background of incoherent bremsstrahlung.

As the primary energy is raised into the GeV region, the number of channeling states becomes large and the level spacing reduces correspondingly. As a result, an essentially continuous transition through the dense spectrum of states becomes possible and channeling radiation appears as a classical emission process. Classical channeling radiation spectra are broad and featureless, but planar positron channeling exhibits unique characteristics, with the radiation concentrated in single-photon peaks. Anharmonicity in the potential leads to higher harmonics, especially with relativistic positrons, causing line broadening except at specific values where the effects balance out. Figure 1.14 shows the channeling radiation from 6.7 GeV positrons incident parallel to the {110} plane in a 0.1 mm thick silicon crystal.

At high energy, above 1 GeV, the dipole approximation is no longer justified because the longitudinal velocity $\beta_z c$ varies as a result of a relativistic transverse momentum $p_\perp$ [19]:

$$\beta_z^2 = \beta^2 - \beta_x^2 \simeq 1 - \frac{1}{\gamma^2}\left[1 + \left(\frac{p_\perp}{mc}\right)^2\right] \tag{1.27}$$

where the terms of the order $p_\perp/p_\parallel$ were neglected. The longitudinal motion becomes non constant, even in the absence of direct forces in this direction. An explanation can be found in the interaction of the particle, that has a relativistic transverse velocity, with the magnetic field in the average rest frame of the longitudinal motion. This field imposes a force in the longitudinal direction on the transverse velocity, such that a *figure-eight* motion results [26][27].

1.3.4 The Strong Field Regime

At energies high enough, the classical description of the radiation process becomes invalid. The problem is not the transverse motion of the charged particles, since the density of states increases with γ. The breakdown is associated with the recoil due to radiation. From the classical calculation of the synchrotron radiation emission in a magnetic field, it is known that the ratio of the instantaneously emitted power to the primary energy increases with γ. Thus, for γ larger than a certain value, the classically calculated radiation spectrum extends beyond the available energy. In this case, a quantum description and proper QED calculations must be used [10].

The classical spectrum of synchrotron radiation becomes modified when quantum corrections are taken into account, particularly in the case of emission within a sufficiently Strong Field. The external field is considered strong if the Schwinger's field parameter, χ, exceeds the unity value [28]:

$$\chi = \frac{e\hbar|F_{\mu\nu}|p^{\nu}}{m^3c^4} > 1 \tag{1.28}$$

where $F_{\mu\nu}$ is the field electromagnetic tensor, p^{ν} is the 4-momentum of the electron, e and m are the charge and rest mass of the electron, respectively. In oriented crystals, the condition becomes:

$$\chi = \frac{\hbar F\gamma}{m^2c^2} > 1 \tag{1.29}$$

where $F = |\nabla U|$ is the force acting on the electron due to the continuum potential U of the crystal atomic axes or planes. In the case of axial channeling

$$F \approx \frac{2Ze}{da_F} \tag{1.30}$$

where Z is the atomic number of the crystal, d is the distance between the atoms in the atomic strings and a_{F} is the Thomas-Fermi screening parameter. For instance, in a <110> silicon crystal ($Z = 14$), $F \approx 520\,\mathrm{eV}\,\mathrm{Å}^{-1}$ and $\chi \approx 1$ for electron energies of 150 GeV [28]. The Strong Field effects in radiation, such as quantum recoil due to hard photon emission, are already significant at $\chi < 0.1$ [28].

An accurate model to describe these effects is based on the Constant Field Approximation (CFA), meaning that the electric field is considered

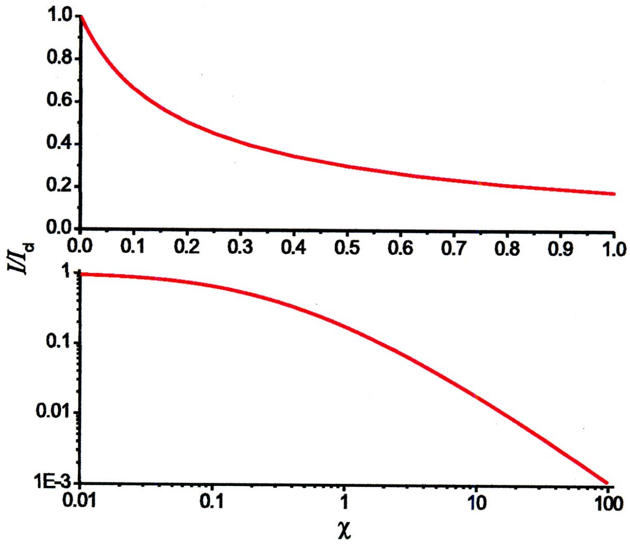

Figure 1.15: The intensity I of synchrotron radiation as a function of χ, normalized to the classical value I_{cl}. The top plot shows the $0 \leq \chi \leq 1$ region on a linear scale, while the lower part shows the $0.01 \leq \chi \leq 100$ region with a logarithmic scale [19].

approximately constant along the formation length and the transverse motion of the incident particle is described by means of a two-dimensional Schrödinger-like equation, corrected for the ultrarelativistic energies. From CFA the following approximate expression is found [19]:

$$I/I_{cl} \simeq [1 + 4.8(1+\chi)\ln(1+1.7\chi) + 2.44\chi^2]^{-2/3} \tag{1.31}$$

which is valid for a wide range of χ values. I is the intensity of the synchrotron radiation and I_{cl} is the classical value obtained for $\chi \to 0$. As shown in figure 1.15, the quantum corrections cause a reduction of the intensity compared to the classical synchrotron law. However, the emission probabilities in the quantum regime are still enhanced in a crystal with respect to the Bethe-Heitler value, due to coherence [19].

The *end-point* of the radiation spectrum, $\hbar\omega_c$, beyond which the frequencies are exponentially suppressed, can be found as [19]:

$$\frac{\hbar\omega_c}{E} \simeq \frac{\chi}{1+\chi} \tag{1.32}$$

The characteristic angle for CFA is given by the conservation of the transverse energy [10]:

$$\frac{p^2}{2\gamma m}\psi_0^2 = \frac{p^2}{2\gamma m}(\psi_0 + \Delta\psi)^2 - U_0 \tag{1.33}$$

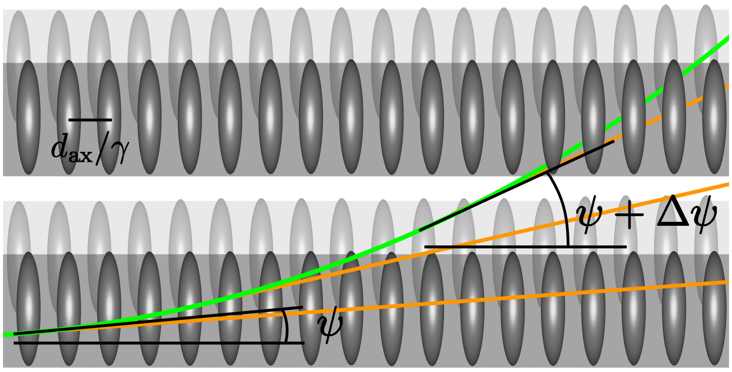

Figure 1.16: Sketch of the radiation emission in a strong crystalline field [21]. The parent electron is drawn in green, while the emitted radiation is drawn in orange.

where ψ_0 is the incidence angle and $\Delta\psi$ is the deflection angle. Considering small oscillations with respect to the incidence angle ($\Delta\psi \ll \psi_0$), it follows:

$$\Delta\psi = \frac{1}{\gamma}\frac{U_0}{mc^2}\frac{1}{\psi_0} \tag{1.34}$$

Thus, the angle

$$\Theta_0 = \frac{U_0}{mc^2} \tag{1.35}$$

separates two regions:

- $\psi \gg \Theta_0$: the radiation has a dipole nature and the deflection angle is larger than $1/\gamma$;
- $\psi \ll \Theta_0$: the radiation has a synchrotron nature and the deflection angle is smaller than $1/\gamma$.

Θ_0 is the so-called *Baier angle*.

A sketch of the radiation emission in a strong crystalline field is shown in figure 1.16.

1.4 Pair production and shower development

When a high energy photon interacts with an electromagnetic field, it may annihilate and create a lepton-antilepton pair: this phenomenon is the so-called *pair production*. In particular, the electron-positron pair production

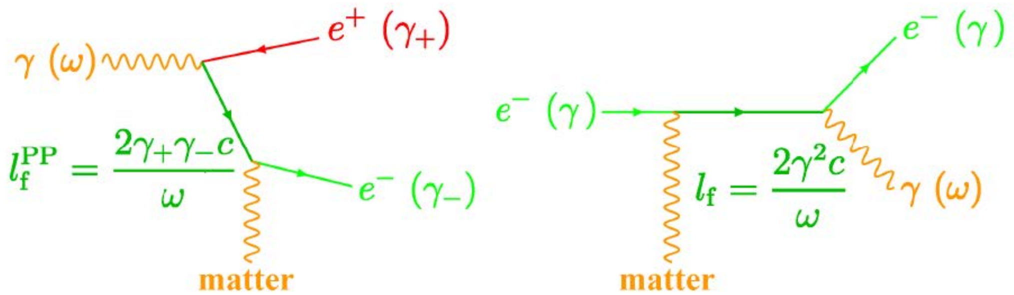

Figure 1.17: Feynman diagrams of electron-positron pair production (left) and bremsstrahlung (right).

is related to the emission of a photon from a moving electron (standard bremsstrahlung). Indeed, since a positron can be seen as an electron that travels backwards in time, the Feynman diagram of bremsstrahlung can be obtained by means of a counterclockwise rotation from the diagram of the pair production, as shown in figure 1.17. Since bremsstrahlung is heavily effected by the presence of the crystalline lattice, a magnification of the electron-positron pair creation process is also expected.

The differential cross section for the electron-positron pair production is given by the Bethe-Heitler formula, which mirrors the standard bremsstrahlung one [10]:

$$\frac{dN_{pp}}{d\eta} = \frac{16}{3} Z^2 \alpha r_e^2 nc \left(\frac{3}{4} - \eta + \eta^2\right) \log\left(183 Z^{-1/3}\right) \tag{1.36}$$

where η is the ratio of the energy of the created positron E_+ and the photon energy $\hbar\omega$, n is the density of the medium, α is the fine structure constant, r_e is the electron classical radius and Z is the atomic number of the target material. This is a threshold process, observed only for incident photons with an energy larger than $\sim 2mc^2$, where m is the electron mass. For energies beyond $\sim 100\,\text{MeV}$, this process becomes the dominant photon absorption mechanism.

The number of photons undergoing pair production in a target of thickness t is given by [29]:

$$N(t) = N_0 \left[1 - e^{-7t/9X_0}\right] \tag{1.37}$$

where N_0 is the number of incident photons and $\frac{7}{9}X_0$ is the pair production mean free path. Similarly to the standard bremsstrahlung case, the opening angle of the emitted pair is $\theta_{pair} \sim 1/\gamma_p$, where $\gamma_p = \hbar\omega/mc^2$ is the Lorentz factor of the emitted pair.

In order for channeling to influence the process by capturing the charged particle produced by an incident photon into channeled orbits, it is necessary for the opening angle to be smaller than the critical channeling angle, $1/\gamma \lesssim \psi_1$. This results in a threshold in photon energy, as described in [30]:

$$\hbar\omega_{th} \approx \frac{2(mc^2)^2}{|U(0)|} \tag{1.38}$$

A typical value for silicon is 5 GeV. However, to compete with incoherent pair production it is necessary to go considerably higher in energy.

Theorical results for pair production in oriented crystals are obtained using the Constant Field Approximation. The maximum enhancement over the Bethe-Heithler production may be estimated as [19]:

$$\max\left(\frac{N_{pp}^{CFA}}{N_{pp}^{BH}}\right) \sim \frac{U(0)ma_s d}{3Z^2\alpha^2\hbar^2 \ln\left(183Z^{-1/3}\right)} \tag{1.39}$$

where N_{pp}^{CFA} is the total Strong Field pair production probability, N_{pp}^{BH} is the Bethe-Heitler probability, a_s is the screening length of the target material and d is the inter-string spacing. The maximum enhancement can reach values of $\simeq 150$ and appears at an energy of approximately 100 times the threshold energy $\hbar\omega_{th}$, that is in the multi TeV region [19].

Figure 1.18 shows the calculated values for the total pair-production probability per unit distance in the CFA for several crystals, as a function of the initial photon energy.

If an electron/positron or photon with a high energy E_0 interacts with a thick absorber, it starts an electromagnetic cascade as pair production and bremsstrahlung generate more electrons and photons with decreasing energy, as schematically shown in figure 1.19.

The longitudinal development of the shower (figure 1.20a) is governed by the high energy part of the cascade and therefore scales as the radiation length in the material. When the electrons energy falls below the critical energy E_c, the electrons dissipate their energy via ionization and excitation rather than via the generation of more shower particles. The depth at which the largest number of secondary particles is produced is approximately located at [32]

$$t_{\max} \simeq \ln\frac{E_0}{E_c} + t_0 \tag{1.40}$$

where $t_{\max}$ is measured in radiation lengths, E_0 is the incident particle energy and $t_0 = -0.5$ $(+0.5)$ for electrons (photons). This formula states that the shower length, and therefore the detector thickness needed to absorb a shower, depend logarithmically on the incident particle energy, allowing to build compact calorimeters.

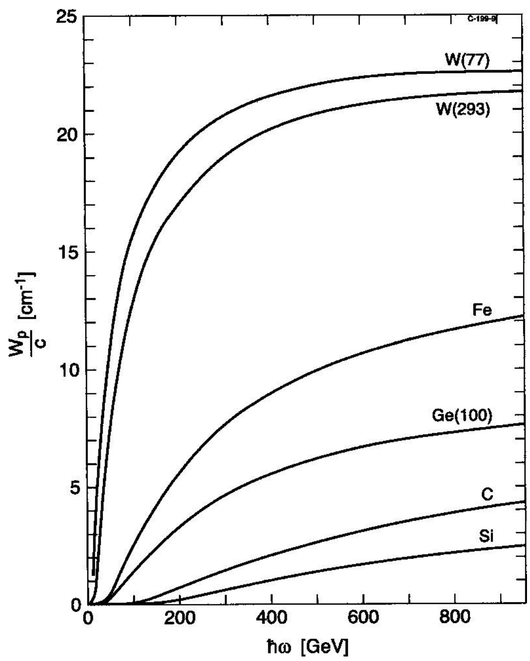

Figure 1.18: Pair-production probability as a function of energy by a photon impinging along the <111> axis for C, Si, Fe, and W and along <110> for Ge. The values within the brackets denote the temperature only when it differs from 293 K. The values are calculated according to the Constant Field Approximation [19].

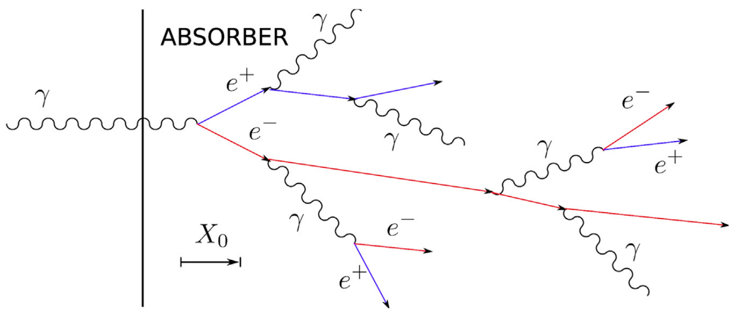

Figure 1.19: Schematic representation of an electromagnetic shower started by a high-energy photon [31].

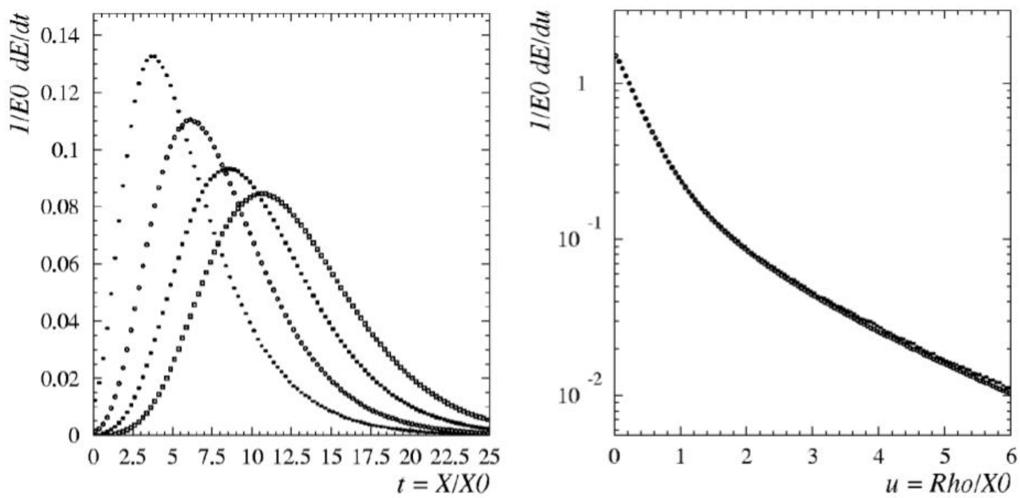

Figure 1.20: **(a)** Simulated shower longitudinal profiles in $PbWO_4$ (PWO), as a function of the material thickness (expressed in radiation lengths), for incident electrons of energy (from left to right) 1 GeV, 10 GeV, 100 GeV, 1 TeV [32]. **(b)** Simulated radial shower profiles in PWO as a function of the radial distance from the shower axis (expressed in radiation lengths), for 1 GeV and 1 TeV electrons [32].

The transverse development of the electromagnetic shower, shown in figure 1.20b, is mainly due to the multiple scattering of the electrons and positrons away from the shower axis. The transverse size, integrated over the full shower depth, is defined by the *Molière radius*, which can be approximated by [29]

$$R_M = \frac{X_0 E_s}{E_c} \tag{1.41}$$

where R_M represents the average lateral deflection experienced by an electron of energy E_c crossing $1X_0$ of matter, and $E_S \approx 21\,\mathrm{MeV}$. On average, 10 % of the energy lies outside the cylinder with a radius of $1R_M$ [32]. The Moliére radius depends on the material and not on the energy of the incident particle.

Figure 1.21 shows what would happen to the electromagnetic shower when a calorimeter is based on oriented crystals with respect to a non oriented calorimeter. Since bremsstrahlung and pair production are enhanced when on axis, the shower is more compact along the longitudinal direction. In particular, the shower peak is located significantly closer to the target front when the latter is axially oriented. The reduction of the shower length in crystals can be seen as the reduction of the effective radiation length [31, 33].

This reduction is not uniform along the depth of the crystal: the enhancement of the electromagnetic processes is the strongest in the first interaction of the primary particle. The secondary particles have an energy smaller than E_0 and are emitted with an angle with respect to the shower axis, which result in a reduction of the coherent effects. As a consequence, the shower generation features the most significant enhancement in the first radiation lengths and becomes similar to the case of amorphous-like media in the downstream part.

The next chapter will explore how the reduction of the effective radiation length in oriented crystals can be employed to develop a compact electromagnetic calorimeter. This aspect constitutes the primary focus of the OREO project and this thesis work will present the initial tests performed to assess its feasibility.

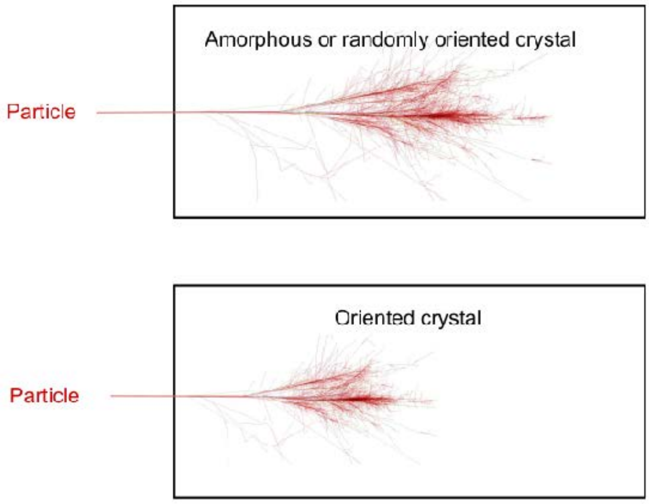

Figure 1.21: A schematic representation of the development of an electromagnetic shower in an amorphous or randomly oriented crystal (top) and in an oriented crystal (bottom).

Chapter 2

The OREO project

In the previous chapter, the theory of oriented crystals was introduced. This chapter will focus on OREO (ORiEnted calOrimeter), a project of the INFN (Istituto Nazionale di Fisica Nucleare) CSN5 (Commissione Scientifica Nazionale 5), which aims at studying the feasibility of an electromagnetic calorimeter based on oriented crystals and which represents the framework of this thesis work.

The first section of this chapter provides an overview of homogeneous electromagnetic calorimeters, essential instruments in high-energy physics experiments. Then, specific experimental techniques to study oriented crystals are explored, before introducing the OREO project in detail, focusing on its motivations and exploring potential applications.

2.1 Homogeneous electromagnetic calorimeters

Advancements in high-energy physics and astrophysics are closely related to the development of advanced electromagnetic calorimeters, which are essential for achieving high resolution in energy measurements. For instance, crystal-based calorimeters play a key role in space experiments such as the Fermi Telescope [34] and DAMPE (DArk Matter Particle Explorer) [35], allowing for precise measurements across a wide energy range, from a few GeV to several TeV. Similarly, in particle collider experiments such as the Large Hadron Collider (LHC) at CERN, crystal calorimeters are instrumental in studying high-energy particle collisions, providing crucial insights into fundamental particles and their interactions.

Moreover, calorimeters are versatile detectors. Designed for energy measurement purposes, they may also allow the determination of the shower position and direction, the particle identification, the particle arrival time measurement, and they may be used in the trigger generation [32].

Electromagnetic calorimeters are used to measure the energy of electrons/positrons and photons through their electromagnetic interactions and can be classified according to their construction technique into sampling calorimeters and homogeneous calorimeters. Sampling calorimeters consist of alternating layers of an absorber, a dense material used to degrade the energy of the incident particle, and an active medium that provides the detectable signal. Homogeneous electromagnetic calorimeters are composed of a single material in which the electromagnetic shower started by the incident electron/positron or photon fully develops. This active medium serves both to degrade the energy of the particles and to generate the signal. The focus of this section will be on electromagnetic homogeneous calorimeters based on crystals, without considering the orientation of the crystal lattice relative to the incident particles.

The main advantage of homogeneous electromagnetic calorimeters is their excellent energy resolution, as all the energy of the incident particle is deposited in the active medium. However, the fine segmentation of the homogeneous calorimeters volume, especially in the longitudinal direction, is challenging. Thus, precise position measurements and particle identification may be difficult to achieve [32].

The energy resolution of a calorimeter can be written as follows [32]:

$$\frac{\sigma}{E} = \frac{a}{\sqrt{E}} \oplus \frac{b}{E} \oplus c \tag{2.1}$$

where $\oplus$ denotes a quadratic sum. The first term is called *stochastic term*, the second term is the *noise term*, and the third one is the *constant term*:

- the stochastic term is due to the fluctuations associated with the physical development of the shower. In homogeneous calorimeters, intrinsic fluctuations are small because all the energy of the incident particle is deposited in the active volume of the detector. Therefore, in most cases, the intrinsic resolution can be better than the statistical expectation by a factor known as the *Fano factor* [37]. Typical stochastic terms for homogeneous electromagnetic calorimeters are at the level of a few $\%/\sqrt{E(\text{GeV})}$;

- the noise term quantifies the contribution to the resolution due to the electronic noise of the readout chain and depends on the detector signal type (light or charge) and on the features of the readout circuit. In scintillation-based calorimeters, where the signal is collected as light,

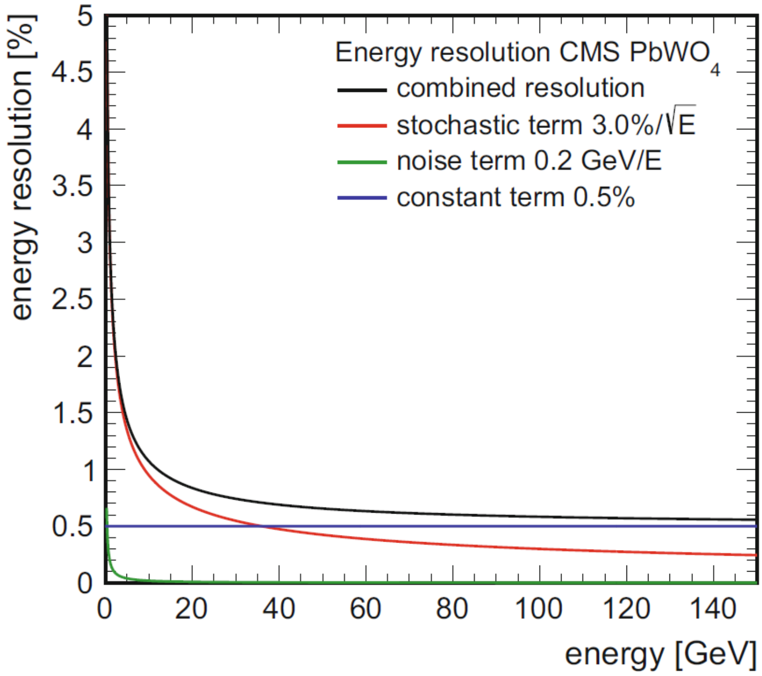

Figure 2.1: Different components contributing to the energy resolution of the CMS electromagnetic homogeneus calorimeter [36].

low levels of noise can be achieved if the photodetection system is properly chosen. The noise contribution increases decreasing the energy of the incident particles and becomes significant at energies below a few GeV. Therefore, for applications in the several GeV region, the noise equivalent energy is usually required to be smaller than 100 MeV;

- the constant term includes contributions that do not depend on the energy of the particle, arising from instrumental effects that cause non-uniformities in the detector response relative to the particle impact point. Non-uniformities can originate from the detector geometry, defects in the detector mechanical structure and readout system, temperature gradients, detector aging, etc. Typically, the constant term should be kept at or below 1 %. This is particularly important for homogeneous calorimeters due to their small stochastic term.

Additional contributions to the energy resolution arise from the constraints faced by a calorimeter when integrated into a large experiment, including longitudinal leakage, lateral leakage, upstream energy losses and non-hermetic coverage. These effects often dominate the resolution of homogeneous calorimeters operated in high-energy physics experiments due to their excellent stochastic term [32]. Figure 2.1 shows the energy resolution of the CMS (Compact Muon Solenoid) homogeneous electromagnetic calorimeter (ECAL) and its different components [36].

Among the available choices of detector materials, inorganic scintillators are the most appealing option in HEP, due to their high density and atomic number Z.

Generally, inorganic scintillators offer a high light yield, which depends on the material, and good signal linearity. However, some inorganic scintillators may exhibit slower response times compared to organic scintillators. The emission of light is closely tied to the crystal structure of the material. In order to improve some of their characteristics, crystals may be doped with small amounts of impurities [32]. These dopants create additional activation sites within the energy gap between the valence and conduction bands, allowing them to capture electrons from the conduction band, thus increasing the probability of photon emission and altering both the wavelength and decay time of the emitted light. Generally, doped crystals exhibit a slower response compared to undoped ones.

As schematically shown in figure 2.2, an incident charged particle can ionize a bound electron in the valence band and promote it to the conduction band, or it can create an exciton, i.e. it can form an electron-hole pair, which moves freely within the crystal, in the so-called excitonic band (an energy

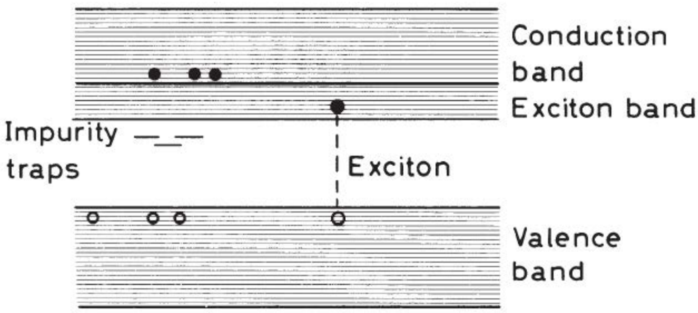

Figure 2.2: Electronic band structure of an inorganic crystal [38].

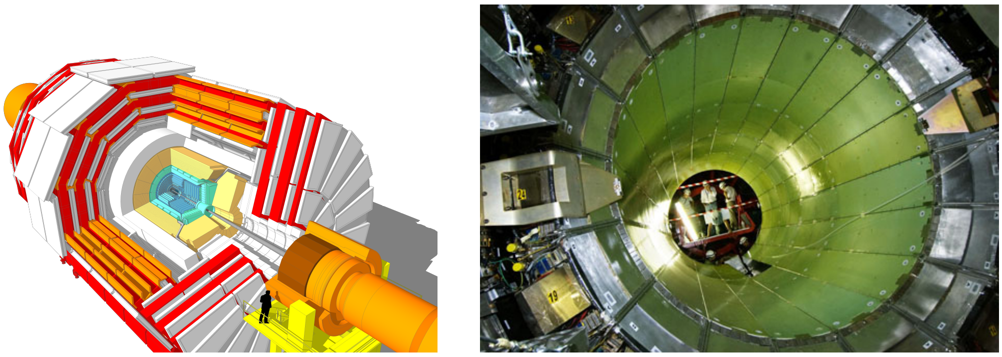

(a) **(b)**

Figure 2.3: **(a)** Cutaway diagram of the CMS detector [39]; **(b)** the CMS electromagnetic calorimeter (ECAL), made of PWO crystals [40].

level just below the conduction band and above the valence band), though weakly bound. Impurities in the crystal create energy levels within the band gap and if a hole (free or excitonic) meets an impurity, the impurity can ionize. At this point, an electron from the conduction band may fall into the impurity, emitting light. If the jump is non-radiative, however, the hole becomes a trap, and the energy is lost through vibrational relaxation. The frequency and response time of this emitted radiation depend on the energy gap between the valence and conduction bands [32].

Several materials have been used and are used in HEP experiments depending on the energy range to explore: among them, NaI(Tl), BGO, CsI and PWO[1]. Their properties are summarized in Table 2.1. In particular, PWO is very dense, fast and has an optimal radiation hardness. This makes it the crystal best suited for the LHC environment and it has been adopted by

[1] $PbWO_4$, lead tungstate.

Table 2.1: Main properties of several crystals used for homogeneous electromagnetic calorimeters in accelerator experiments [32].

	NaI(Tl)	CsI(Tl)	CsI	BGO	PWO
Density ($g\,cm^{-3}$)	3.67	4.53	4.53	7.13	8.28
X_0 (cm)	2.59	1.85	1.85	1.12	0.89
R_M (cm)	4.5	3.8	3.8	2.4	2.2
Decay time (ns)	250	1000	10	300	5
Emission peak (nm)	410	565	305	410	440
Light yield (γ/MeV)	4×10^4	5×10^4	4×10^4	8×10^3	1.5×10^2

experiments such as CMS (as shown in figure 2.3), $\overline{\text{P}}$ANDA (antiProton ANnihilation at DArmstad) and ALICE (A Large Ion Collider Experiment). One of the disadvantages of PWO is its low light yield, which is approximately 0.37% of the one of NaI(Tl). Moreover, the light yield is temperature-dependent.

In this section, crystal-based calorimeters have been discussed without considering the orientation of their crystalline structure with respect to the incident particles. The next sections will focus on the effects described in chapter 1, explaining how they can be used to develop a compact calorimeter based on oriented crystals.

2.2 Experimental investigations on oriented crystals

The experimental investigation of the Strong Field effects started in the 1980s with single-element crystals such as Si, Ge and W. These studies demonstrated that photons impinging on crystals along a specific axis exhibit a higher probability of pair production compared to amorphous targets [19]. Since then, several experiments addressing various aspects of oriented crystals have been performed.

2.2.1 Experimental Methodologies

To experimentally characterize the coherent electromagnetic interactions occurring in oriented crystals, it is necessary to design an experimental setup with specific features [41, 42]. The key elements both for the beam and the detectors are the following:

- e^+/e^- beams that enable the investigation of the radiation produced within the crystal under examination across a wide range of energies, allowing for the treatment of both the Strong Field and sub-Strong Field regions. Since the Strong Field threshold for PWO crystals is $\sim 30\,\text{GeV}$, higher energies are necessary for investigating the full Strong Field;

- a remotely controlled goniometer which ensures a precise spatial and angular alignment of the crystal lattice relative to the beam direction;

- a particle tracking system to reconstruct the incident particle trajectory and determine the angle with respect to the crystal with high resolution. This angle, known as the misalignment angle, is given by:

$$\theta_{miss} = \theta_{track} \pm \theta_{gonio} \tag{2.2}$$

  where θ_{track} represents the relative angle between the particle track and the tracking system axis, while θ_{gonio} is the relative angle between the crystal and the laboratory frame, as provided by the goniometer;

- a photodection system to study the scintillation light in PWO. This system was implemented for the first time in the context of the STORM (STrOng cRystalline electroMagnetic field) CSN5-INFN experiment [14, 42];

- an electromagnetic calorimeter positioned at the end of the beamline to measure the total energy output of the crystal;

- when the direct readout of the crystal scintillation light is not feasible, a multiplicity counter is employed to measure the multiplicity of the charged particles exiting from the crystal. This is crucial in the alignment procedure, as an increase in multiplicity is expected when the crystal is oriented. For this purpose, a scintillator placed after the crystal can be used, as there exists a direct proportionality between the number of particles exiting the crystal and the light produced in the scintillator. Alternatively, a tracking system can estimate the multiplicity of the charged particles considering the number of detected clusters;

- a Data AcQuisition system (DAQ) that allows to identify single particle events to measure the effect due to the crystal.

The next chapter will provide a more detailed explanation of these elements.

2.2.2 The AXIAL/ELIOT/STORM collaborations

Since 2016 there have been several INFN projects dedicated to the study of coherent effects in crystals.

In 2017-2018, several studies on tungsten crystals for the generation of intense radiation and positron beams were performed within the framework of the AXIAL (Axial and quasi-axial coherent interaction between charged particle beams and crystals) project. These investigations were further pursued in 2019-2020, as part of the ELIOT (Electromagnetic processes In Oriented crysTals) project and later within the STORM project in 2021-2022. More details on the experiments performed by the collaborations are given in [31, 33, 43–48]

The STORM project aimed at exploring the impact of the strong crystalline electromagnetic fields in high-Z oriented crystals, with a particular focus on PWO crystals. The primary goal was to quantitatively measure the acceleration of the electromagnetic shower development and assess its effect on the reduction of the radiation length X_0. This investigation involved testing PWO crystals coupled with Silicon PhotoMultipliers (SiPM) at the CERN SPS H2 beamline. The experimental setup used in August 2021 is presented in Figure 2.4. From left to right, the components are the following:

- two scintillator detectors (S1 + S2) used to generate the trigger;
- two high resolution silicon microstrip detectors (T1 and T2) for the particle tracking;
- the PWO crystalline sample coupled with the SiPM positioned on a high resolution goniometer;
- a plastic scintillator read out by a PMT (PhotoMultiplier Tube), used as a multiplicity counter;
- a silicon microstrip detector (BC1), to reconstruct the trajectory of the particles exiting from the crystal;
- a bending magnet, which separates the electrons from the photons;
- a silicon microstrip detector (BC2), also used as a multiplicity counter;
- an electromagnetic calorimeter (Genni), to measure the energy of the photons.

The deposited energy was measured inside two samples, one of $1X_0$ and the other of $2X_0$, both in the axial orientation and the random condition.

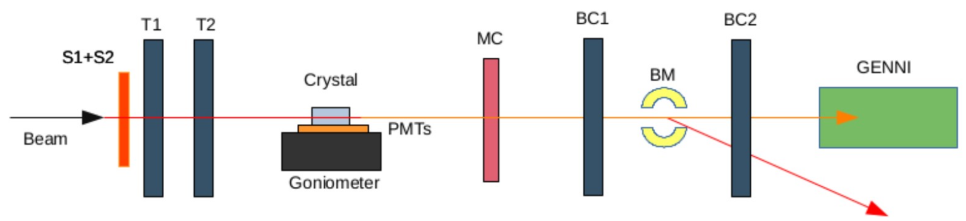

Figure 2.4: A schematic view of the STORM setup on the H2 beamline in August 2021 [14]. Refer to the text for the description.

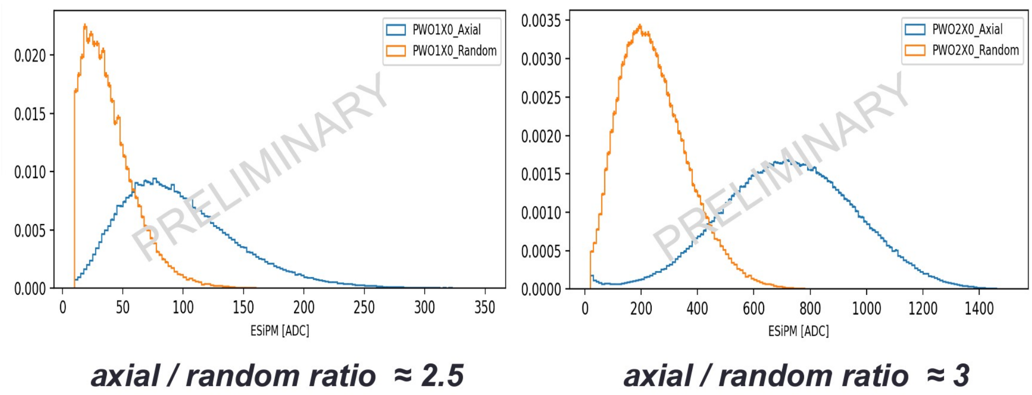

Figure 2.5: Scintillation light measured for two PWO samples with a thickness of about $1X_0$ (left) and $2X_0$ (right) in the axial (blue curve) and random (orange curve) orientation with a 120 GeV electron beam at the CERN SPS H2 line in 2021 [49].

As shown in figure 2.5, the deposited energy enhancement measured with respect to the random condition was ~ 2 for the $1X_0$ sample and ~ 3 for the $2X_0$ sample. The reduction of the radiation length experienced by the electrons in the Strong Field has been evaluated to be around 30 % [14]. Moreover, the measurements showed that the alignment procedure, which will be described in section 4.5, could be performed by measuring directly the energy deposited in the crystal itself, eliminating the need for an additional detector downstream of the crystal on the beamline [14, 42].

2.2.3 The OREO project

The next step in the study of coherent effects in oriented PWO crystals and of the possibility of assembling a compact electromagnetic calorimeter is represented by the INFN OREO project, started in 2023. Its primary goal is

Table 2.2: Properties of the lead tungstate crystal family.

Material	Density $[\mathrm{g\,cm^{-3}}]$	Scintillation [nm]	Light Yield [phe/MeV]	Decay constant [ns]	Reference
PWO	8.28	420	12	6	[50]
PWO-II	8.28	420	15	3.6	[51]
PWO-UF	8.27	420	7	0.640	[52]

to design, assemble and test an innovative homogeneous calorimeter prototype using oriented crystals and a SiPM-based readout system. By exploiting the reduction of the radiation length X_0 and the consequently shorter shower lengths, this project aims at developing a highly compact electromagnetic calorimeter, significantly reducing the material, volume, and weight compared to state-of-the-art detectors. The main challenge of the feasibility study is represented by the need to move from the analysis of the shower in a single oriented crystal to the development of a prototype consisting of several crystals oriented in the same way.

The material chosen for the OREO project is the ultrafast PWO scintillator (PWO-UF), which was recently developed.

As described previously, studies on undoped PWO crystals were performed, demonstrating their capability to exploit the Strong Field in axial orientation to reduce both the radiation length and the shower length. The PWO lattice has a scheelite-type structure, as shown in figure 2.6a, characterized by a tetragonal lattice with unit-cell parameters $a = b = 5.456\,\text{Å}$ and $c = 12.020\,\text{Å}$ [50]. Figure 2.6b presents the potentials as a function of the distance from the atomic string for the <100> and <001> axes. The <001> axis is the strongest one, resulting in an axial potential of approximately 480 eV, corresponding to an angular range for the Strong Field effect of the order of a few mrad. Other properties of PWO are summarized in table 2.1.

Studies on the luminescence properties of PWO crystals in the subnanosecond domain have shown two fast luminescence decay components, in addition to the main luminescence band [52]. The fraction of fast decay components can be increased via appropriate techniques to grow PWO scintillators [52], resulting in the production of PWO-UF. Table 2.2 summarizes some properties of PWO-UF in comparison with PWO and PWO-II. PWO-UF has a scintillation decay time constant of 640 ps and a high radiation tolerance. It is considered an outstanding candidate for the dual readout of scintillation and Cherenkov photons in electromagnetic calorimetry at future colliders [52]. Hence, PWO-UF could combine the reduction in X_0 achieved by aligning conventional PWO with faster light emission, making it an ideal candidate

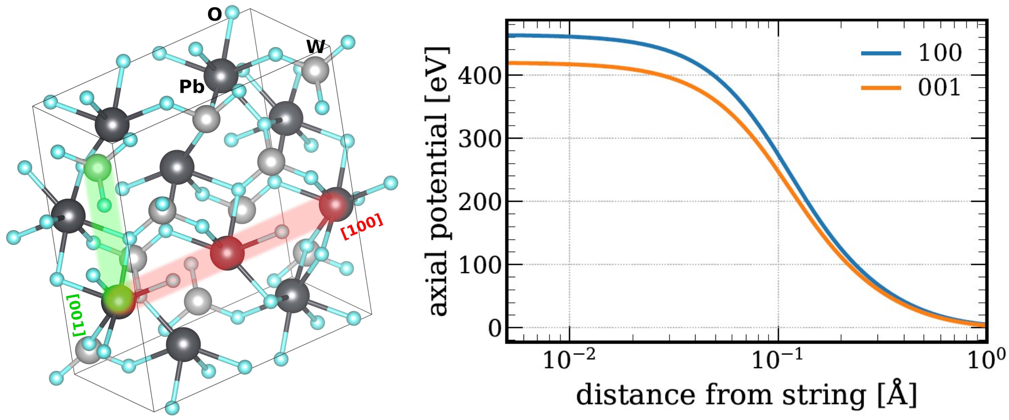

Figure 2.6: **(a)** PWO crystalline structure. The <001> axis is highlighted in green, while <100> is highlighted in red. **(b)** Potentials of the <001> and <100> axes plotted as a function of the distance from the atomic string [21].

for a compact, ultra-fast homogeneous calorimeter for the high-energy and high-intensity frontiers.

A prototype made with ultrafast PWO crystalline samples has be designed and built in the framework of the OREO project. The prototype is composed by two layers, as shown in figure 2.7. The first layer consists of a 3×3 matrix of crystals with a thickness of $\sim 5X_0$ and a transverse section of $2.5 \times 2.5\,\mathrm{cm}^2$. All the crystals of this layer have to be axially oriented. The second layer consists of a 3×3 matrix of not aligned crystals with a thickness of $\sim 11.2X_0$ and of the same transverse section as the ones in the first layer. Beside the advantages obtained exploiting the coherent effects in the first layer, another interesting feature of this detector would be the longitudinal segmentation, typically absent in scintillating homogeneous calorimeters. Longitudinal and transverse segmentation can provide valuable information for particle identification.

The OREO project will face the challenge to move from single crystals to a matrix of crystals aligned with each other within less than a mrad, developing a technology that should be scalable to true realistic calorimeters with a large number of crystals.

This thesis focuses on the test of the first OREO prototype, consisting of three crystals arranged in a 3×1 row.

Another important element of the OREO project is the simulation of the electromagnetic shower development within a crystal in Strong Field

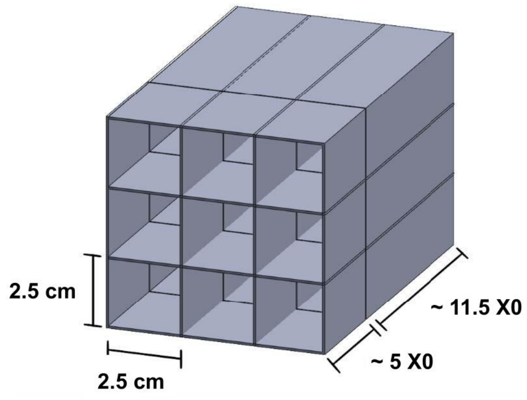

Figure 2.7: Conceptual sketch of the OREO calorimeter.

conditions, which is crucial to design an oriented calorimeter and understand its performance. A new Geant4 model was developed to incorporate the lattice structure, enhancing the bremsstrahlung and pair-production cross sections in oriented crystals. This model stems from a previously developed algorithm based on the Baier Katkov quasiclassical method [31]. The results presented in figure 2.8 have been obtained using this new model and show the simulated fraction of the initial particle energy deposited per radiation length in electromagnetic showers generated by electrons, as a function of the penetration depth in randomly and axially oriented <001> PWO crystals: when the crystal is axially oriented, the shower development is accelerated and, as a result, the peak is shifted towards the crystal surface.

2.3 Applications of oriented calorimeters

So far, studies have been described regarding coherent effects in oriented crystals, with a particular focus on the feasibility of an electromagnetic calorimeter based on such crystals. The following sections explore some potential applications of these types of calorimeters.

2.3.1 Compact Calorimeters for HEP

Calorimeters based on oriented crystals exhibit a great potential for applications in particle physics. By reducing the volume of the calorimeter and enhancing performance, particularly in fixed-target experiments characterized by forward scattering (within a few mrad), these calorimeters offer significant

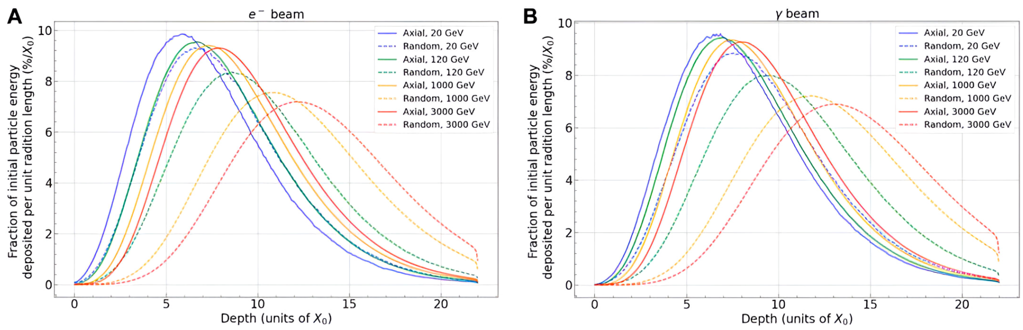

Figure 2.8: Simulated fraction of the initial particle energy deposited per radiation length in electromagnetic showers generated by electrons (left) and photons (right) as a function of the penetration depth in randomly (dashed lines) and axially (<001>) oriented (solid lines) PWO crystals [31].

advantages.

For instance, the reduced depth of the calorimeter, corresponding to the shortened electromagnetic shower length, results in decreased sensitivity to hadronic interactions. Indeed, unlike electromagnetic processes, hadronic interactions in crystalline matter are not influenced by the lattice orientation due to their limited range. Consequently, the ratio between the radiation length X_0 and the nuclear interaction length[2] λ_I is influenced by the lattice orientation and decreases as the effective X_0 gets smaller. This reduction is larger in the Strong Field regime. Hence, the detector thickness can be reduced, diminishing its sensitivity to hadronic interactions while maintaining the same sensitivity to electrons and photons [21, 31].

One potential application is represented by beam-dump experiments aimed at detecting light dark matter, such as NA64 [53]. Located at the CERN SPS, NA64 is a fixed-target experiment that employs active beam dump and missing energy techniques to probe rare events. If a dark photon is created in a shower started by an electron, it can be detected only if it survives for the remaining dump length. Shortening the dump length is crucial to boost sensitivity in these experiments. Oriented crystals offer a promising solution, as they can effectively detect high-energy particles arriving at precise angles considering that there is almost no material in front of the crystal to cause scattering [31].

Other applications, such as detectors for collider experiments at extremely forward angles, where particles arrive directly from the interaction point with

[2]The nuclear interaction length λ_I is defined as the average distance traveled by a hadronic particle before undergoing an inelastic nuclear interaction [29].

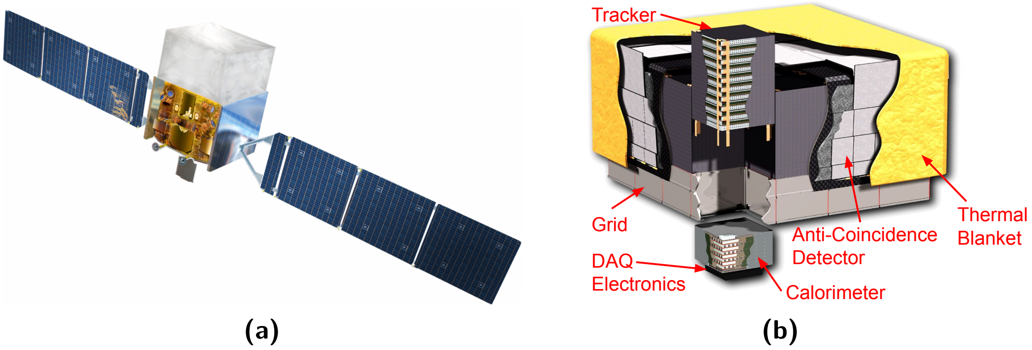

Figure 2.9: **(a)** The Fermi Gamma-Ray telescope. **(b)** Schematic view of the Fermi LAT instrument. Modified from [54].

minimal angular spread, are also worth considering.

Moreover, it may also be useful to consider alignment effects, even in the case when the crystal alignment is not needed. It is possible to align the crystal so that no axis is close to the expected particle direction. On the other hand, if a particle aligns with a crystal axis accidentally, it can lead to differences in the energy deposit compared to not aligned crystals, potentially affecting energy resolution due to intercalibration effects. These effects are more significant for shallow calorimeters or those with longitudinal segmentation.

2.3.2 Satellite-borne calorimeters

Applications of oriented crystals in Very High Energy (VHE) astrophysics represent a pioneering approach that could unlock new possibilities for γ-ray detection technologies on satellites. Indeed, the experimental investigation of several fields of astrophysics is based on the observation of multi-GeV γ-sources. An example of this approach is the Fermi Gamma-Ray Large Area Telescope (LAT) [34], presented in figure 2.9. The LAT measures the tracks of the e^+e^- pairs generated by photons impinging on multiple thin tungsten layers. These conversion foils are interleaved with silicon microstrip sensors, which track the charged particles and reconstruct the incidence angle of the photons. The produced pair then interacts with a scintillating homogeneous calorimeter composed of CsI bars, with a total thickness of $10X_0$.

Since the cosmic γ-ray sources emit high-energy photons that propagate to earth with a very narrow angular distribution, an oriented crystal based hodoscopic calorimeter could enhance the sensitivity of the telescope above a few GeV, thanks to the increase of the pair production cross section in the source direction.

In addition, electron/positron electromagnetic showers started by γ-rays with energies exceeding 100 GeV would be contained within a smaller volume compared to standard detectors. For instance, as shown from simulations (figure 2.8), in the case of a randomly oriented PWO-based detector, the shower peak is located at $\sim 12X_0$ for 3 TeV particles. On the other hand, when the detector is axially oriented, the shower maximum is located at $\sim 8X_0$ [31]. This feature offers the potential to reduce the longitudinal dimension and increase the transverse area of the detector, thereby enhancing sensitivity, with the same weight as a standard satellite. This is particularly significant in VHE astrophysics, where the primary challenge is the limited photon flux. A larger detector area combined with an improved shower containment in the 100-300 GeV range could be useful, given the current gaps in the observational coverage from both space and ground-based detectors [31].

Moreover, the increased sensitivity in a particular direction would inherently reduce the influence of the isotropic background noise, facilitating the identification of γ-ray sources. Since the maximum enhancement of showers in crystals typically occurs within a few mrad, this anisotropy can be exploited to enhance the angular resolution and consequently improve the source localization. This improvement can be achieved without the need for complex converter and tracker systems.

Several fields of astrophysics could benefit from the use of an oriented detector. These include the observation of γ-ray sources not identified by the Fermi Telescope, follow-up studies of transient and multi-messenger sources and the search for dark matter decays around the galactic center.

While the outlined applications for oriented crystal calorimeters would lead to several advantages in the field of astrophysics and HEP, the technology is still in its early stages. Establishing the feasibility of building a working prototype of such a calorimeter is crucial. The next chapter presents the first beamtest of a layer consisting of three oriented crystals, performed at CERN in 2023. This test marks one of the initial steps in the development of oriented crystal calorimeters.

Chapter 3

The OREO 2023 beamtests at CERN

In August 2023 the OREO collaboration performed two beamtests at CERN, to evaluate a preliminary prototype consisting of three crystals, organized in a row, readout by SiPMs. The measurements were performed on the T9 line at the PS East Area, with a maximum energy of 15 GeV, and on the H2 line at the SPS North Area, with energies ranging from 20 to 150 GeV.

This chapter is organized into three main sections. The first section provides an overview of the prototype, including details about the PWO crystal samples and the detection system. The second section describes the T9 and H2 beamlines, while the last section explores the experimental setups in detail.

3.1 Beamtest goals

The goal of the beamtests performed in August 2023 as part of the OREO project was to test a layer composed of three oriented PWO-UF crystals arranged in a 3×1 matrix, readout by SiPMs. The main goals were the following:

- to assess the homogeneity of the scintillation light emitted within the crystals, both when axially and randomly oriented;
- to verify the inter-alignment of the three crystals and to evaluate the radiation increase in the axial configuration compared to the random orientation;
- to investigate the behavior of the setup as a calorimeter, which is the ultimate objective with the complete prototype, of course taking into

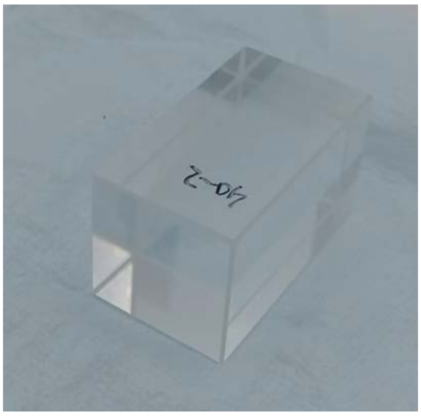

Figure 3.1: One of the PWO-UF samples, with a length corresponding to $5X_0$.

consideration the limited dimensions and the fact that the second "layer" was a different type of calorimeter.

3.1.1 The crystal samples

The prototype sample tested at CERN was composed of three crystals of PWO-UF manufactured by Crytur [52]. Each crystal had a dimension of $2.5 \times 2.5 \times 4.4\,\mathrm{cm}^3$, corresponding to a length of $5X_0$. The characterization of the crystals and the assembly of the layer were performed at the University of Ferrara. An example of the tested crystal is shown in figure 3.1.

The entrance surface with respect to the beam was aligned with the <100> axis, while the other faces were aligned respectively with the <010> and <001> axes. The orientations were verified using a X-ray diffractometer (XRD).

For each sample, the miscut angle, i.e. the angle between the axis and the sample surface, was measured. Moreover, it was observed that the direction of the axes among the three crystals did not vary by more than 200 µrad.

The layer was mounted using a motion system equipped with motorized opto-mechanical components from Thorlabs [55] and a laser autocollimator to ensure the precise crystal orientation before gluing them together. The lateral surfaces were coated with white EJ-510 [56] reflective paint. Two samples were positioned in front of the interferometer from Zygo [57] on supports allowing for movement and rotation. Using the interferometer to verify the alignment between the $2.5 \times 2.5\,\mathrm{cm}^2$ areas where the beam impinges, the samples were adjusted until their axes were aligned. SX-10 epoxy resin was then applied to the adjacent $2.5 \times 4.4\,\mathrm{cm}^2$ areas of the two samples and, thank to a translator, the samples were brought into contact and glued together to form a 2×1 array. The same alignment and gluing process was repeated between the 2×1 array and the third sample to create a 3×1 array. Finally, the beam entrance surfaces were painted, leaving uncovered only the regions to be put in contact with the SiPMs.

3.1.2 The photodetectors

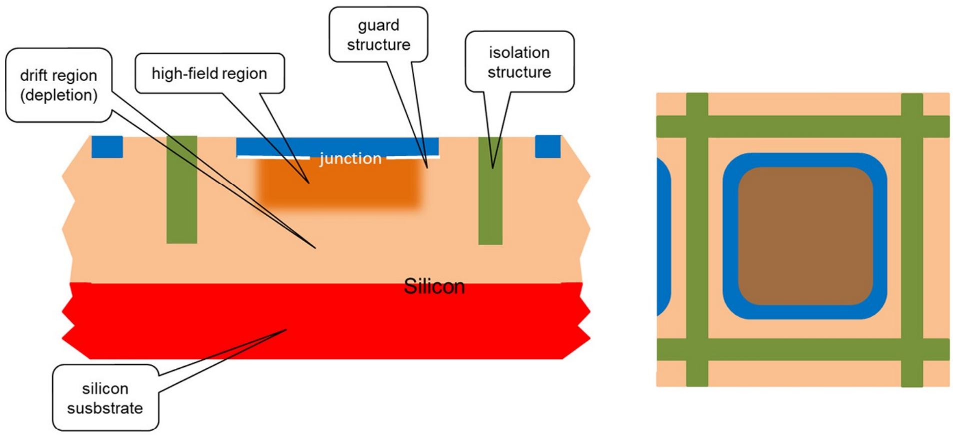

Figure 3.2: Schematic representation of a SPAD in a SiPM [58].

The OREO photodetection system is based on Silicon PhotoMultipliers (SiPMs) [58]. A SiPM (figure 3.2) is a solid-state photodetector consisting of an array of integrated Single-Photon Avalanche Diodes (SPADs) [59], called microcells or pixels, integrated on a common substrate and connected in parallel to a single output. The SPAD is essentially a p-n junction or diode working in the so called Geiger-Muller regime. In this condition, the electric field in the junction depletion layer is so large that, when a photon impinges, the generated electron-hole pair can trigger a self-sustaining avalanche. The avalanche is then quenched by lowering the bias voltage to or below the breakdown voltage[1] V_{bd}, thanks to a so called *quenching circuit*. The bias voltage must then be restored in order to allow for the detection of another photon.

Each pixel gives the same current response when hit by a photon; hence the total output signal is proportional (for moderate fluxes) to the number of hit pixels and, consequently, to the number of detected photons.

[1]When a reverse bias large enough is applied to the p-n junction, the junction starts to draw a large amount of current: this phenomenon is called breakdown.

The bias voltage is typically in the tens of volts range. The difference between the bias voltage and the breakdown voltage is known as *overvoltage* (OV).

SiPMs are characterized by a very high gain, of the order of 10^6. Considering the large density of cells, SiPMs are linear over a wide range of light intensities. The linearity limit is due to the finite number of cells because two or more photons that impinge on one cell produce exactly the same signal as one single photon. The relation between the number of incident photons and the number of fired cells is [60]:

$$N_{fired\ cells} = N_{total}\left[1 - \exp\left(\frac{-N_{photon} \times PDE}{N_{total}}\right)\right] \tag{3.1}$$

where N_{total} is the number of available pixels in the device, $N_{photons}$ is the number of impinging photons, $N_{fired\ cells}$ is the number of cells effectively fired by the impinging photons and PDE is the Photon Detection Efficiency of the SiPM, that is the statistical probability that an incident photon interacts with a microcell producing an avalanche, and is defined as [58]:

$$PDE(OV, \lambda) = QE(\lambda) \cdot P_T(OV, \lambda) \cdot FF(OV, \lambda) \tag{3.2}$$

where QE is the silicon quantum efficiency, P_T is the probability of generating an avalanche and FF is the fill factor of the device. The quantum efficiency is a measurement of the the probability that an incident photon creates an electron-hole pair in the sensitive volume of the sensor. TThis probability takes into account the fact that not all charge carriers in the active volume will start an avalanche. The fill factor is defined as the active area of all the SPADs divided by the total area of the SiPM, and depends on of the dead area between the microcells which in turn depends upon the microcell size.

Due to the finite number of available cells (N_{total}), deviations from linearity occur when the number of photons, i.e. the light intensity, is comparable to the number of available pixels [60].

SiPMs offer several advantages, including a low operating voltage and a compact design. Moreover, they exhibit fast response times and are insensitive to magnetic fields. These features make SiPMs highly effective for detecting light across a wide range of intensities, from single photons to several thousands of photons, thus making them suitable detectors for next generation high energy and space physics experiments. However, it is important to note that SiPMs may also exhibit high levels of noise and their performance parameters can be significantly affected by changes in temperature. The main source of noise in a SiPM is the Dark Count Rate (DCR), which is due to thermally

Figure 3.3: The photodection system, consisting of three SiPM matrices connected on a readout board. V_{bias} (the J4 connector) is the common bias for the three matrices.

generated electrons that may start an avalanche in the high field region and thus producing a signal which is indistinguishable from the one of a detected photon. The DCR is a function of the active area, overvoltage and temperature. The DCR has an exponential dependence on $-1/T$ and the dark current in silicon drops by a factor of 2 about every 10 °C decrease [59]. Also the breakdown voltage is temperature dependent, because the mean free path for electrons decreases with increasing temperature, hence a higher electric field is required to start the avalanche process [58]. Another source of noise is known as optical crosstalk, which occurs when photons emitted during avalanche breakdown in one cell travel to neighboring cells and trigger a second avalanche in the same manner as an external photon. Additionally, during an avalanche, it is possible for some of the charge carriers to be trapped in the high-field region and later re-emitted, triggering a secondary avalanche within the same cell. This phenomenon, known as afterpulsing, is characterized by a delayed signal with an amplitude lower than the primary event. The probability of afterpulsing depends on factors such as the number of traps, release time constants and the recharge time of the SPAD [59].

The OREO photodetection system consists of three SiPM matrices, model ARRAYC-60035-4P-BGA [61], produced by *Onsemi* [62], and a custom readout board designed at the Insulab laboratory, as shown in figure 3.3. The same system was previously used in the STORM project [14].

The ARRAYC-60035-4P-BGA consists in 4 individual 6 mm C-Series sensors [63] arranged in a 2×2 array (figure 3.4); its schematic drawing is shown in figure 3.5. Each C-Series sensor is a low-noise, blue-sensitive and high gain SiPM whose features are summarized in table 3.1. Each sensor is mounted on a Printed Circuit Board (PCB) that uses a Ball Grid Array

Table 3.1: Features of the C-Series sensors produced by Onsemi [63].

Photosensitive area	$6 \times 6\,\text{mm}^2$
Pixel pitch	35 µm
Number of pixels	18980
Geometrical fill factor	64 %
Breakdown voltage (V_{bd})	26 V
Recommended operating bias	$V_{bd} + 2.5\,\text{V}$
Terminal capacitance	3400 pF
Peak sensitivity wavelength	420 nm

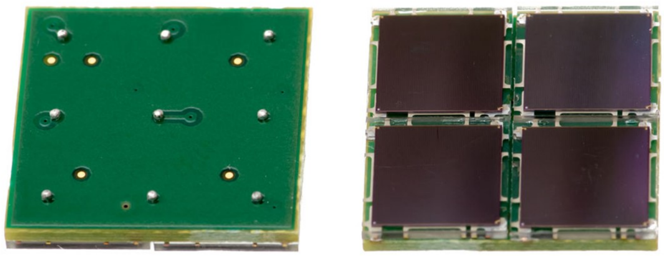

Figure 3.4: ARRAYC-60035-4P-BGA, consisting of 4 individual 6 mm C-Series sensors arranged in a 2×2 array [61].

(BGA) for routing the signals. The 4 SiPMs cathodes on the single matrix are connected together thus providing a common connection. The features of the array are summarized in table 3.2.

The readout board (figure 3.3 top) has been designed at the Insulab laboratory [2]. The schematic is shown in figure 3.6. It is a 2 layer $63 \times 23\,\text{mm}^2$ 1.5 mm thick printed circuit board. The sensors have been assembled on the board itself by SCEN [64]. All the matrices have a common bias (V_{bias}, J4 connector); the A1, A2, B1, B2 anodes are connected to ground while the common cathode is set to a positive bias. The signal of each matrix is coupled with a 100 nF capacitor to the digitizer input (forming a high pass filter with

Table 3.2: Features of the ARRAYC-60035-4P-BGA produced by Onsemi [61].

Array Size	Sensor Type	Redout	Board Size	Pixel Pitch	No. Connections
2×2	60035	Pixel	$14.2 \times 14.2\,\text{mm}^2$	7.2 mm	3×3 BGA

[2] E. Vallazza, INFN - Sezione di Milano Bicocca, Milano, Italy

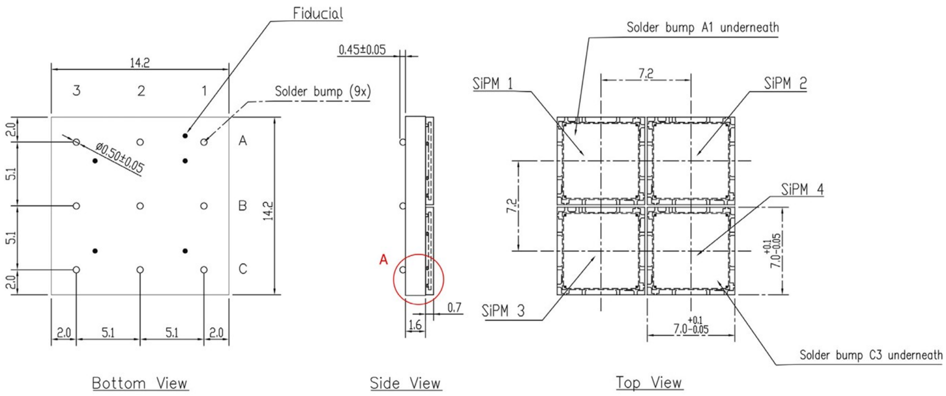

Figure 3.5: Schematic drawing of the ARRAYC-60035-4P-BGA. A1, A2, B1, B2 are the anodes (which are connected to ground), while A3, B3, C1-C3 are the cathodes which are connected together [61].

the 50 Ω digitizer input impedance) and is taken to the readout system with a Hirose connector/cable [65]. For the STORM experiment, four detectors were assembled, named John, George, Paul and Ringo. However, for the OREO project, only John, George and Paul were used.

Figure 3.7 shows the current-voltage (IV) curve of the SiPMs. It can be noticed that the breakdown voltage V_{bd} is around 26 V. The SiPM sensors are operated at a bias that is typically $10\% - 25\%$ higher than the breakdown voltage. During the beamtests, the bias voltage was selected depending on the context. At the T9 beamline, a bias of 31 V was used, whereas at the H2 beamline, the bias voltage ranged between 28 V and 29.5 V to prevent saturation.

The crystals and the detection system were mounted on a 3D-printed holder (figure 3.8) specifically designed for the beamtest. This holder is a modular support allowing for an easy installation and an efficient coupling with the SiPMs readout. It is designed to be directly interfaced with the goniometer. Figure 3.9 presents the system from the beam perspective. It is evident that the faces of the crystals do not cover all the SiPM matrices. Consequently, only two out of three matrices per board were coupled and read out.

3.2 CERN Beamtest Facilities

The accelerator complex at CERN is a succession of machines that accelerate particles to increasingly higher energy, as shown schematically in

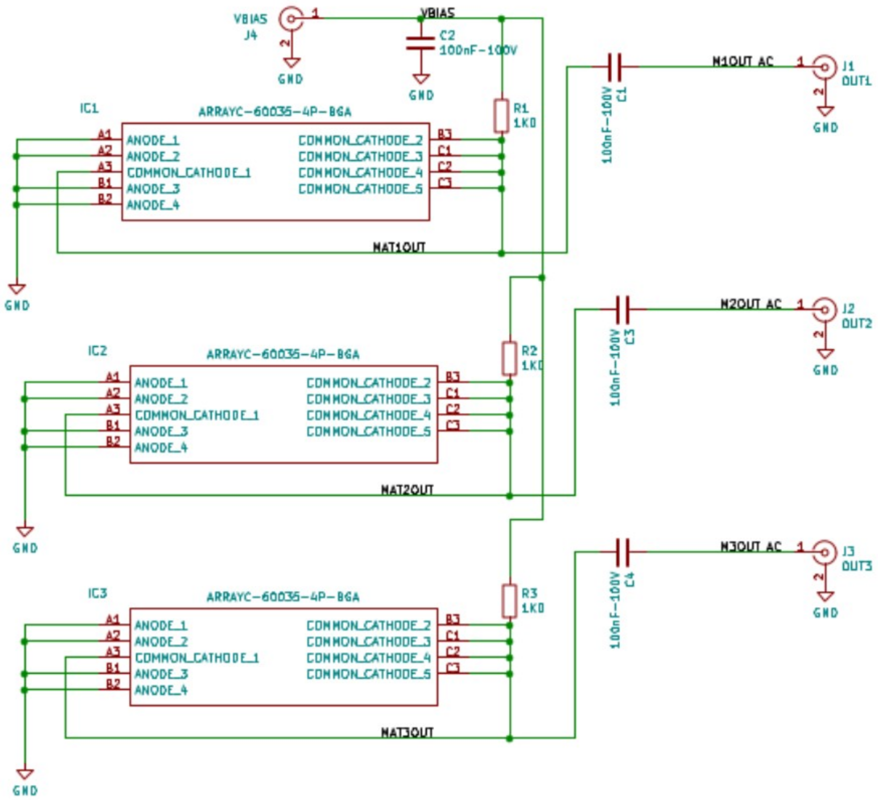

Figure 3.6: Schematics of the readout board.

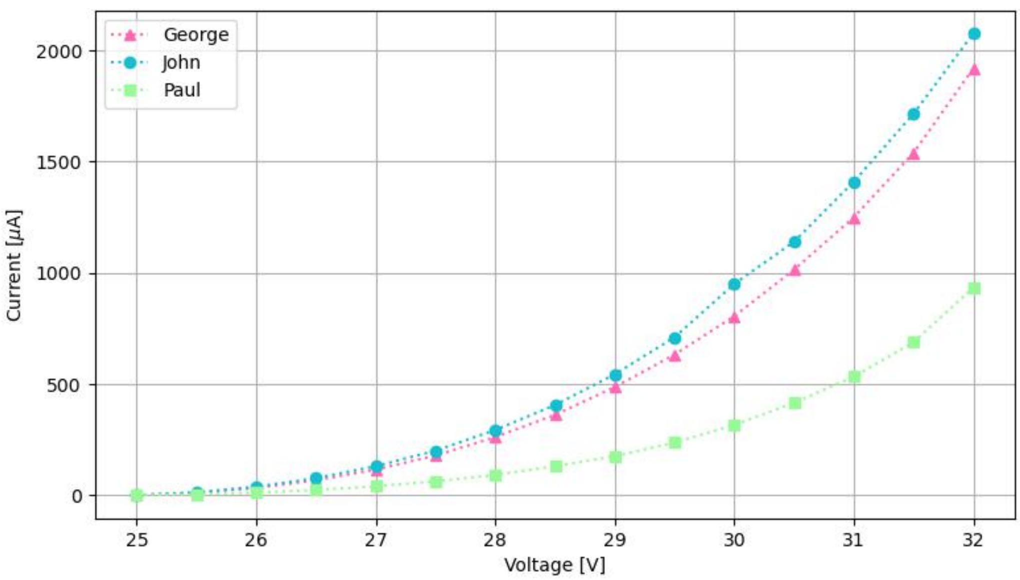

Figure 3.7: IV curves of the SiPMs.

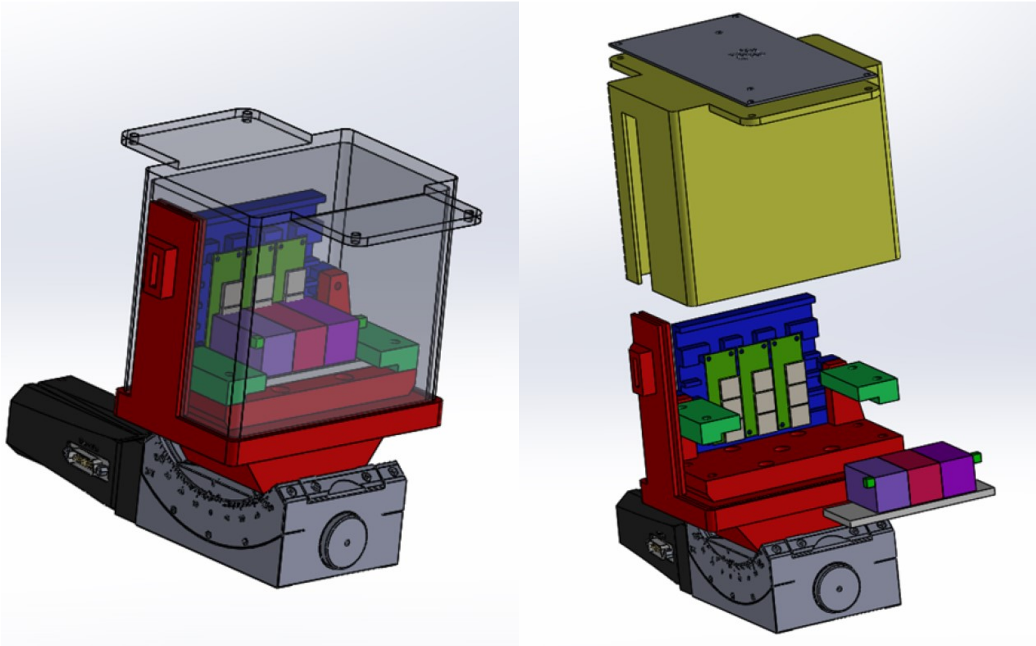

(a) (b)

Figure 3.8: 3D drawing of the crystal holder with the coupling system with the goniometer.

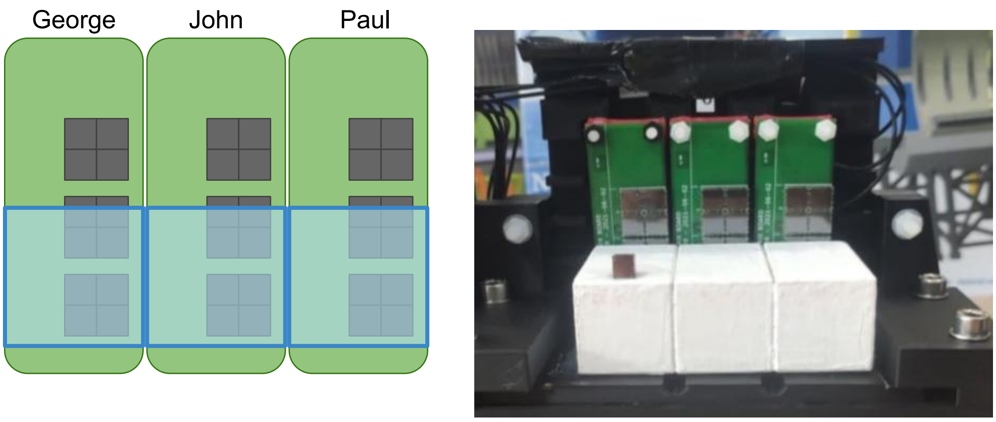

(a) (b)

Figure 3.9: **(a)** Schematic representation of the 3×1 layer coupled to the SiPMs. **(b)** Photo of the crystals coupled to the SiPMs mounted on the holder. Both the scheme and the photo are viewed from the perspective of the incident beam.

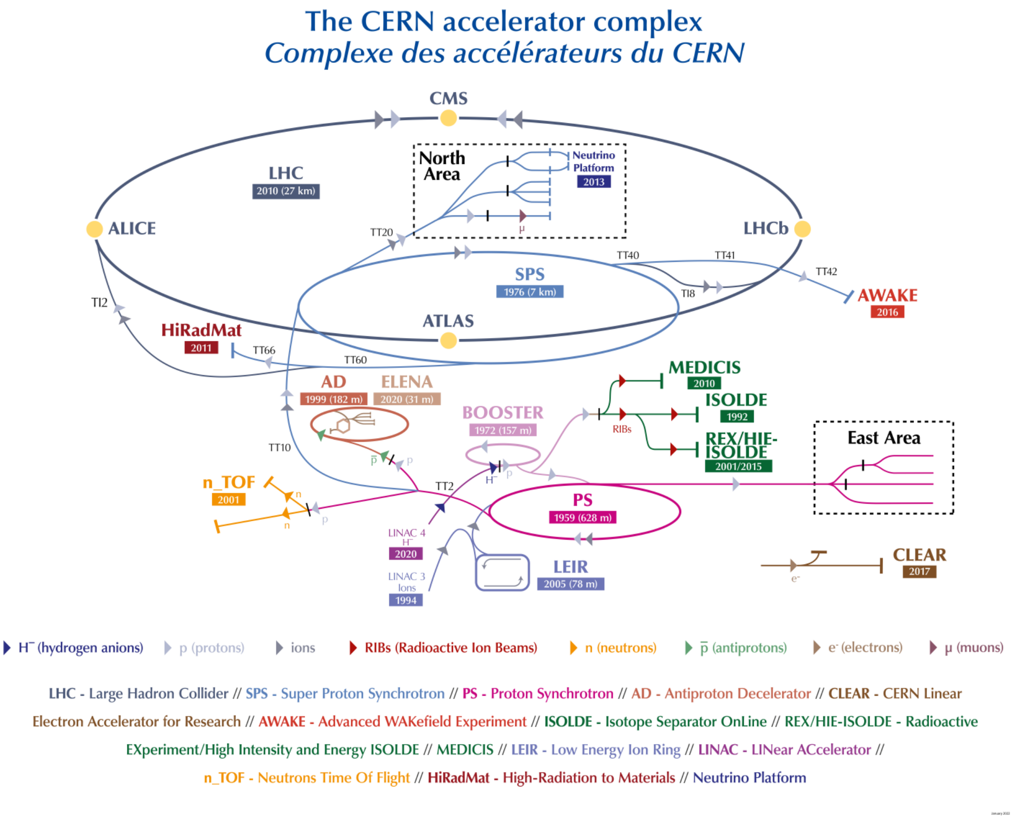

Figure 3.10: The CERN acceleration complex [66].

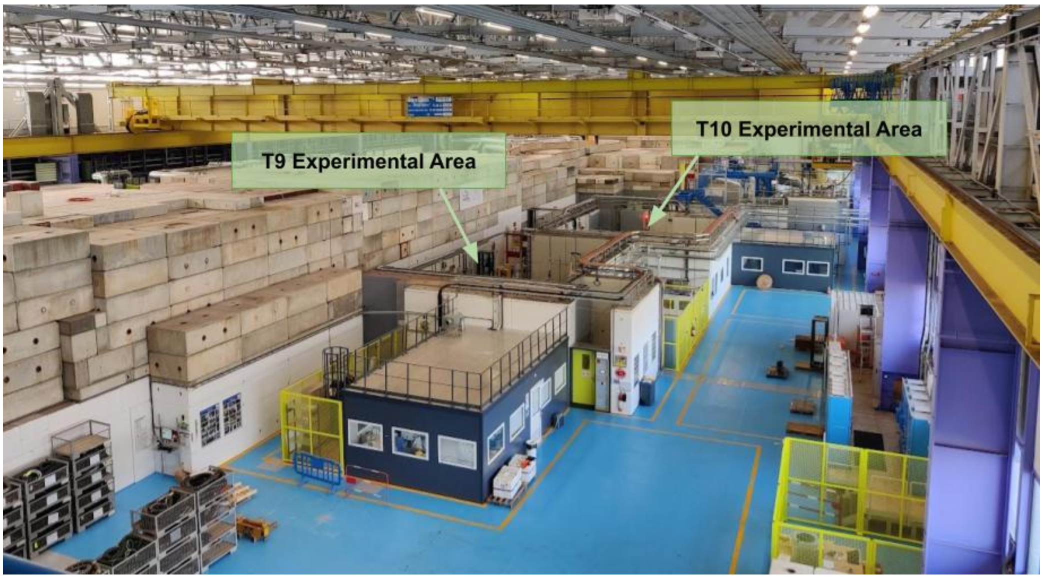

Figure 3.11: Photo of the East Area.

figure 3.10. Each machine boosts the energy of a beam of particles before injecting it into the next machine in the sequence. In the Large Hadron Collider (LHC) - the last element in this chain - particle beams are accelerated up to the record energy of 6.5 TeV per beam.

Linear accelerator 4 (Linac 4) has become the source of proton beams for the CERN accelerator complex in 2020. It accelerates negative hydrogen ions (H-, consisting of a hydrogen atom with an additional electron) to 160 MeV to prepare them to enter the Proton Synchrotron Booster (PSB). The ions are stripped of their two electrons during the injection from Linac 4 into the PSB, leaving only protons. These are accelerated to 2 GeV for the injection into the Proton Synchrotron (PS), which pushes the beam up to 26 GeV. These protons can be either extracted to the East Area Beamlines or sent to the Super Proton Synchrotron (SPS), where they are accelerated up to 450 GeV. The accelerated proton beam can be either delivered to the North Area beamlines or sent to LHC.

3.2.1 The T9 beamline

The CERN East Area (figure 3.11) is an experimental area, located in building 157, that hosts four PS extracted beamlines: T8, T9, T10 and T11, as shown in figure 3.12. In 2019, during the Long Shutdown 2 period, the East Hall experimental area underwent renovation. For more information, refer to [67].

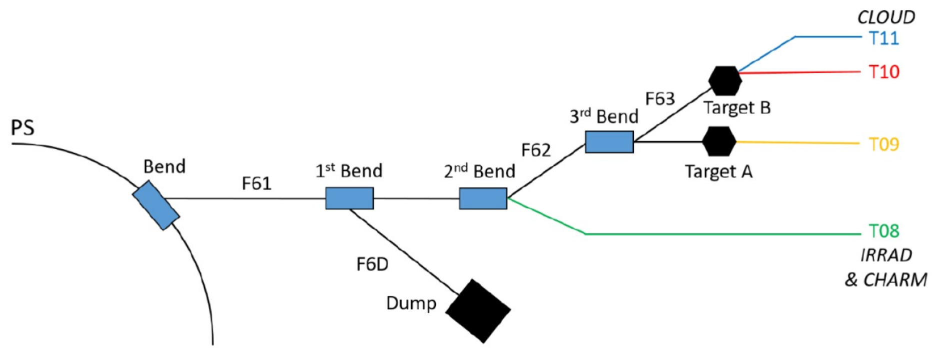

Figure 3.12: Sketch of the CERN East Area beamlines. The T9 beamline is in yellow [67].

The beams in the extracted beamlines are derived from the 24 GeV/c primary beam of the PS, which provides 2.4 second cycles with a flat top of about 400 ms. The secondary beams are produced at target B for T10 and T11 and target A for T9, with a vertical angle of 30 mrad with respect to the primary beam: this allows for a clean stopping of the primary beam into a dedicated beam dump independently of the secondary beams [67].

In particular, the T9 beam is a secondary beam that delivers secondary particles up to 15 GeV/c. The beam composition depends on the target, the selected momentum and the polarity. The negative beam contains negatively charged particles (electrons, anti-protons, pions and kaons), while the positive beam contains positively charged particles (positrons, protons, pions and kaons). Figure 3.13 shows the flux for positive and negative particles and their composition. Along their path to the experimental area, some of the pions and kaons decay, therefore there is a large number of muons entering T9.

Furthermore, it is also possible to generate a pure electron/positron beam with an energy up to 6 GeV. To achieve this, the secondary beams of charged particles are deflected using two bending magnets, leaving only the neutral γ-rays. A converter made of $2-8$ mm of lead is placed in their path to convert them into electron/positron pairs.

The T9 beamline is equipped with two threshold Cherenkov counters to obtain particle identification information for individual particles. The detectors are filled with gas: when a particle travels faster than the speed of light in that specific gas, it produces Cherenkov light, which can be detected by a photomultiplier. The gas pressure inside the detectors determines the maximum mass of the particles that emit light.

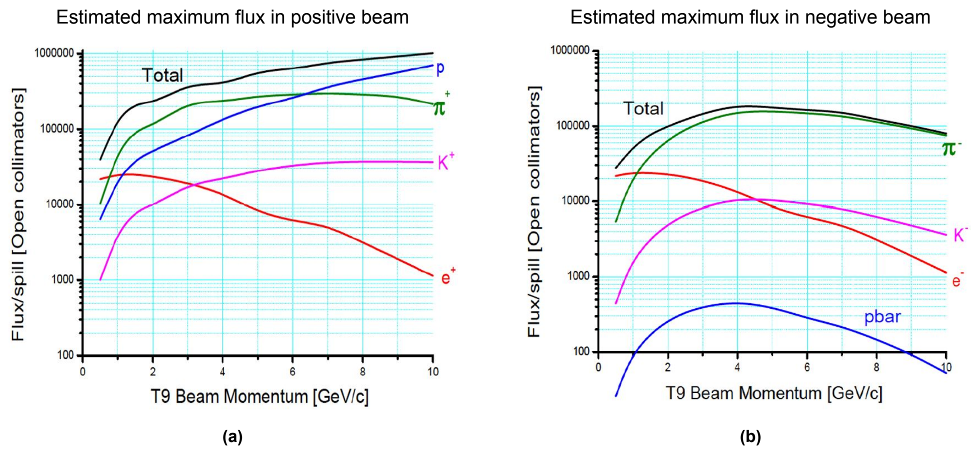

Figure 3.13: Beam composition of the positive **(a)** and negative **(b)** beam at the T9 beamline [68]. The line labeled pbar describes the flux of antiprotons. There are no muons present at this stage, but they appear when pions or kaons decay.

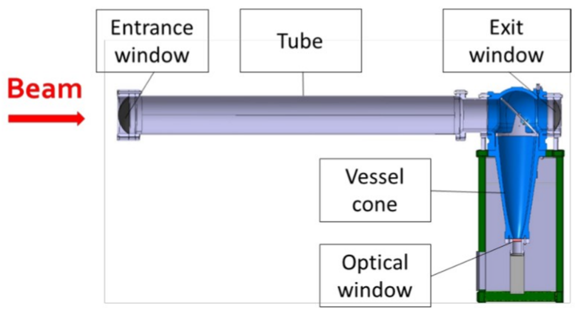

Figure 3.14: Structure of a Cherenkov counter [67].

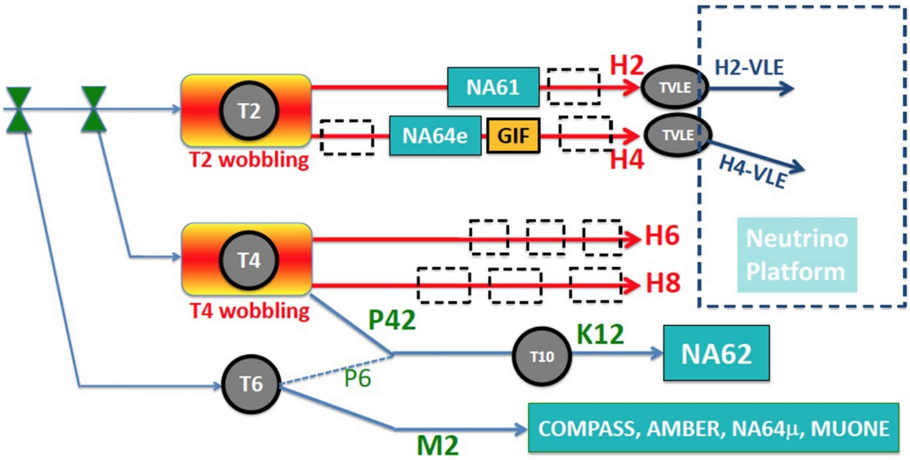

Figure 3.15: Schematic layout of the experiments and the test beam zones on the various North Area beamlines [69].

The structure of a Cherenkov counter is presented in figure 3.14: the beam enters the detector tube through an entrance window, crosses the tube filled with gas and exits through the exit window. Inside the top part of the vessel cone, also filled with gas, a mirror deflects the light towards the optical window, behind which the photomultiplier is located. The Cherenkov counters installed in the East Area line consist of a stainless steel tube approximately 3 m long with a diameter of 159 mm [67].

3.2.2 The H2 beamline

The North experimental area is located on the French site, near Prévessin. The SPS can provide proton beams up to 450 GeV/c and ion beams up to 400z GeV/c, where z represents the ion charge in units of e. A schematic layout of the North Area beamlines is presented in figure 3.15.

Protons are slow-extracted from the SPS and directed towards three beryllium targets. Different particle beams are obtained from the interactions within these targets: secondary beams are generated by capturing and manipulating particles directly emerging from the targets, while tertiary beams result from the in-flight decay of secondary particles and/or their interaction with secondary targets. Secondary and tertiary beams are delivered to the experimental areas, located in two surface halls (EHN1 and EHN2) and one cavern (ECN3). EHN1 (figure 3.16) primarily focuses on hardware R&D and small-scale physics measurements, hosting four general-purpose beamlines:

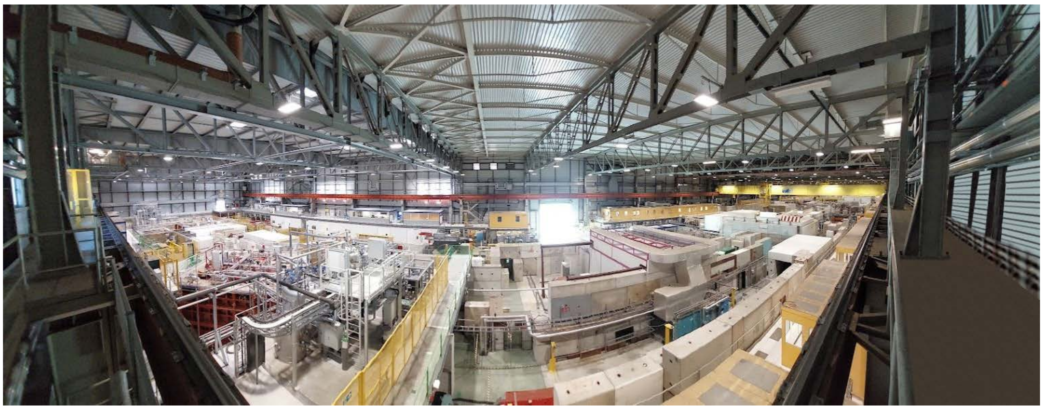

Figure 3.16: Picture of the EHN1 hall from above.

H2, H4, H6, and H8 [69].

As depicted in figure 3.15, both the H2 and H4 beamlines use secondary and tertiary beams originating from the T2 target. Specifically, in the H2 beamline, secondary beams of momentum up to 360 GeV/c are available, with a maximum momentum bit $\Delta p/p = \pm 2\%$. As far as the electron/positron beams are concerned, they are available with highly variable purity [69].

Nowadays, the H2 beamline hosts the NA61/SHINE experiment, permanently installed in zone PPE152. The PPE172 zone, shown in Figure 3.17, is dedicated to beamtests. Some of the measurements presented in this thesis were performed in this area.

3.3 Experimental setup

This section offers a comprehensive overview of the experimental setup used on both the H2 and T9 beamlines. Notably, the same elements are employed in both setups, with the additional integration of the Cherenkov counters already present on the T9 beamline. Furthermore, the individual components of the experimental apparatus are explored, highlighting their roles and contributions to the overall setup, along with a brief overview of the Data Acquisition (DAQ) system.

3.3.1 General Layout

The experimental setups for both beamlines are shown in figure 3.18. The following detectors were placed on the beamlines:

- a plastic scintillator (S) used to generate the trigger (section 3.3.2);

Figure 3.17: The PPE172 zone of the North Area H2 beamline, viewed from above. In the picture, the beam goes from right to left.

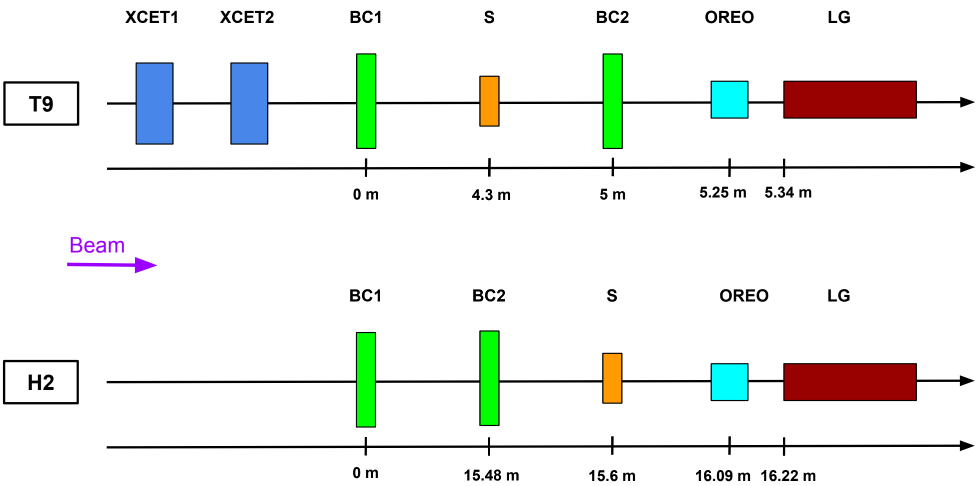

Figure 3.18: Experimental setups installed on the T9 beamline (top) and on the H2 beamline (bottom). The labeling notation is described in the text.

Figure 3.19: The trigger scintillator mounted downstream of the second beam chamber in the setup on the H2 beamline.

- two silicon chambers (BC1 and BC2) to reconstruct the incident particles trajectories (section 3.3.3);
- the OREO prototype mounted on a high precision goniometer (section 3.3.4);
- an electromagnetic Lead Glass (LG) calorimeter (section 4.4), used to measure the energy of the particles at the end of the line. The calorimeter was positioned as close as possible to the crystals in order to study the LG+OREO system. This provides a preliminary understanding of the complete OREO prototype, including the not oriented layer;
- only on the T9 beamline, two Cherenkov counters (XCET1 and XCET2, section 3.2.1) to discriminate the electrons from the other particles.

3.3.2 The trigger system

The trigger for the DAQ system was provided by a scintillator (figure 3.19) with an area of approximately $10 \times 10\,\text{cm}^2$ and a thickness of 1 cm, read out by a PMT.

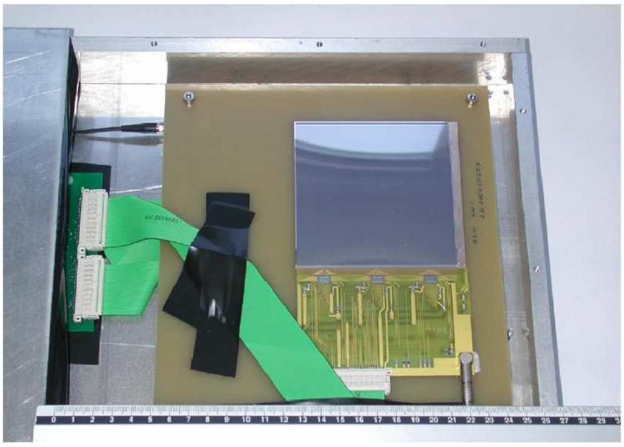

Figure 3.20: An AGILE silicon miscrostrip layer coupled to the ASICs.

For the measurements taken in both in H2 and T9, the trigger was given by the coincidence of the spill signal, which is provided by the accelerator timing system to indicate the particles arrival, and the discriminated scintillator signal.

On the T9 line, one of the Cherenkov counters was also used. The pressure of the gas was adjusted to select only electrons. The output signal was discriminated and used for triggering in coincidence with the scintillator and spill signals. Therefore, the trigger was generated by an electron crossing the scintillator. However the inefficiency of the Cherenkov counter should be taken into account. The study of the Cherenkov counters performance will be addressed in section 4.3.

3.3.3 The tracking system

The tracking system consists in two Beam Chambers (BC1 and BC2), which are large area silicon microstrip detectors based on the spare modules of the AGILE (Astrorivelatore Gamma a Immagini LEggero - Light Imager for Gamma-ray Astrophysics) satellite, a project selected by ASI (Agenzia Spaziale Italiana - Italian Space Agency) to observe γ-rays in the 30 MeV − 50 GeV range [70, 71]. The AGILE silicon detector (figure 3.20) is a single side 410 µm thick strip detector built on a 6-inch high resistivity ($\geq 4\,\mathrm{k}\Omega\,\mathrm{cm}$) substrate manufactured by Hamamatsu.

The physical strip pitch is 121 µm, while the readout pitch is 242 µm, which means that a one floating strip scheme is employed. This configuration allows to reduce the number of readout channels while ensuring a good spatial resolution thanks to the charge sharing between strips. A total of 384 strips are read out, resulting in a sensitive area of $9.3 \times 9.3\,\mathrm{cm}^2$. Guard rings and a bias ring surround the strip area, resulting in an overall dimension of $9.5 \times 9.5\,\mathrm{cm}^2$.

The detectors are AC-coupled with the frontend electronics with a coupling capacitance of 527 pF measured at 10 kHz and an AC coupling Al resistance value of $4.5\,\Omega\,\mathrm{cm}^{-1}$. The bias resistor is 40 MΩ and the typical bias value for the silicon to be fully depleted lies in the $30 - 36$ V range. The leakage current is $1.5\,\mathrm{nA\,cm}^{-2}$. The measured spatial resolution resulted to be 40 µm in a wide range of particle incidence angles [72].

Each silicon detector is interfaced with three 128 low noise and low power channels TA1 ASICs. Each channel comprises a folded cascode Charge Sensitive Preamplifier (CSA), a CR-RC slow shaper, a sample and hold circuit (S&H), and a level-sensitive discriminator. When an external trigger signal is received, a hold signal is generated to sample the signal Pulse Height (PH) at the shaper output. The readout is a multiplexed differential analog readout with a maximum clock frequency of 10 MHz.

More details on the tracking system are given in [70, 72]. Figure 3.21 shows a photograph of one of the modules used in the setup installed on the T9 beamline.

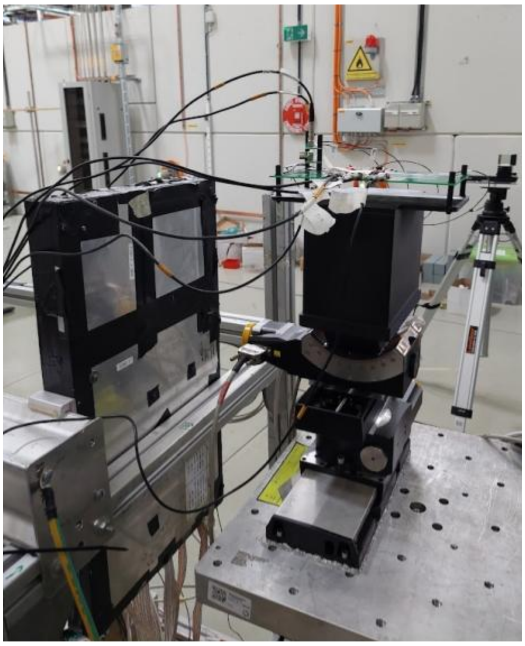

Figure 3.21: One of the modules installed in the T9 beamline in front of the goniometer with the crystal samples.

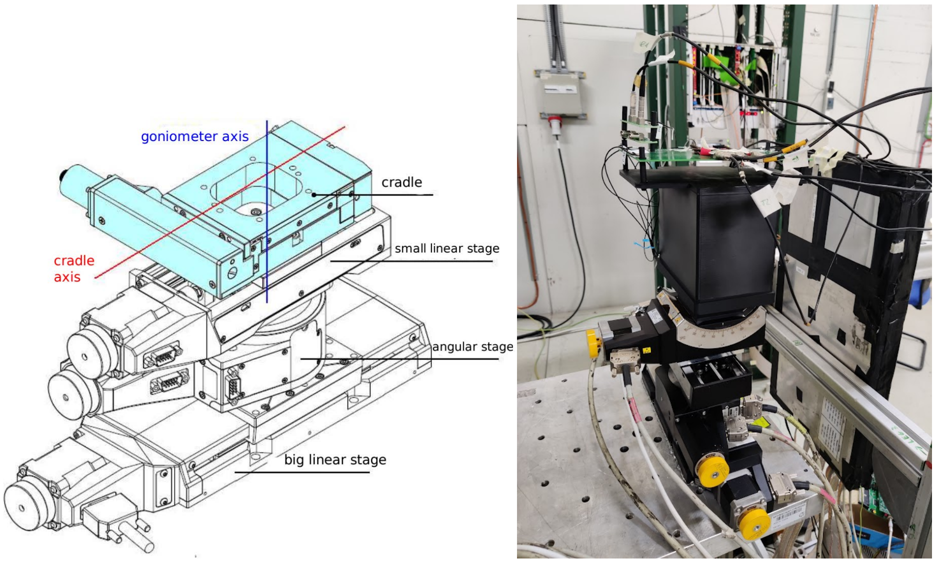

(a) (b)

Figure 3.22: **(a)** Sketch of the goniometer [73]. **(b)** Photo of the goniometer installed on the T9 beamline. On top, the holder containing the crystals and the photo detection system is mounted. The goniometer is glued on the XSCA table.

3.3.4 The goniometer

To accurately orient the crystals with respect to the incident particle beam, a high-precision goniometer system was used. The goniometer, shown in figure 3.22a, consists of different stages, manufactured by PI [74]:

- two linear stages (VT-80 and L-511) for the horizontal movement along the x direction perpendicular to the beam, with a 1.5 µm accuracy, 2 µm bidirectional repeatability and a 5 µm resolution. The range is 102 mm for the former and 52 mm for the latter;
- a rotational stage (PRS-110) to align the crystal lattice with respect to the incoming beam on the x-z plane, with an accuracy of the order of a few µrad;
- a WT-90 cradle stage to align the crystalline planes in the y-z direction. It has a maximum load of 8 kg and a precision of 1 µrad.

All the stages are connected to the DAQ computer through different controllers, such as the Corvus, the Pollux and the Mercury, all manufactured

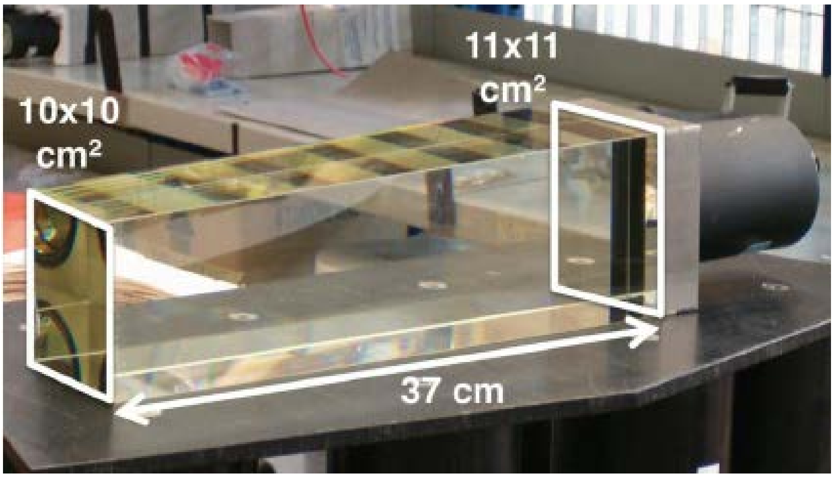

Figure 3.23: Photo of a Lead Glass calorimeter, without the cover layers [76].

by PI. Thus, the goniometer is remotely controlled by the DAQ system and the motor positions are stored in the data files and in dedicated control files. A comprehensive description of the features of the goniometer can be found in [75]. Figure 3.22b shows the goniometer installed on the T9 beamline. On both beamlines, the goniometer was installed on a remotely controlled moving platform (XSCA table) that can move in the x-y plane.

3.3.5 The Lead Glass calorimeter

The Lead Glass calorimeter, used to measure the energy of the particles at the end of the experimental setup, is one of the spare modules developed for the barrel electromagnetic calorimeter of the OPAL (Omni-Purpose Apparatus at LEP) experiment [77].

The calorimeter is made of Schott SF57 glass with 76% of lead [76] and it is covered with an aluminum foil and a cardboard layer. It has a thickness of 37 cm ($\sim 24.7X_0$) and a trapezoidal shape, with a front section measuring approximately $\sim 10 \times 10\,\text{cm}^2$ and a rear section of $\sim 11 \times 11\,\text{cm}^2$, as illustrated in figure 3.23. Electromagnetic showers in the lead glass are detected through the production of Cherenkov light, which is read out by a high voltage Hamamatsu R2238 76-mm PMT [76]. The PMT was biased in the $900 - 1000\,\text{V}$ range. Furthermore, the transverse half-size of the calorimeter measures approximately $\sim 5.5\,\text{cm}$, corresponding to $\sim 2.13R_M$, thus ensuring negligible lateral leakage.

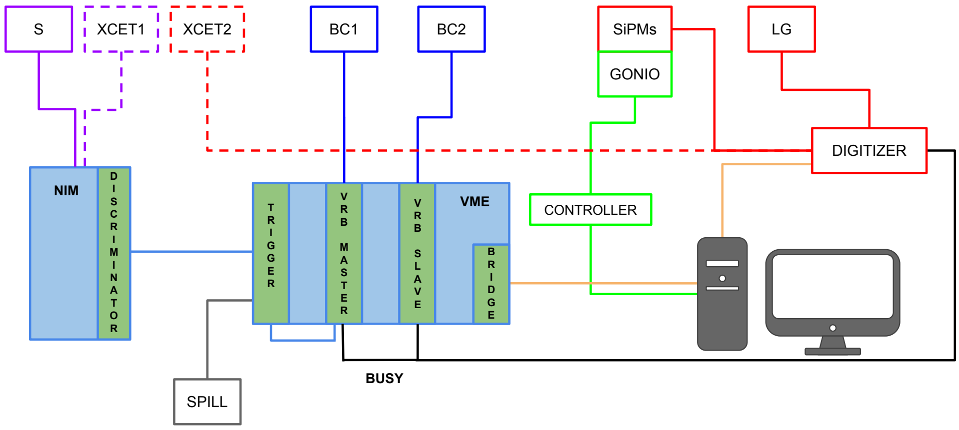

Figure 3.24: The DAQ scheme.

3.3.6 The Data Acquisition System

The data acquisition system (DAQ) is controlled by a dedicated software running on a PC with a Linux operating system. A schematic representation is shown in figure 3.24.

Each event is associated with a trigger processed by the DAQ system, generated by the logic implemented in the trigger board, and includes the information recorded by all the detectors when the trigger occurs.

A VME crate hosts the VRBs (VME Readout Boards - one per tracking module). If the system is ready when a trigger occurs, the VRB of the first beam chamber (master VRB) generates a busy signal that acts as the trigger for the slave VRB (the one for the second beam chamber) and for the digitizer (the module to read out the other light based detectors). Each VRB generates the hold signal to sample the analog strip signal at its maximum to determine the pulse height, which is digitized by the ADC (Analog to Digital Converter). Then, the VRB reads the ADC output during the spill, storing it in a dedicated RAM (Random Access Memory) and transferring it to the DAQ PC during the interspill period. The DAQ can operate in zero suppression mode, meaning that only strips above a certain threshold are stored in the RAM. In this mode, a total of 2×16 strips can be saved for each event.

The digitizer receives the trigger signal generated by the master VRB and samples the waveform of the SiPMs, the Cherenkov detector and the Lead Glass calorimeter. The waveforms are stored in the PC memory and saved during the interspill period. The DAQ software computes the maximum amplitude of the waveform and the time with respect to the trigger at which such maximum is reached. All these values are saved in the data files together with the complete waveforms.

The raw data are saved in HBOOK ntuples at the end of each spill. An offline stripping procedure, based on a FORTRAN code, first determines the number of clusters (groups of neighboring strips where the particle deposits its charge) for each silicon module. The crossing position can be reconstructed with a COG (Center Of Gravity) algorithm, which computes the weighted mean of the strips using the deposited charge as the weight. The stripping software finally saves the crossing positions for single-cluster events in ASCII files, one for each spill, along with information from the digitizer and the goniometer.

The digitizer used during the beamtests was the CAEN V1730S, which features a 14-bit resolution, a 500 MS/s sampling rate, a 0.5 and 2 Vpp selectable input dynamic range with programmable DC offset adjustment [78].

Chapter 4

Preliminary Data Analysis

To achieve a comprehensive characterization of the OREO 3×1 layer, a series of preliminary analyses are required. This chapter focuses on these initial steps, which include:

- the alignment of the silicon detectors to correct their possible physical misplacement along the line;
- the characterization of the electron beams to understand their divergence and size as a function of the energy;
- the study of the performance of the Cherenkov counters located along the T9 beamline;
- the calibration of the LG calorimeter to convert the PHs in ADC into energy deposits measured in GeV;
- the alignment of the crystals axis with respect to the particle beam, to properly study the coherent effects.

4.1 Alignment of the silicon trackers

Even if the two silicon detectors were manually aligned in the plane perpendicular to the beam axis, a small offset may still exist between them. To align the second detector to the first one, an offline procedure is needed. The particle incidence angle for each event was computed along both the x and y axes:

$$\begin{cases} \theta_x = \arctan\left(\frac{\Delta x}{\Delta z}\right) \\ \theta_y = \arctan\left(\frac{\Delta y}{\Delta z}\right) \end{cases} \tag{4.1}$$

where Δx and Δy are the differences between the hit positions measured by the second Beam Chamber and the first Beam Chamber and Δz is the distance between the modules, along the z axis. The distributions of the incidence angles were fitted with a Gaussian function and the shift parameters for the x and y coordinates were evaluated as follows:

$$shift_{x,y} = \tan(\mu_{x,y}) \cdot (z_2 - z_1) \tag{4.2}$$

where $z_2 - z_1$ is the distance between the two detectors and $\mu_{x,y}$ is the mean value extracted from the Gaussian fit of the θ_x and θ_y distributions, respectively. The shifts were then subtracted from the measured hit positions. This procedure was performed on both the H2 and T9 beamlines.

Figure 4.1 shows the incidence angle distribution both before and after the alignment procedure, with the initial distribution fitted with a Gaussian function, for the T9 6 GeV beam.

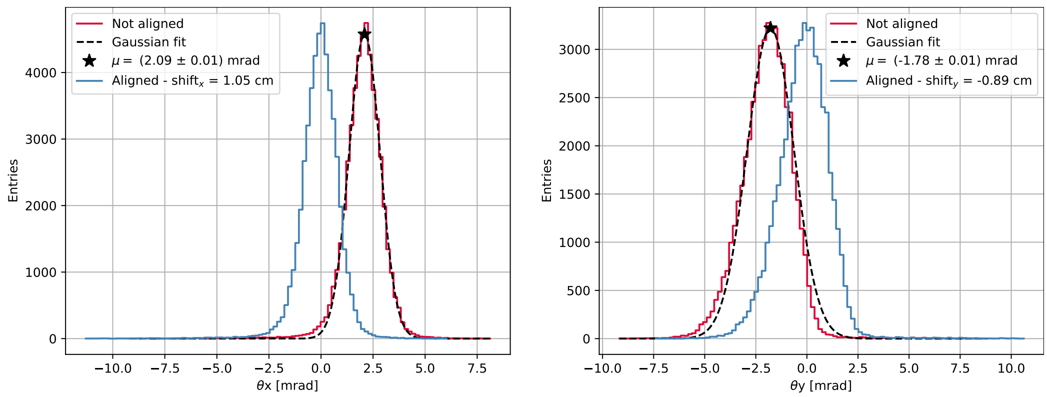

Figure 4.1: Angular distribution along the x (left) and y (right) axes of the T9 6 GeV beam, before and after the alignment procedure.

4.2 Beam characterization

The particle beams used in the beamtests were characterized to determine their size and angular divergence, observing the impact coordinates of the particles on the two silicon detectors. Figure 4.2 shows the distributions of the x and y coordinates for the two beams: the 6 GeV one (T9 beamline) and the 120 GeV one (H2 beamline). To express the beam size, the Full Width at Half Maximum (FWHM) was computed for each distribution.

Figure 4.3 presents the FWHM of the beam on the first Beam Chamber, located at the beginning of the experimental setup, for both beamlines.

Generally, the beam size decreases increasing the energy. At the T9 low energies, the beam size covers completely the three crystals. At the H2 energies, optimal positioning with respect to the beam is necessary since the beam size is smaller than the crystal dimensions. Moreover, the T9 beam was larger in the x direction because a parallel optics configuration was used to minimize the divergence in the x axis, thus increasing the beam profile. In fact, the magnets can spread the beam in only one direction, thus the x axis was chosen since the three crystals are organized in a horizontal row.

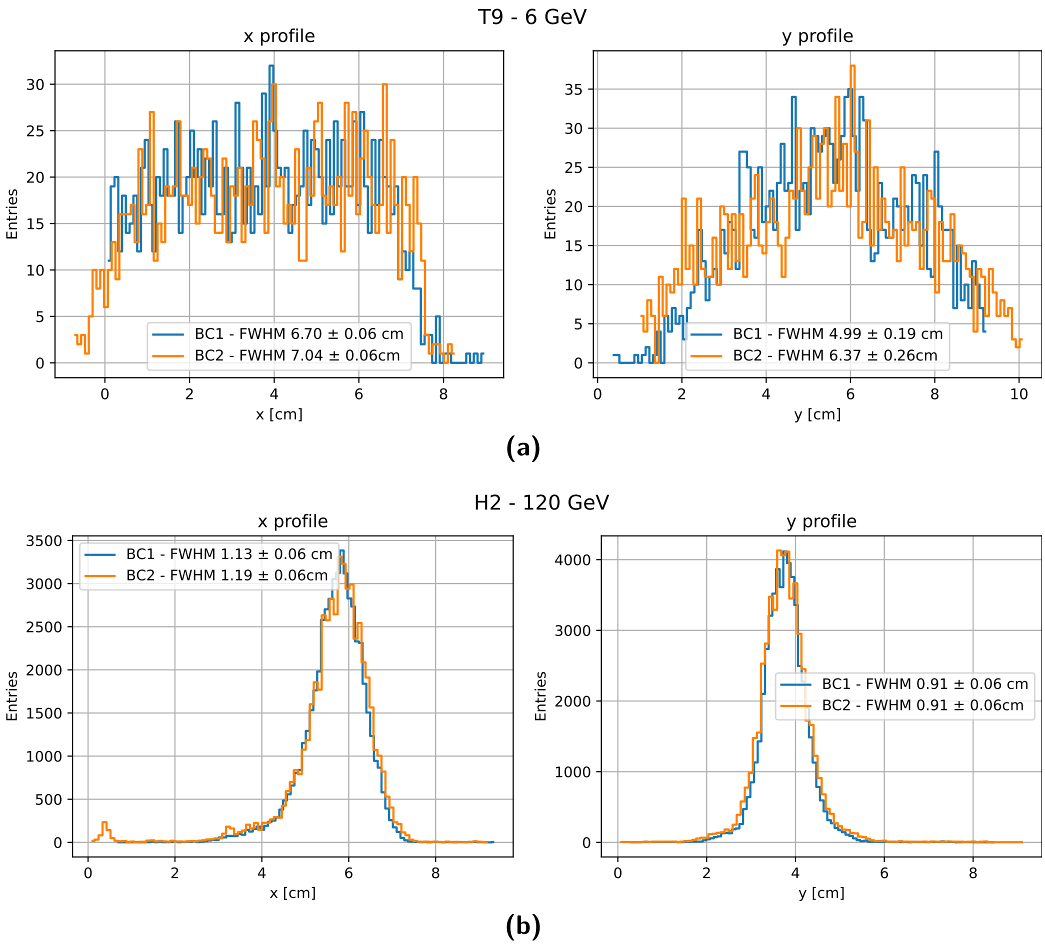

Figure 4.2: Distributions of the x (left) and the y (right) coordinates for **(a)** the 6 GeV and **(b)** 120 GeV beams.

The angular spread of the beam was evaluated using the divergence of the incidence angle distributions, computed as shown in equation (4.1) after the alignment procedure. An example is shown in figure 4.4, for the H2 and the T9 beamlines: the distribution is much narrower for the higher energy.

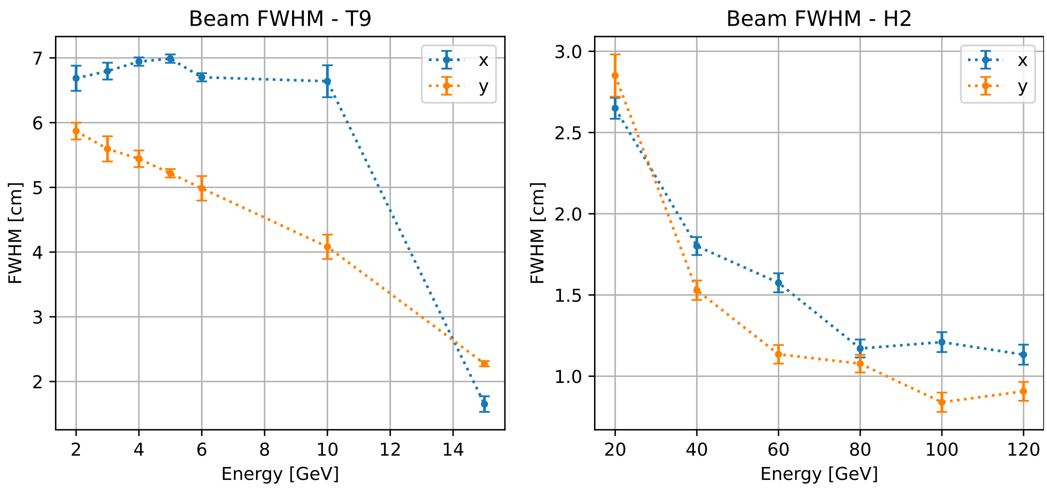

Figure 4.3: FWHM of the x (blue) and y (orange) coordinate distributions in the first Beam Chamber (BC1) for the T9 and H2 beams.

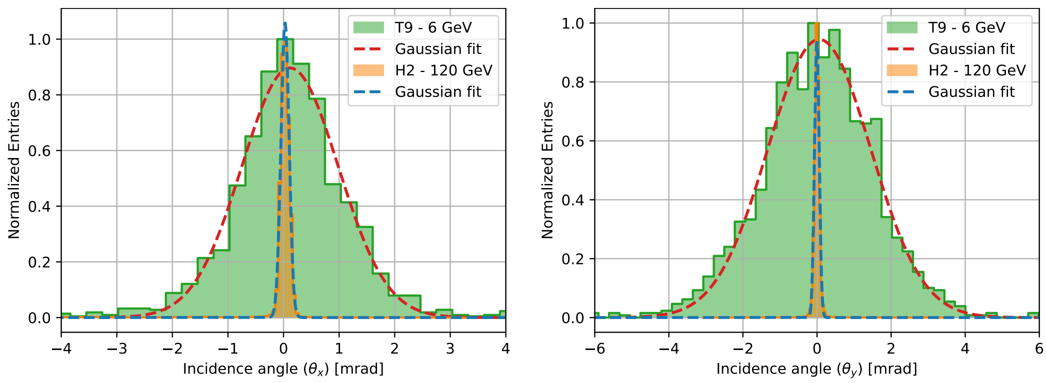

Figure 4.4: Angular distribution along the x axis (left) and the y axis (right) of the T9 6 GeV beam (green) and the H2 120 GeV beam (orange). The distributions are normalized to their respective maxima.

The distributions of the incidence angles were fitted with a Gaussian function and the beam divergence was computed as the standard deviation σ of the Gaussian. Figure 4.5 presents the angular divergence as a function of the energy for the T9 and H2 beams: the divergence decreases increasing the energy. The T9 15 GeV beam does not follow this pattern. This deviation could be attributed to the fact that the beam was obtained from a different beamline optics compared to the other beams. Phenomena such as the Strong Field effects, which strongly depend on the incidence angle, require a small beam angular divergence for accurate measurements and analysis. Specifically, the angular range for the Strong Field effects along the PWO axes is ~ 1 mrad. Notably, the beam divergence at the T9 beamline ranges approximately from 0.5 mrad to 2 mrad, while at the H2 beamline it is even smaller, up to around 250 μrad. Thus, the divergence is small enough to acquire a large statistics in a short time, given the fact that all the single track events are good ones.

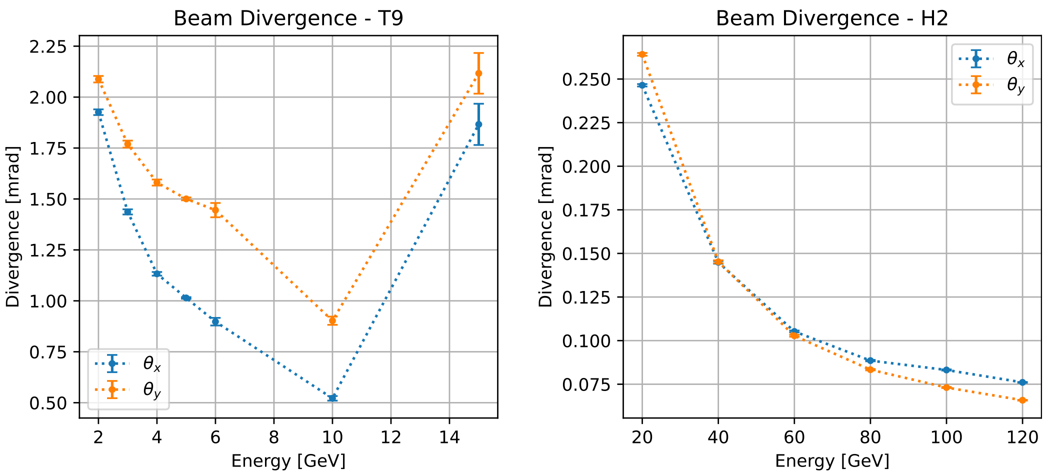

Figure 4.5: Beam divergence as a function of the energy for the T9 and H2 beams.

4.3 Cherenkov counters characterization

As mentioned in section 3.2.1, the T9 beamline is equipped with two Cherenkov counters, which allow for particle discrimination based on their gas pressure. The pressure was set so that electrons emit Cherenkov light, since they are of interest for studying Strong Field effects in crystals.

To evaluate their performance, two key quantities were taken into account:

- *purity* refers to the fraction of particles identified as electrons by the Cherenkov detector that are actually electrons. In other words, it measures how accurately the detector distinguishes electrons from other particles;

- *efficiency* refers to the fraction of incoming electrons that are identified as electrons by the Cherenkov detector.

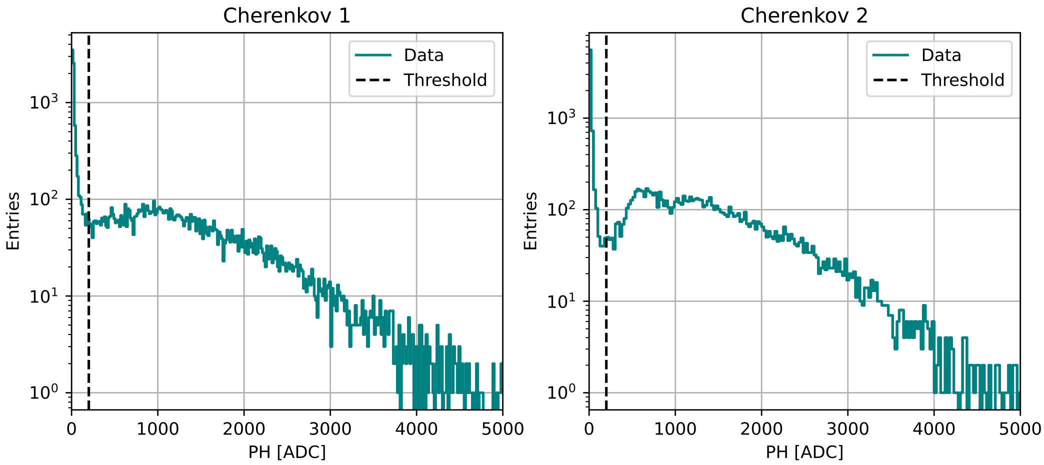

Figure 4.6: PH distribution of the two Cherenkov counters. The black lines indicate the chosen threshold.

Figure 4.6 presents the pulse height distributions of the Cherenkov counters signals. A threshold value (indicated by the black line) was chosen to distinguish between events that generated a signal in the detector and those that did not. Events with a pulse height exceeding the threshold are classified as electrons.

To identify electrons, the Lead Glass calorimeter was used as a reference detector. To ensure only particles interacting within the active area were considered, a fiducial area was defined. The particle tracks reconstructed using the silicon Beam Chamber data were projected onto the LG plane. Figure 4.7a shows a two-dimensional, pulse height-weighted histogram of the hit coordinates with the fiducial area indicated in pink. Additionally, a time cut was implemented (Figure 4.7b) to select only the particles that actually crossed the detector. Indeed, each signal peak generated by a particle occurs at approximately the same time relative to the trigger signal. The resulting pulse height spectrum after applying both cuts is presented in figure 4.8. The electron peak was fitted with a Gaussian function, and events were tagged as electrons if their pulse height was in the $(\mu - 3\sigma) < PH < (\mu + 3\sigma)$ range, where μ represents the mean value of the Gaussian and σ its standard deviation. The peak on the left corresponds to muons.

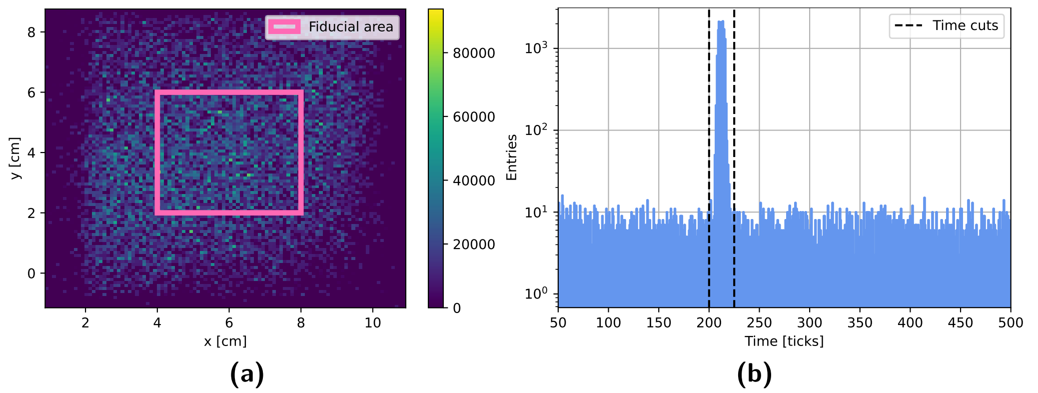

Figure 4.7: **(a)** Two-dimensional, pulse height-weighted histogram of the hit coordinates on the Lead Glass calorimeter. The fiducial area is indicated in pink. **(b)** Signal time distribution of the Lead Glass calorimeter. The events between the black lines were selected.

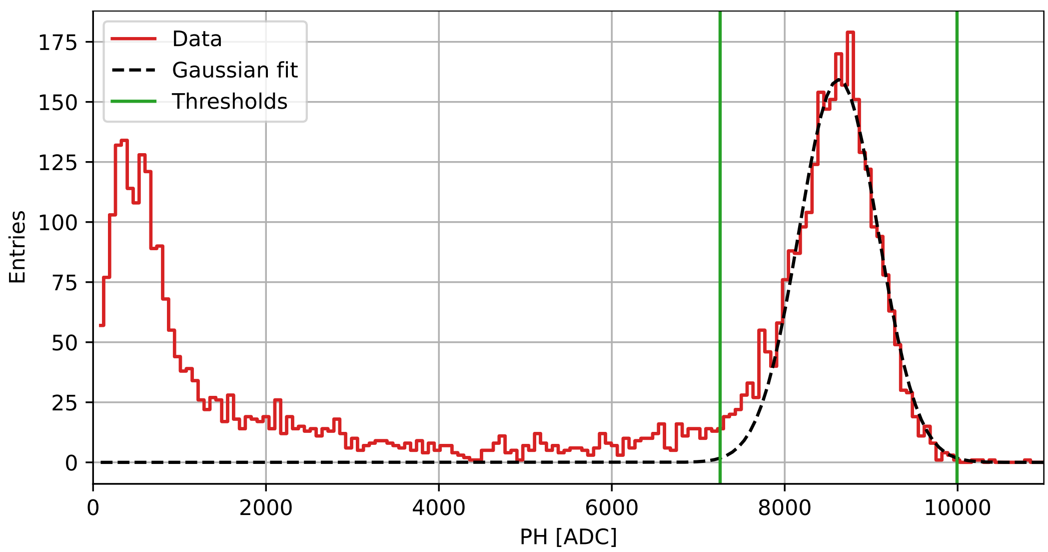

Figure 4.8: Lead Glass PH with position and time cuts. The electron peak was fitted with a Gaussian function. The green lines represent the lower and higher thresholds used to identify electrons. The peak on the left corresponds to muons.

Figure 4.9 shows the raw LG spectrum (red line) and the LG one when the Cherenkov detector registered a signal (indicating the presence of electrons). Purity was calculated as the ratio of events identified as electrons by both the Cherenkov counter and the LG calorimeter (black histogram between the green lines) and the total number of events identified as electrons by the Cherenkov counter (black histogram). Efficiency was determined by the ratio of events identified as electrons by both the Cherenkov counter and the LG calorimeter (black histogram between the green lines) and the events identified as electrons by the LG (red histogram between the green lines).

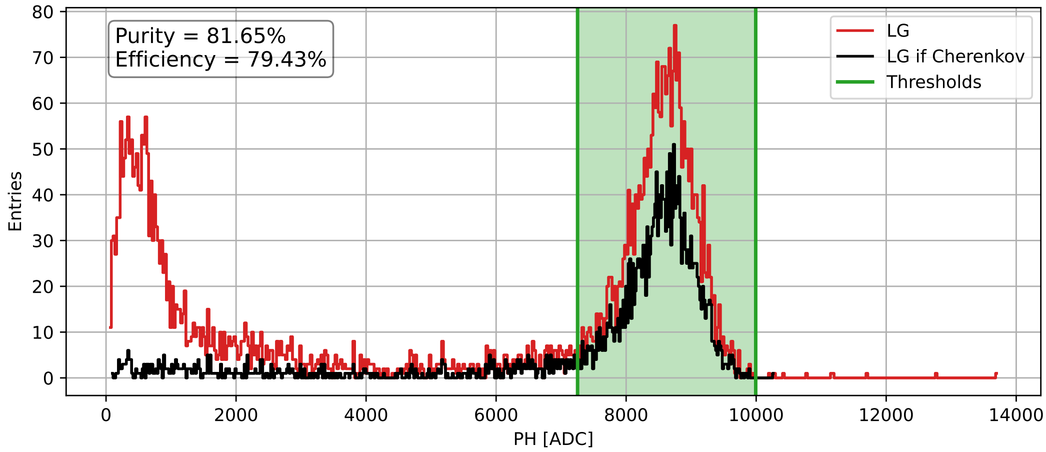

Figure 4.9: Efficiency and purity of one of the Cherenkov counters. In red, the LG pulse height distribution. In black, the LG pulse height distribution of the events above the Cherenkov threshold. The green lines indicate the threshold region used to identify electrons.

The analysis was repeated for the other Cherenkov counter and for two additional conditions:

- C1 AND C2: only events where both counters are above threshold are considered;
- C1 OR C2: events where at least one counter is above threshold are considered.

Table 4.1 presents the results: the purity does not vary significantly under the different conditions, while the efficiency increases when using the "C1 OR C2" condition, which considers electrons identified by either detector.

Table 4.1: Purity and efficiency of the Cherenkov counters for different selection conditions.

Condition	Purity	Efficiency
C1	81.65 %	79.43 %
C2	82.10 %	88.12 %
C1 AND C2	81.83 %	70.27 %
C1 OR C2	81.92 %	97.28 %

4.4 Lead Glass calorimeter characterization

To establish the relationship between the ADC counts (PHs) and the energy deposited in the calorimeter (GeV) by incoming particles, a calibration with electron beams of different energies was necessary. This procedure was performed for both the T9 and H2 beamlines. The T9 line required two separate calibrations due to the use of two digitizer ranges to acquire the Lead Glass signal: the smaller range (0.5 V) allowed for higher resolution at low energies, while the higher range (2 V) prevented saturation at higher energies.

The procedure was the following:

1. The crystals were taken out from the beam path using the goniometer and the XSCA table;

2. Maintaining the lead glass on the beam, data were acquired at different energies;

3. The PH distribution was computed at each energy. For the data acquired on the T9 beamline, cuts were applied based on position, time and Cherenkov spectra, as described in section 4.3 (figure 4.7 and 4.6). For the H2 beamline, only the time cut was applied. The fiducial area was not needed because the size of the beam was smaller than the detector one. Figure 4.10 (left) shows the PH distributions for different energies acquired on the H2 beamline;

4. For each beam energy E_{GeV}, the electron peak was fitted with a Gaussian function (figure 4.10, right), obtaining the mean value $\bar{E}$;

5. A linear regression was performed on the (E_{GeV}, $\bar{E}$) pairs, thus obtaining the straight line parameters a_0, a_1:

$$\bar{E} = a_0 \cdot E_{\mathrm{GeV}} + a_1 \tag{4.3}$$

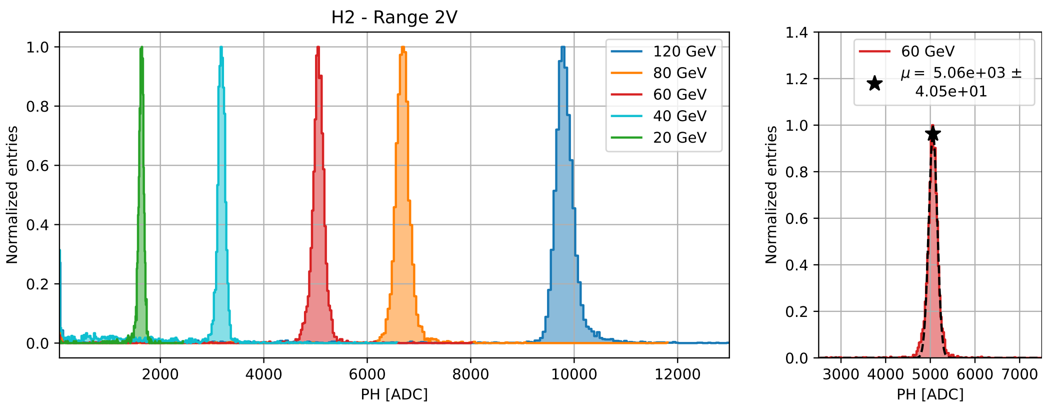

Figure 4.10: Left, pulse height spectra of the Lead Glass calorimeter at different energies acquired on the H2 beamline. Right, example of a gaussian fit of an electron peak.

Table 4.2: LG calibration coefficients for the T9 and H2 beamlines.

Beamline	Digitizer Range	a_0 [ADC/GeV]	a_1 [ADC]
H2	2 V	82.84 ± 0.46	-34.01 ± 18.34
T9	0.5 V	1303.57 ± 24.97	-96.46 ± 80.56
T9	2 V	303.77 ± 0.48	-7.33 ± 5.29

Figure 4.11 shows the calibration lines and the residuals obtained from the fit, which are found to be within 3%. The calibration coefficients are summarized in table 4.2;

6. The computed coefficients enabled the conversion of the PHs in ADC units to GeV using the equation:

$$E_{\mathrm{GeV}} = \frac{\bar{E}}{a_0} - \frac{a_1}{a_0} \tag{4.4}$$

Moreover, after converting the PHs in GeV, it was possible to compute the energy resolution, described in section 2.1. The converted spectra used for the calibration were fitted with a gaussian function, obtaining the mean value E and the standard deviation σ_E. The energy resolution was then computed as:

$$R = \frac{\sigma_E}{E} \tag{4.5}$$

The dependence of the energy resolution on the beam energy was modeled as [32]:

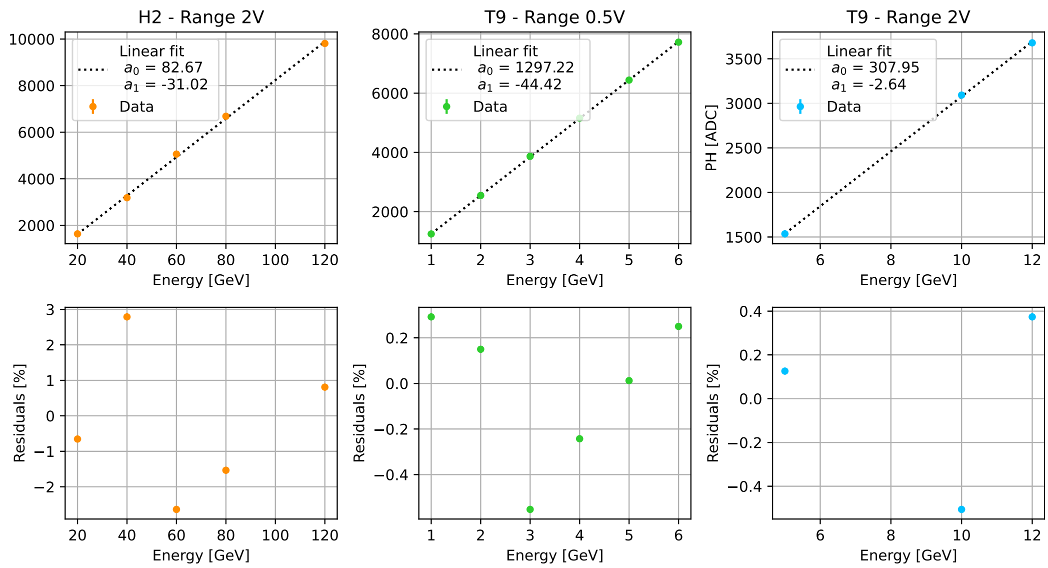

Figure 4.11: Top, Lead Glass calibration lines for the H2 (2 V digitizer range) and the T9 (0.5 V and 2 V digitizer range) beamlines. Bottom, residuals computed from the fit.

Table 4.3: LG energy resolution terms for the T9 and H2 beamlines.

Beamline	$a\,[\%\cdot\sqrt{\text{GeV}}]$	$c\,[\%]$
H2	11.00 ± 0.35	1.29 ± 0.04
T9	10.76 ± 0.27	1.63 ± 0.42

$$R = \frac{a}{\sqrt{E}} \oplus c \tag{4.6}$$

where a is the stochastic term and c the constant one. The noise term was not considered, since the LG calorimeter was readout by low-noise PMTs. The resolution curves are presented in figure 4.12 and the fit parameters are reported in table 4.3. The obtained parameters are larger than those expected for a homogeneous electromagnetic calorimeter [32]. The reason might lie in the lateral leakage of the LG calorimeter, which was found to be $\sim 6.5\%$ in [79] and thus is not negligible.

4.5 Crystals alignment

Before the characterization of the OREO prototype in the Strong Field regime, it is necessary to align the axes of the crystals with the incoming

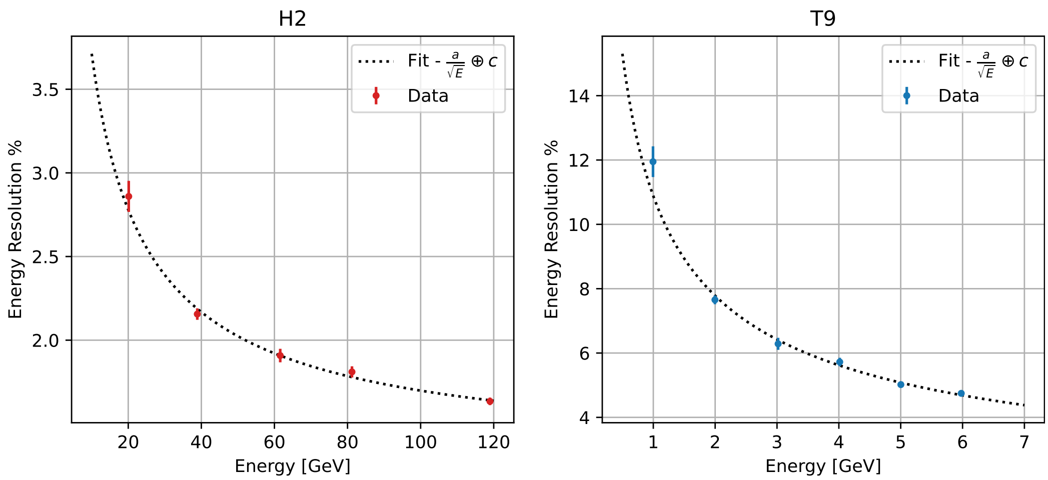

Figure 4.12: Energy resolution of the Lead Glass calorimeter, for the H2 (left) and the T9 (right) beamlines.

beam. This process is composed of two steps:

- the first is a pre-alignment and is performed without the beam, using a laser, a pentaprism and a mirror;
- the second is a more precise alignment and it is performed using the goniometer and measuring the variation of the PH of the SiPMs as a function of the beam-crystal angle.

The goal of the first step is to determine the coordinates of the stages of the goniometer which allow to align as much as possible the axis of the crystal to the beam incidence direction. For this purpose a mirror was previously installed on the crystals sample, as shown in figure 4.13, and the relative alignment of the mirror front surface with the front surface of the crystals was measured with high precision.

The pre-alignment procedure is the following:

1. An optical laser is installed in the experimental area. Using two plummets and a straight line drawn on the ground, the laser beam is aligned with the z axis (i.e. with the electron beam);
2. A pentaprism is placed along the laser beam path at the same longitudinal position as the OREO layer holder. The key feature of this instrument is that it always deflects a visible light beam by 90° (figure 4.14);
3. The crystals layer is rotated by 90° towards the pentaprism;

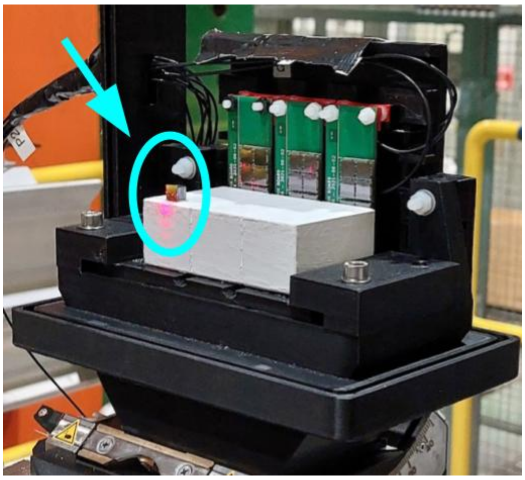

Figure 4.13: The OREO 3×1 layer on the holder installed on the goniometer in the experimental area. In cyan the mirror glued on top of one of the crystals is indicated. The laser beam impinges on the mirror.

4. The laser beam crosses the pentaprism and impinges on the mirror front face, which reflects it back across the pentaprism and towards the laser. By properly rotating the OREO layer in the $x-z$ and $y-z$ planes, the mirror is aligned along the z axis: in this condition, the incident and reflected laser beams are perfectly superimposed;

5. The sample is then rotated back by 90°, aligning the mirror perpendicularly to the incident particles beam, and by the miscut angle found as described in 3.1.1.

The pre-alignment process enables the determination of the crystal reference axis position with an uncertainty of a few mrad. This initial step is followed by a more precise alignment using the beam itself.

The alignment procedure is performed building the so-called *stereogram* [14], shown in figure 4.15. In this diagram, the coordinates represent the misalignment angles $\theta_{x,miss}$ and $\theta_{y,miss}$, as defined in equation (2.2), indicating the angles between the particle trajectory and the crystal. The origin coincides with the axis, while any crystallographic plane which crosses the reference axis is represented as a dashed straight line.

In each run with the beam, the goniometer performed a scan along either the horizontal or the vertical axis, moving the rot angular stage (θ_{rot}) or the cradle angular stage (θ_{crad}) in a predefined range. At each point of the scan, the mean PH of the SiPM coupled to the central crystal (John) was considered. If the particle beam impinges far from the crystal axis, the Standard Pair

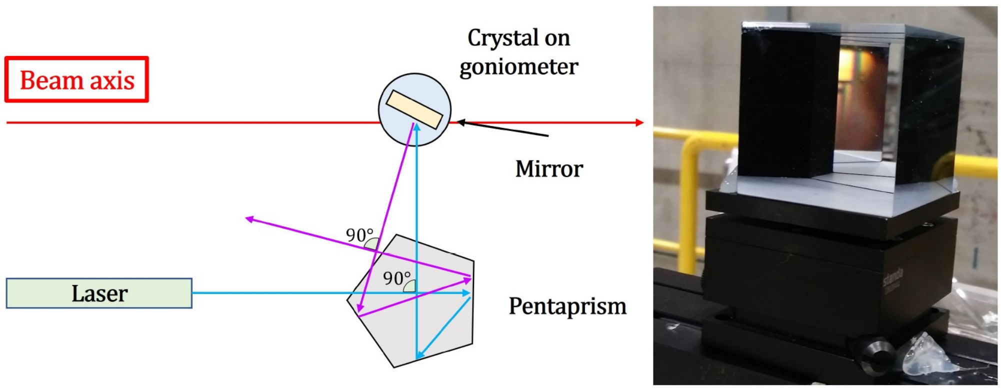

Figure 4.14: Left: schematic representation of the crystal pre-alignment process. The beam axis (z) is depicted in red, while the incident and reflected laser beams are shown in cyan and magenta, respectively. The misalignment of the crystal and the mirror with respect to the z axis results in the non-superposition of the incident and reflected laser beams. Right: photograph of the pentaprism.

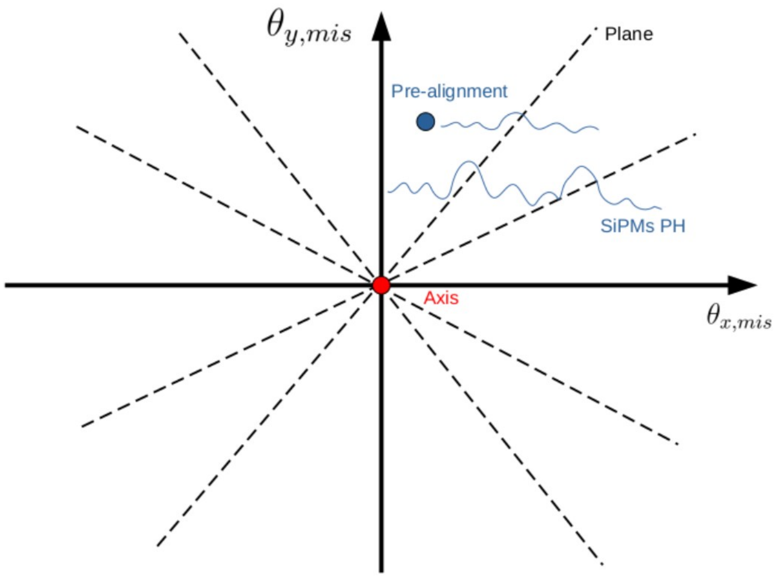

Figure 4.15: The stereogram: the abscissa and the ordinate are the $\theta_{x,\,miss}$ and $\theta_{y,\,miss}$ of the angles between the particle trajectory and the crystalline sample; the dashed black lines represent the crystallographic planes, whose intersection point is the axis (red dot) [14].

Production process takes place, resulting in a constant and very small energy deposit. As the reference axis of the crystal is approached, the electrons interact with the enhanced crystalline field and undergo coherent effects, causing the average PH of the SiPM to increase.

To compute the mean PH, several cuts were applied:

- a fiducial area within the central crystal (John) was considered, as shown in figure 4.16 (left);
- a cut based on the signal time was made;
- a selection on the beam angular divergence was performed to include only particles with a small angle, that is with a divergence within one σ of the mean value μ.

Figure 4.16 shows John PH distribution for the T9 beam with and without the cuts.

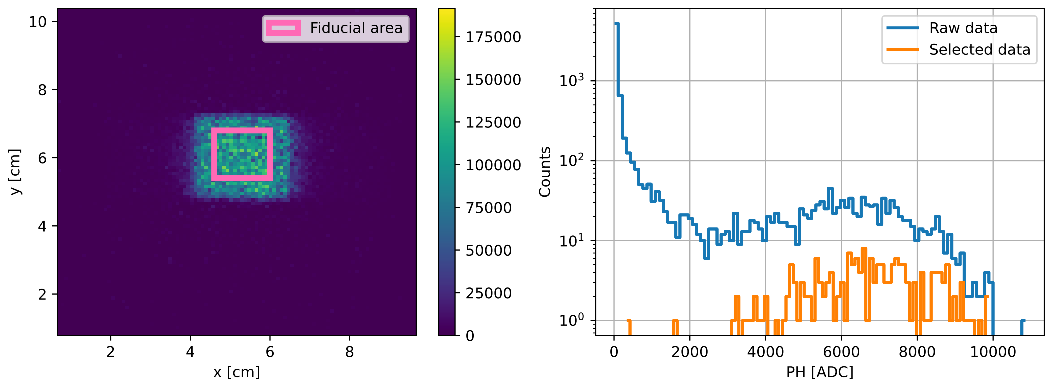

Figure 4.16: Left: two-dimensional, pulse height-weighted histogram of the hit coordinates on the central crystal (John). The fiducial area used for the mean PH calculation is shown in pink. Right: distribution of the PH values for the central crystal (John) with (orange) and without (blue) the cuts. The data were acquired on the T9 beamline.

The scans with the goniometer were used to reconstruct the crystallographic stereogram shown in figure 4.17. Each point on the stereogram represents the average John PH for a specific crystal orientation. The black circle highlights the region with the maximum average PH, which corresponds to the crystal axis.

Furthermore, it is possible to examine the average PH of the LG, positioned downstream relative to the crystal. As the coherent effects in the crystal intensify near the axis, the energy deposited in the crystal increases.

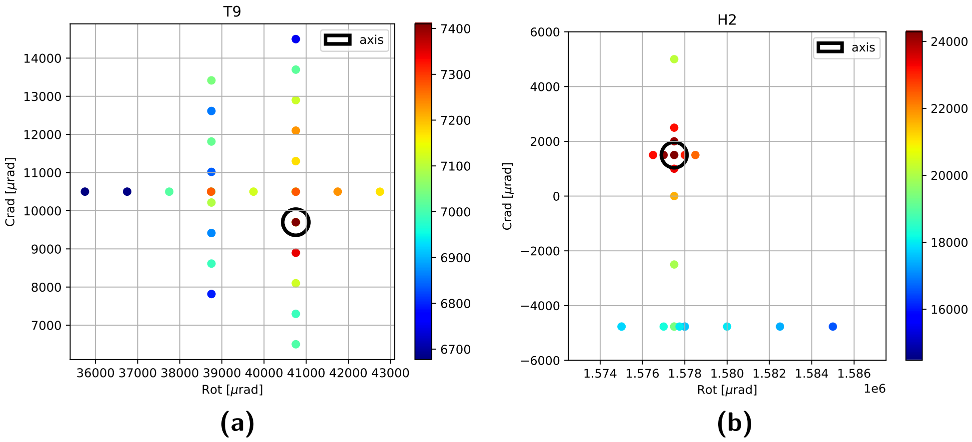

Figure 4.17: Stereogram plot obtained for the T9 (left) and H2 (right) beamline. Each point represents a rotational-cradle pair measured during the scans and its color is relative to the John mean pulse height. The black circle highlights the maximum average PH, which corresponds to the axis.

Consequently, the energy deposited in the downstream LG calorimeter decreases. For instance, figure 4.18 displays a cradle scan performed on the T9 beamline, with the rotational coordinate corresponding to the axis one. The mean PHs for John and LG, computed for each step, are respectively shown in the top and bottom plots. The cradle coordinate referring to the axis coincides with the maximum mean PH for John and the minimum for the LG, confirming the expected behavior.

The alignment of the 3×1 layer, along with the preliminary analyses and procedures presented in this chapter, allows for the detailed characterization of the OREO prototype, which will be the focus of the next chapter.

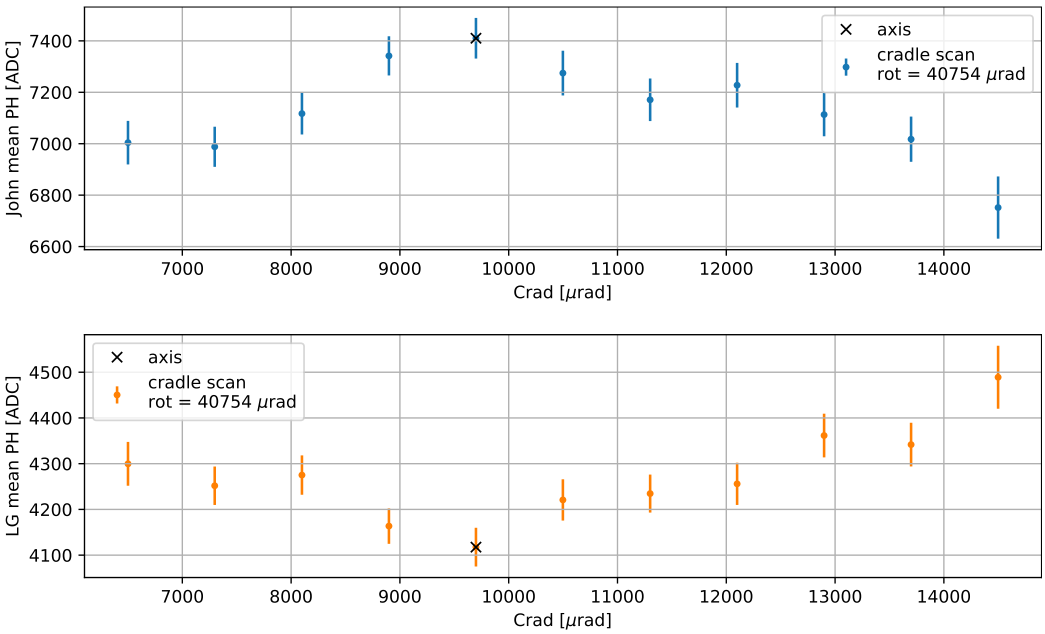

Figure 4.18: Cradle scan with the rotational coordinate fixed at the axis value. The points represent the mean PH for John (top) and for the LG (bottom) at each step of the scan. The black x marks the axis.

Chapter 5

The OREO Layer Characterization

The primary goal of the OREO 2023 beamtests was to characterize the 3×1 layer prototype consisting of three PWO-UF crystals, readout by SiPMs. This chapter presents the results obtained in the data analysis.

The first part of the chapter describes the SiPMs calibration-like procedure, to convert the SiPMs signal from ADC to GeV. Then, the enhancement of the energy deposit in the axial orientation compared to the random one is studied in three conditions:

1. in each of the the three crystals, to understand the relative alignment between them;

2. increasing the beam energy, to characterize the prototype in a large range going from low energies to the full Strong Field region;

3. at several misalignment angles between the crystal lattice and the beam.

The final part of the chapter presents a preliminary estimate of the prototype energy resolution. This estimation is achieved using the LG calorimeter to complete contain the particle shower, that is considering a two layer calorimeter.

5.1 SiPMs calibration-like procedure

To convert the SiPMs signal from ADC to GeV, it is not possible to perform a calibration as described in section 4.4 because the thickness of the crystals is too small to fully contain the shower. An alternative approach involves using Minimum Ionizing Particles (MIPs): indeed, MIPs have mean

Table 5.1: MIP energy deposit in PWO for two crystal lengths, depending on the rotation of the goniometer.

Goniometer rotation	Crystals thickness	E_{MPV}
0°	4.4 cm	44.88 MeV
90°	2.5 cm	25.50 MeV

energy loss rates close to the minimum and thus deposit the same energy per traveled unit length. For PWO, the MIP energy loss per unit length is $\varepsilon_{\mathrm{MIP}} = 10.20\,\mathrm{MeV\,cm^{-1}}$ [29]. The energy deposit can thus be computed as:

$$E_{\mathrm{MPV}} = L \cdot \varepsilon_{\mathrm{MIP}} \tag{5.1}$$

where L is the crystal thickness. The thickness of the crystals was 4.5 cm, but the goniometer allowed rotating the layer by 90°, resulting in the particles crossing 2.5 cm of PWO for each crystal. Table 5.1 presents the E_{MPV} value for the two crystal thicknesses. By measuring the corresponding energy deposit in ADC, it is possible to obtain two calibration points, thus establishing a relation between ADC and GeV.

On the H2 beamline, a 40 GeV hadron beam was available, while on the T9 beamline, a 10 GeV electron beam was used due to the small fraction of electrons at that energy. To evaluate the electron fraction, data were acquired using only the scintillator as a trigger, with the crystals removed from the beam trajectory. The Cherenkov counters were used to identify electrons with the condition C1 AND C2 and the fraction of electrons was found to be approximately 1.5%. Figure 5.1 shows the LG spectra both with and without the AND condition on the Cherenkov counters.

On each beamline, data were acquired with the goniometer set at two rotation angles (0° and 90°) and adjusting the goniometer coordinates to avoid coherent effects, ensuring that the crystals had a random orientation with respect to the beam. Since each crystal was read out by two SiPMs, the sum of their outputs was considered for the calibration.

To investigate the energy deposited by MIPs in the crystals, several cuts were applied. In order to spatially identify each crystal, the efficiency map was examined. The efficiency is defined as the fraction of detected particles relative to the total number of incident particles. To select the particles detected by each pair of SiPMs, cuts were applied based on the pulse height and time of the signal, as shown in figure 5.2. The spatial distribution of the efficiency for the T9 beamline is shown in figure 5.3, with the selected fiducial

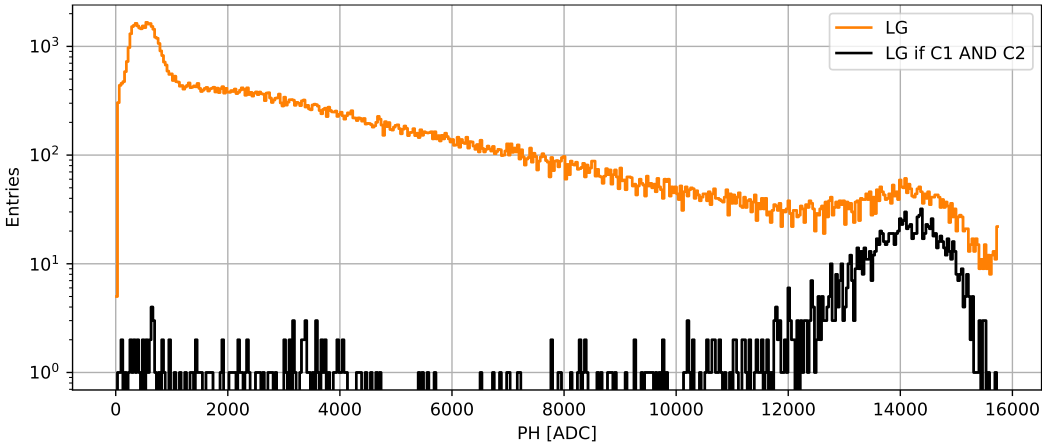

Figure 5.1: Lead Glass calorimeter spectrum using the T9 10 GeV beam (orange) and with the C1 AND C2 condition (black).

areas highlighted. To display the efficiency map of all the three crystals, an OR condition was applied among them.

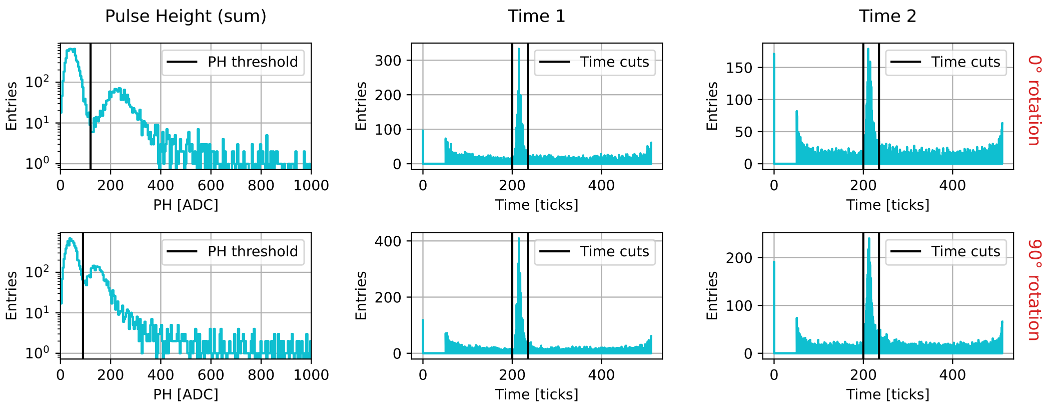

Figure 5.2: Efficiency map cuts applied for John on the T9 beamline. From left to right: sum of the two SiPMs pulse height distribution, signal time distribution of the first SiPM and signal time distribution of the second SiPM. Above, 0° rotation; below, 90° rotation. The thresholds are indicated in black.

Furthermore, cuts based on the beam divergence were applied.

The MIPs energy deposit distribution can be modeled as a Landau-like distribution, which can be described using the Moyal approximation [80]:

$$f(\lambda) = \frac{1}{\sqrt{2\pi}} e^{-0.5\lambda + e^{-\lambda}} \tag{5.2}$$

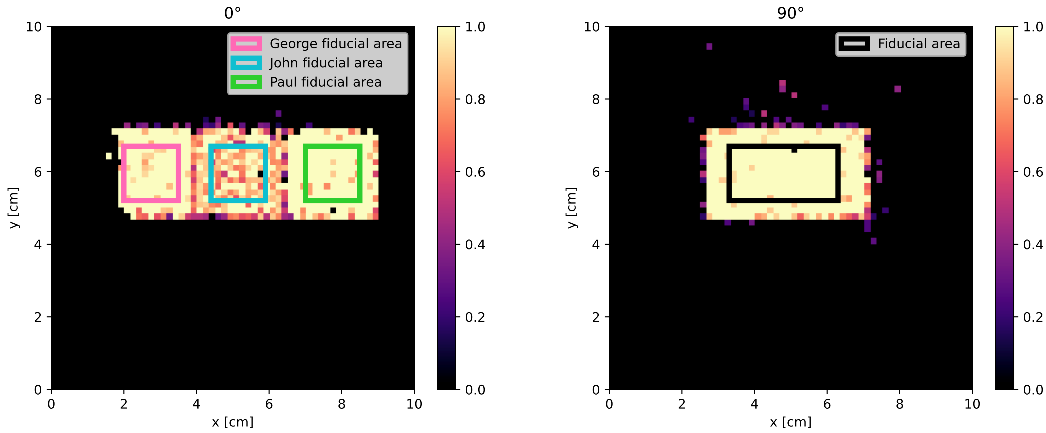

Figure 5.3: Efficiency map for the T9 beamline for two rotation angles of the goniometer: 0° (left) and 90° (right). The selected fiducial areas are indicated for each crystal.

where λ is given by:

$$\lambda = 4.02 \frac{\mathrm{PH} - \mathrm{MPV}}{\mathrm{FWHM}} \tag{5.3}$$

Figure 5.4 shows the data and the resulting fit obtained for the H2 beam, while table 5.2 presents the MPV extracted from the fit ($\mathrm{PH_{MPV}}$).

Table 5.2: (E_{MPV}, $\mathrm{PH_{MPV}}$) pairs computed for each of the three photodetectors on the T9 and H2 beamlines.

Goniometer rotation	E_{MPV} [GeV]	Detector	$\mathrm{PH_{MPV}}$ H2 [ADC]	$\mathrm{PH_{MPV}}$ T9 [ADC]
0°	$44.88 \cdot 10^{-3}$	George	103.48 ± 0.18	294.35 ± 3.57
		John	86.79 ± 0.30	218.03 ± 2.86
		Paul	103.28 ± 0.49	332.69 ± 2.45
90°	$25.50 \cdot 10^{-3}$	George	61.41 ± 0.33	163.98 ± 1.09
		John	53.60 ± 0.41	130.47 ± 1.02
		Paul	60.63 ± 0.39	183.02 ± 0.92

A linear regression was performed on the (E_{MPV}, $\mathrm{PH_{MPV}}$) pairs computed for each detector on both beamlines, as shown in figure 5.5, obtaining the straight line parameters m and q:

$$E_{\mathrm{MPV}} = m \cdot \mathrm{PH_{MPV}} + q \tag{5.4}$$

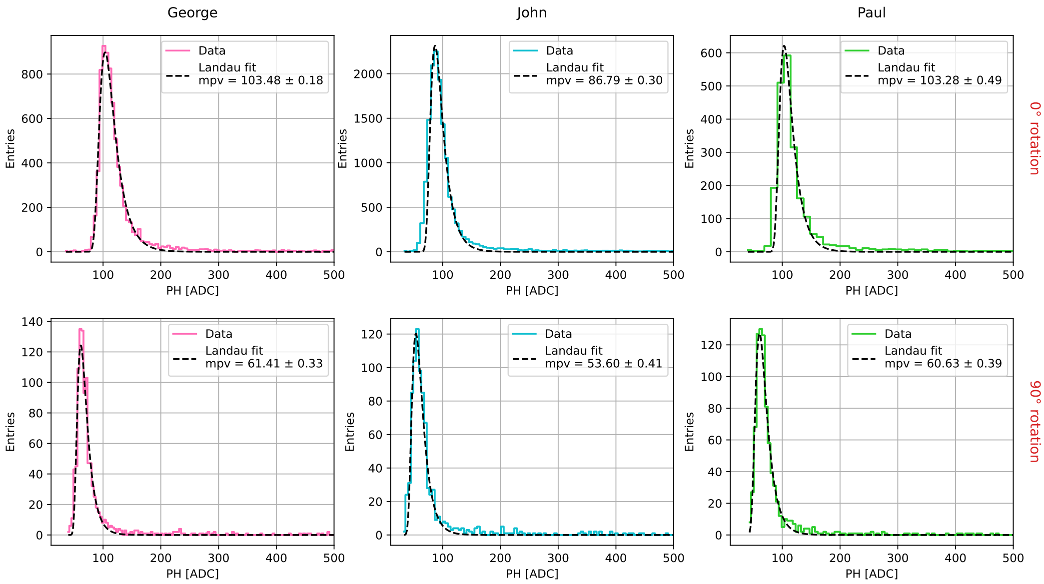

Figure 5.4: MIP peaks fitted with a Landau distribution for the H2 beam.

The calibration coefficients summarized in table 5.3 enable the conversion of PHs in ADC units to GeV using the inverse formula.

Table 5.3: SiPMs calibration coefficients obtained using the MIP peak approach.

Detector	Beamline	m [ADC/GeV]	q [ADC]
George	T9	6175.57 ± 129.69	10.92 ± 3.92
	H2	2170.58 ± 19.43	6.07 ± 0.80
John	T9	4269.33 ± 123.42	25.55 ± 3.88
	H2	1712.41 ± 26.08	9.93 ± 1.02
Paul	T9	7815.52 ± 135.57	-11.76 ± 3.92
	H2	2200.57 ± 32.37	4.52 ± 1.11

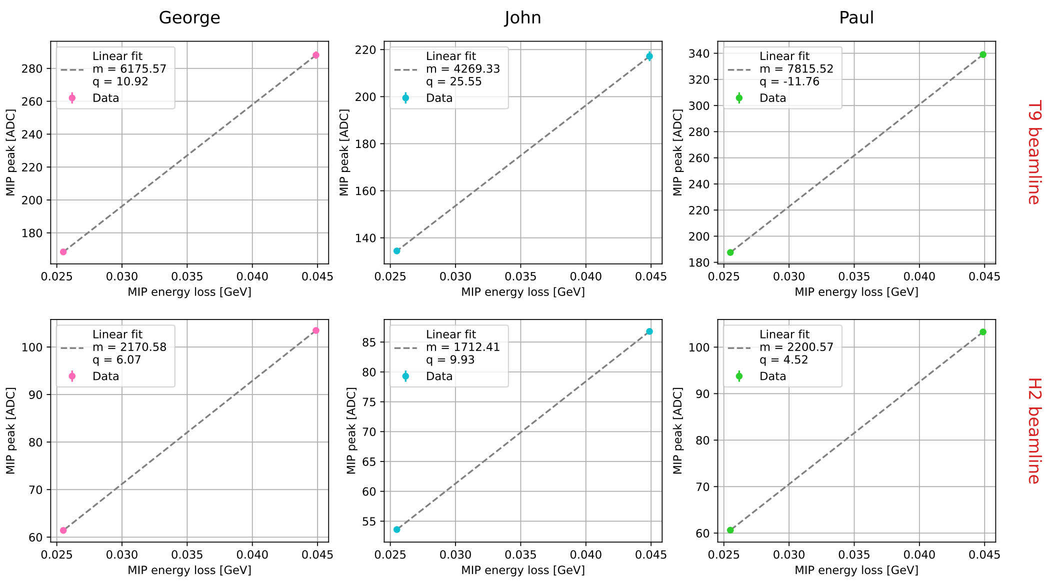

Figure 5.5: Calibration lines for the three detectors (George, John and Paul) on the T9 (above) and H2 (below) beamlines.

5.2 Crystals interalignment

A crucial step in building a calorimeter based on oriented crystals is to ensure that the different crystals are properly aligned with each other. To verify the alignment of the crystals in the 3×1 layer, the energy deposit in each crystal can be evaluated in both random and axial orientations. Specifically, the increase in radiation in the axial orientation compared to the random orientation should be consistent across all the crystals.

To study this aspect, dedicated runs were performed on both beamlines. On the T9 beamline, a 6 GeV beam was used. Due to its large size, all the three crystals could be studied simultaneously. On the other hand, the H2 120 GeV beam is smaller, so dedicated runs were performed for each crystal individually. This was done by horizontally moving the prototype with the goniometer to center each crystal on the beam.

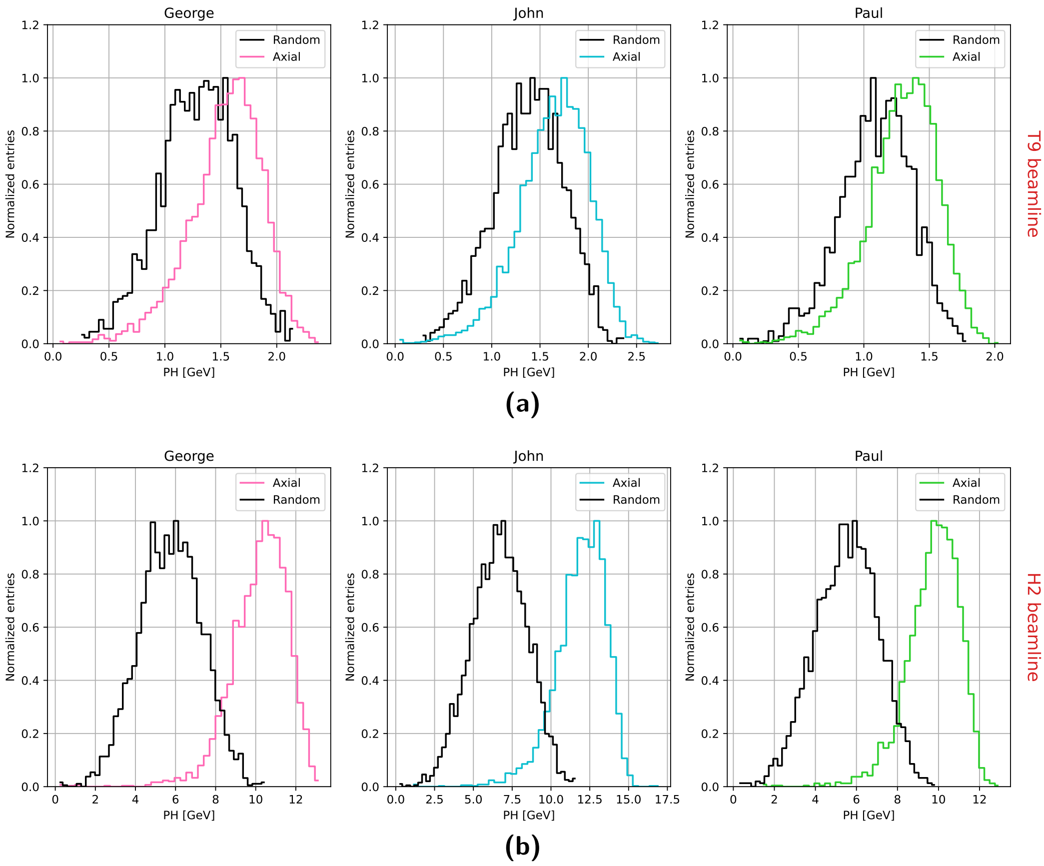

Figure 5.6: PH spectrum in axial and random orientations for each crystal, acquired with the T9 6 GeV **(a)** and H2 120 GeV **(b)** beams.

The events were selected considering the signal time, the impact position and the beam divergence. The PHs were then converted from ADC counts to GeV using the calibration coefficients determined in section 5.1. The resulting spectra are shown in figure 5.6 for each crystal.

The mean PHs were computed for each spectrum and the ratio between the axial and random orientations was calculated. The results, shown in table 5.4, indicate that the ratios are compatible, suggesting that the crystals are aligned with each other.

Table 5.4: Mean PHs in random and axial orientations, and their ratios, for each crystal, with the T9 6 GeV and the H2 120 GeV beams.

Beamline	Detector	PH_{mean} random	PH_{mean} axial	axial/random ratio
H2	George	5.746 ± 0.028	10.206 ± 0.025	1.776 ± 0.010
	John	6.660 ± 0.031	11.903 ± 0.026	1.787 ± 0.009
	Paul	5.518 ± 0.030	9.739 ± 0.025	1.765 ± 0.010
T9	George	1.284 ± 0.008	1.542 ± 0.005	1.202 ± 0.008
	John	1.378 ± 0.008	1.641 ± 0.005	1.191 ± 0.008
	Paul	1.091 ± 0.007	1.293 ± 0.004	1.185 ± 0.008

Notably, the ratios computed at 120 GeV are larger than those at 6 GeV. Indeed, the electron energy such that $\chi = 1.0$ for PWO is 31.844 GeV [73], thus at 6 GeV the Strong Field condition is not fully satisfied.

5.3 Characterization at different energies

After studying the interalignment of the crystals, the response of the 3×1 layer was analyzed at various beam energies, ranging from 6 GeV to 15 GeV on the T9 beamline and from 20 GeV to 120 GeV on the H2 beamline. For each energy, data were acquired with both axial and random crystal orientations, ensuring that the beam was centered on the central crystal (John).

Events were selected based on the signal time and the beam divergence. A fiducial area, as shown in figure 5.7, restricted the analysis to particles crossing the central crystal central region. Figure 5.8 shows the OREO and Lead Glass spectra with and without data selection for the 20 GeV H2 beam, while figure 5.9 shows the spectra of the selected events for the axial and the random orientation for the same beam. The OREO spectra were computed summing the PH of the three crystals.

After applying the cuts, the mean PHs for both the OREO and LG calorimeters were calculated at several beam energies, for both the axial and

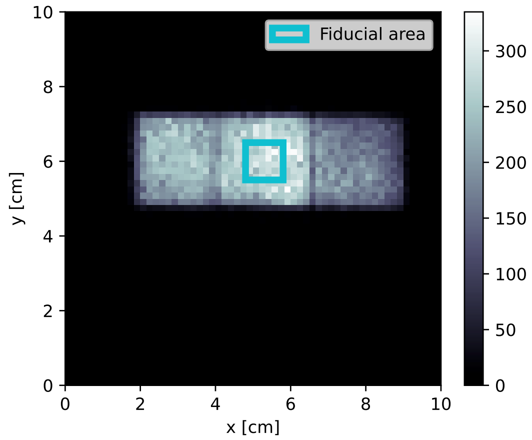

Figure 5.7: Two-dimensional histogram of the hit coordinates on the crystals, weighted by the summed PHs of all the SiPMs. The fiducial area is highlighted in blue.

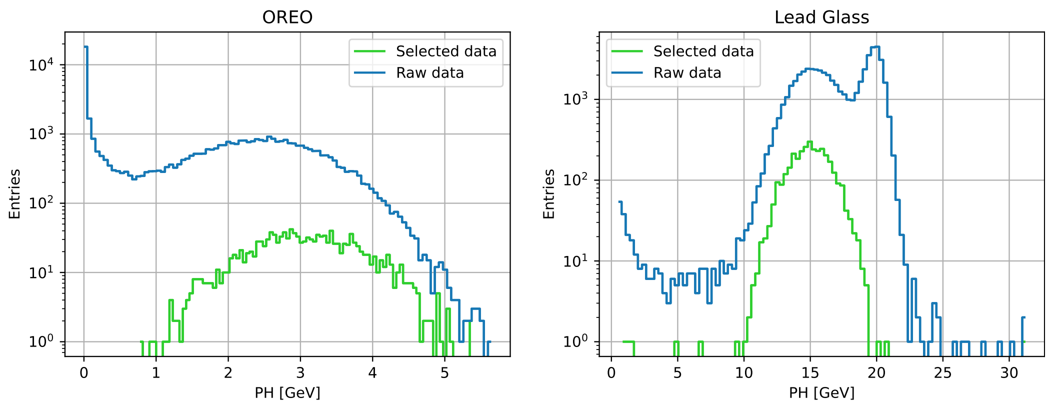

Figure 5.8: The OREO (left) and LG (right) PH spectra with (green) and without (blue) the cuts, for the 20 GeV H2 beam.

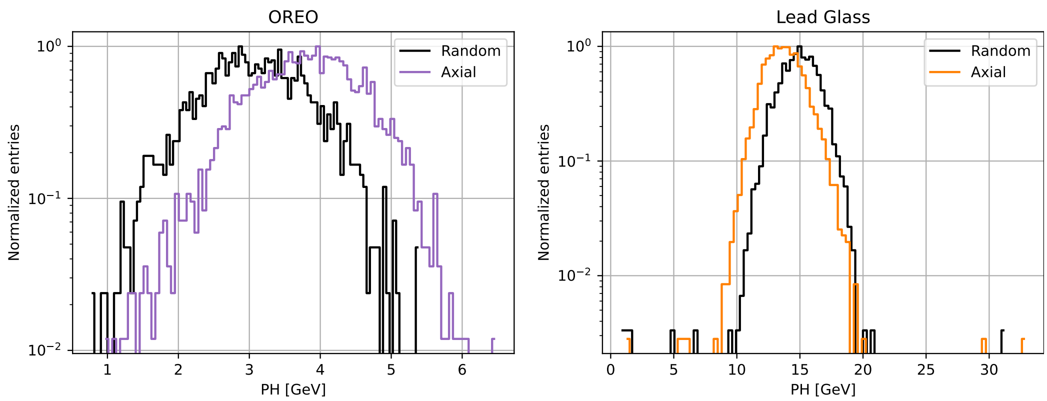

Figure 5.9: The OREO (left) and LG (right) PH spectra of the selected events, for the axial and random crystals orientation, for the 20 GeV H2 beam.

random crystal orientations. Additionally, the ratios of the OREO mean PH in the axial orientation to the mean PH in random orientation were determined for each energy. Figure 5.10 shows the results. At 10 and 15 GeV the errors are larger due to the poor statistics. The increase in the energy deposit ranges from ~ 1.15 to ~ 1.74, which is smaller compared to the results obtained with standard PWO as reported in [73]. In fact, at 120 GeV, an enhancement of ~ 2 was measured with PWO, while with PWO-UF the enhancement was approximately ~ 1.74.

Moreover, the sum of the responses of the LG calorimeter and the OREO layer was considered, applying the same cuts presented previously (figure 5.11). The two detectors were placed as close as possible in the z direction to gain a preliminary understanding of a calorimeter-like composed of a first oriented layer and a second non-oriented layer. The mean PH values were computed at each energy, as shown in figure 5.12, left. The mean energy is smaller than the beam energy. The missing energy percentage was computed as:

$$E_{\text{miss}}[\%] = \frac{E_{\text{beam}} - \bar{E}}{E_{\text{beam}}} \cdot 100 \tag{5.5}$$

where E_{beam} is the beam energy and $\bar{E}$ the mean PH. The results are shown in figure 5.12, right: a fraction of the energy is missing, ranging from $\sim 9\%$ to $\sim 24\%$. Several factors could contribute to the observed missing energy:

- the physical separation of the two detectors could result in a loss of energy in measuring the entire shower profile;
- the OREO calibration with MIPs might not fully account for the response to higher energy particles;

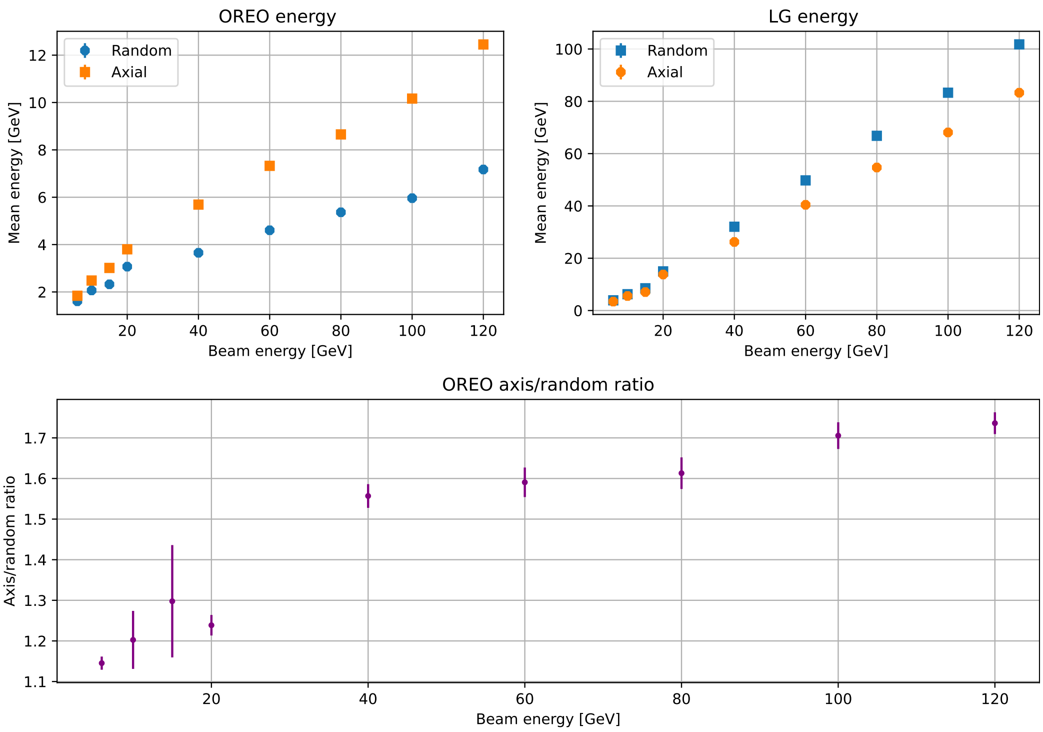

Figure 5.10: Above: OREO (left) and LG (right) mean PHs at several energies in axial (orange) and random (blue) orientation. Below: ratios of the OREO mean PHs at different energies.

- the limitations of the OREO prototype in containing the shower laterally could lead to an underestimation of the total deposited energy.

The larger difference observed in the axial orientation compared to the random one is due to the earlier shower development in the axial case, as described in chapter 1. Consequently, a greater leakage is expected due to the higher energy deposit compared to the random orientation. These aspects will be further studied in the upcoming tests involving the complete OREO prototype.

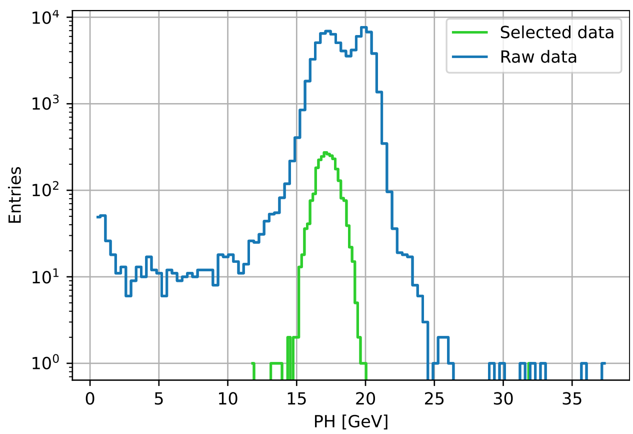

Figure 5.11: OREO + LG spectrum with (green) and without (blue) cuts.

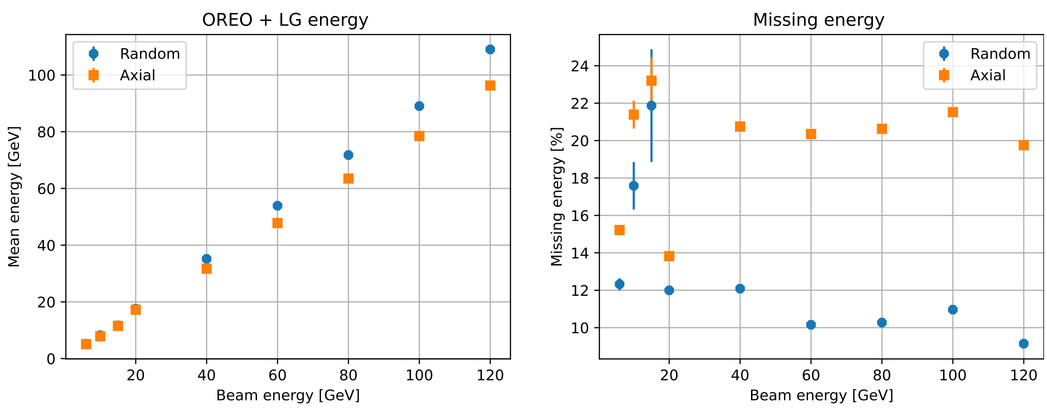

Figure 5.12: Left: OREO + LG mean PH as a function of the beam energy. Right: missing energy % as a function of the beam energy.

5.4 Angular dependence of the energy deposit enhancement

As presented in section 1.3.4, the angular range for the Strong Field regime can be estimated using the Baier angle Θ_0, which for PWO corresponds to approximately 1 mrad. This angle represents the extent of the angular range over which the enhancement of radiation by electrons/positrons and pair production by photons is maximal. However, the Strong Field effects are still measurable up to $0.5 - 1°$ of misalignment between the incident particle and the crystal axes [31].

The angular dependence of the energy deposit was studied on the T9 beamline, acquiring data with the 6 GeV beam for different misalignment angles. The events were selected following the same criteria used in section 5.3, considering only the particles crossing the center of the central crystal. At each angular step, the mean PHs of OREO and the LG calorimeter were computed and the enhancement factor was calculated by dividing these values by those obtained in the random orientation. The results are shown in figure 5.13 and in table 5.5: the enhancement factor of OREO increases as the misalignment angle approaches zero, while the calorimeter shows the opposite behavior, as their energies are anti-correlated.

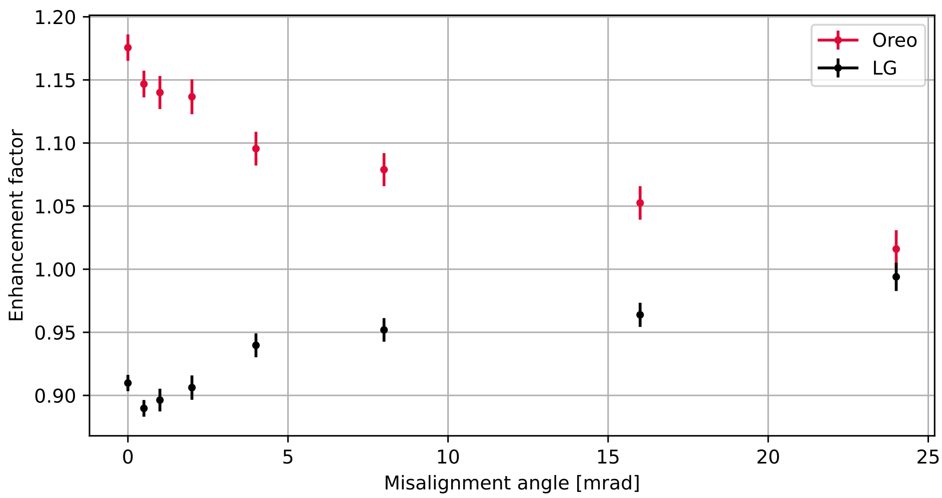

Figure 5.13: Enhancement factors of the energy deposit in the OREO prototype (red) and in the LG calorimeter (black), as a function of the misalignment angle.

Moreover, the enhancement was analyzed separately for each of the three crystals, following the same procedure. For each crystal, only the particles crossing their center were selected and their mean PHs were computed. The

Table 5.5: Enhancement factors of the energy deposit in OREO and in the LG calorimeter, computed for several misalignment angles.

Misalignment angle	Enhancement factor	
	OREO	LG
0 mrad	1.18 ± 0.01	0.91 ± 0.01
0.5 mrad	1.15 ± 0.01	0.89 ± 0.01
1 mrad	1.14 ± 0.01	0.90 ± 0.01
2 mrad	1.14 ± 0.01	0.91 ± 0.01
4 mrad	1.10 ± 0.01	0.94 ± 0.01
8 mrad	1.08 ± 0.01	0.95 ± 0.01
16 mrad	1.05 ± 0.01	0.96 ± 0.01
24 mrad	1.02 ± 0.01	0.99 ± 0.01

results are shown in figure 5.14 and in table 5.6. At each angle, the enhancement factors are compatible within $2.5\,\sigma$, confirming the interalignment of the three crystals.

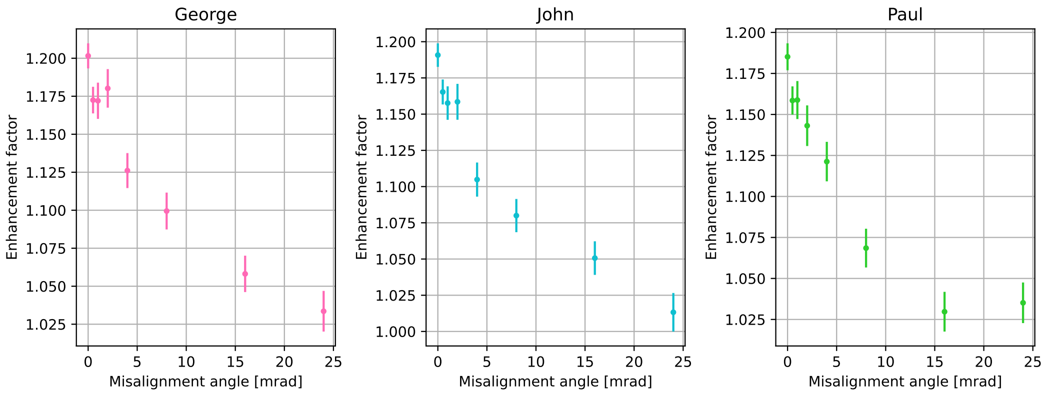

Figure 5.14: Enhancement factors of the energy deposit in the three crystals, as a function of the misalignment angle.

5.5 Preliminary energy resolution estimate

In the context of developing a compact electromagnetic calorimeter based on oriented crystals, one of the crucial parameters to consider is the energy resolution, which refers to the ability of a calorimeter to accurately measure the energy of incoming particles. In this section, a preliminary estimate of the energy resolution is presented, using the Lead Glass calorimeter as a second

Table 5.6: Enhancement factors of the energy deposit in the three crystals, computed for several misalignment angles.

Misalignment angle	Enhancement factor		
	George	John	Paul
0 mrad	1.20 ± 0.01	1.19 ± 0.01	1.19 ± 0.01
0.5 mrad	1.17 ± 0.01	1.17 ± 0.01	1.16 ± 0.01
1 mrad	1.17 ± 0.01	1.16 ± 0.01	1.16 ± 0.01
2 mrad	1.18 ± 0.01	1.16 ± 0.01	1.14 ± 0.01
4 mrad	1.13 ± 0.01	1.10 ± 0.01	1.12 ± 0.01
8 mrad	1.10 ± 0.01	1.08 ± 0.01	1.07 ± 0.01
16 mrad	1.06 ± 0.01	1.05 ± 0.01	1.03 ± 0.01
24 mrad	1.03 ± 0.01	1.01 ± 0.01	1.04 ± 0.01

layer to completely contain the particle shower. By combining the signals from the prototype and the Lead Glass calorimeter, some indications on the performance and potential improvements of the oriented crystal approach may be obtained. It must be underlined that the OREO prototype is not a calorimeter but just a row of 3 crystals. Thus the shower is surely not contained laterally.

The spectra of the combined signals of the OREO prototype and the LG calorimeter, as presented in section 5.3, were analyzed for both the axial and random orientations. Only the data acquired on the H2 beamline (i.e., from 40 to 120 GeV) were considered, due to the poor statistics of the T9 data. Each spectrum was fitted with a Gaussian function (figure 5.15), and the extracted fit parameters were used to compute the percentage energy resolution:

$$R = \frac{\sigma}{\mu} \cdot 100 \tag{5.6}$$

where μ is the mean value and σ is the standard deviation obtained from the fit.

Figure 5.16 shows the results obtained for the axial and random orientations, compared to the resolution of the LG calorimeter, determined in section 4.4 as:

$$R_{LG}(E) = \sqrt{\left(\frac{(11.00 \pm 0.35)\sqrt{\mathrm{GeV}}}{\sqrt{E}}\right)^2 + (1.29 \pm 0.04)^2} \tag{5.7}$$

The energy resolution in the axial orientation ranges from 4.36% to

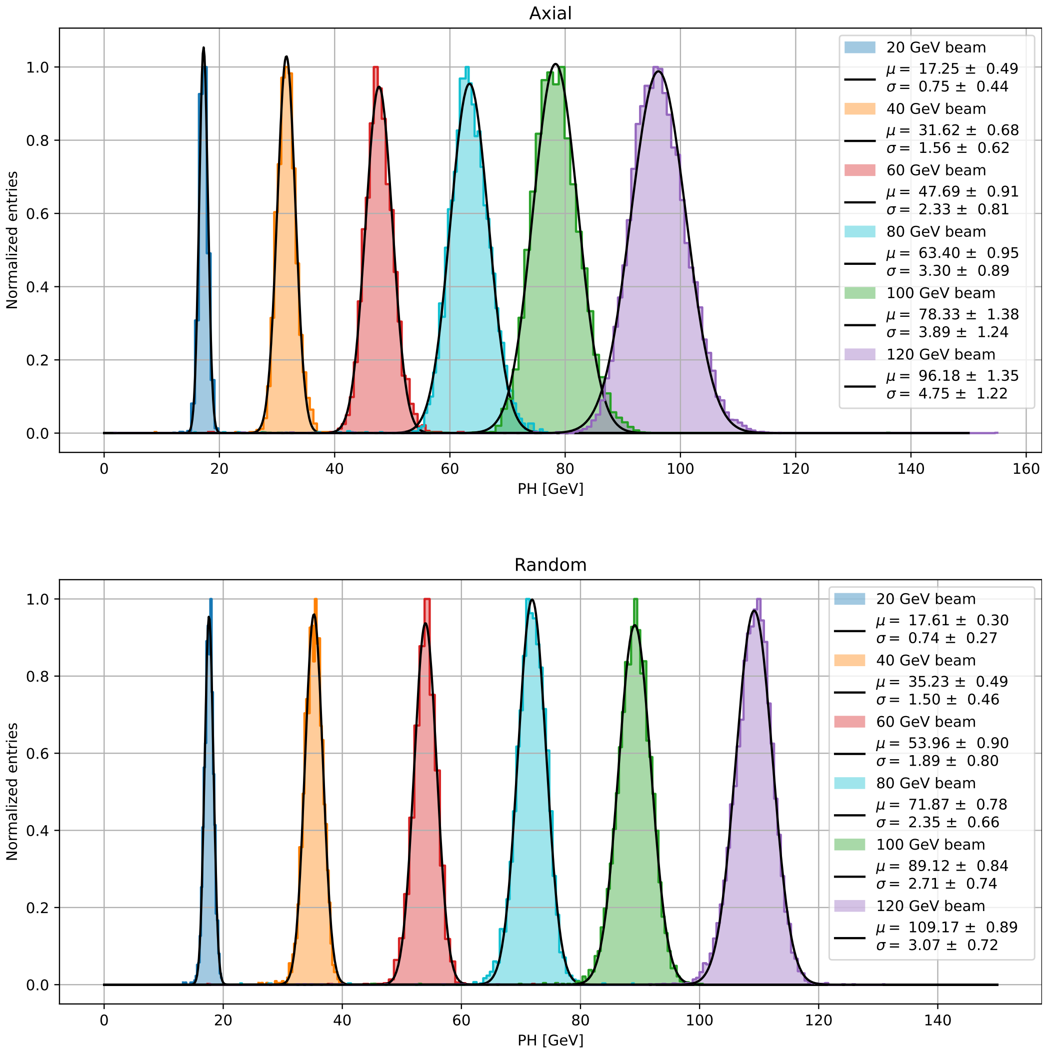

Figure 5.15: OREO + LG spectra at different beam energies, fitted with a Gaussian function, in axial (top) and random (bottom) orientation.

5.21%, while in the random orientation it ranges from 2.81% to 4.25%. The higher values observed in the axial orientation may be attributed to the larger missing energy in the combined LG and OREO system in the axial orientation compared to the random one. The quantity $\frac{\mu}{\sigma}$ was computed for the spectra of the prototype alone, although this value cannot be directly interpreted as the standard energy resolution, because the OREO prototype is not a complete calorimeter and does not contain the whole shower. The results (figure 5.17) suggest that the axial orientation might improve the energy resolution. However, the issue of the missing energy must be addressed in future feasibility tests with dedicated measurements to fully understand it.

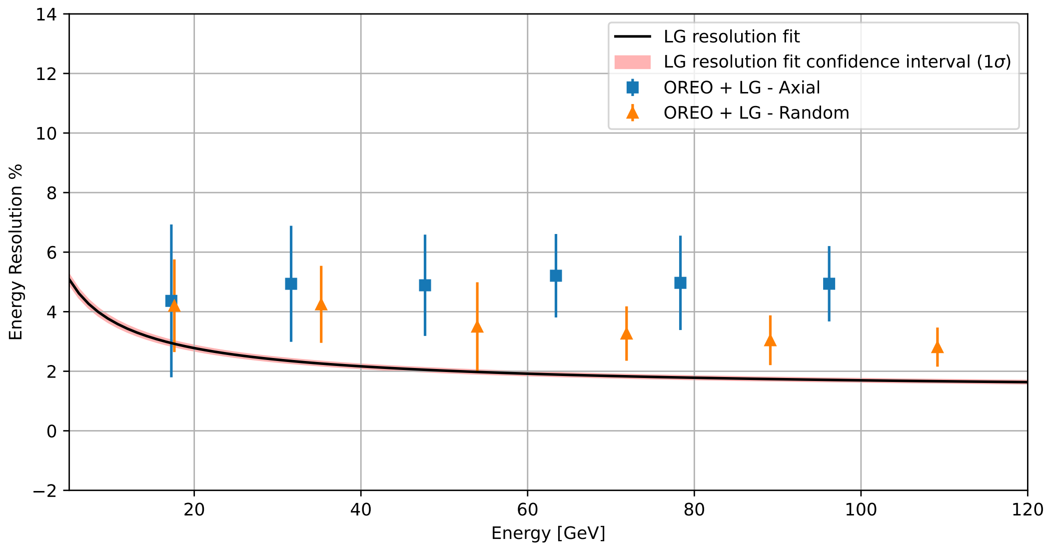

Figure 5.16: Percentage energy resolution of the LG + OREO system in axial (blue) and random (orange) orientations as a function of the mean energy. The black line represents the energy resolution fit for the LG calorimeter.

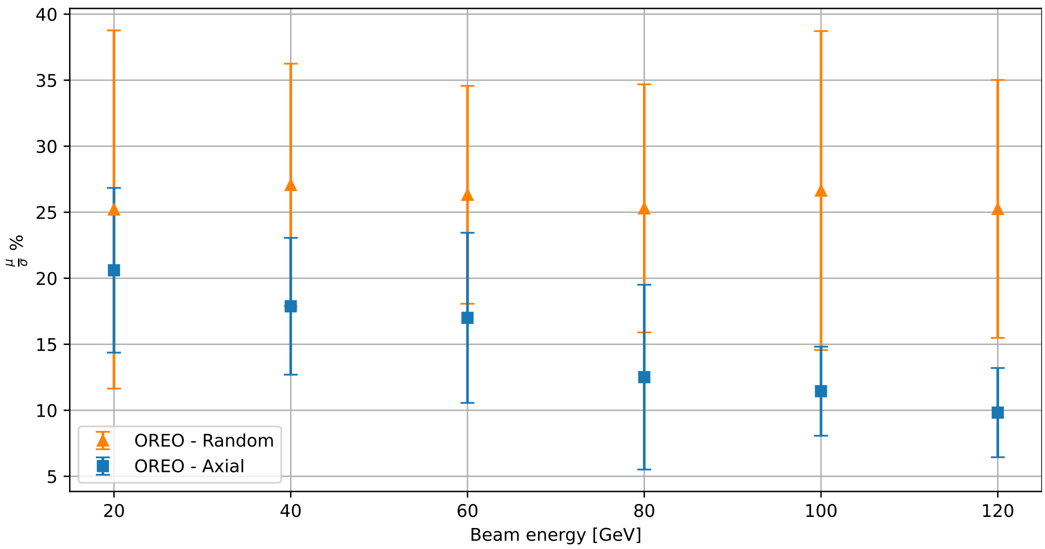

Figure 5.17: $\frac{\mu}{\sigma}$ quantity computed on the OREO spectra in random (orange) and axial (blue) orientation, as a function of the beam energy.

Conclusions

This thesis work has been performed within the framework of the INFN CSN5 OREO (ORiEnted calOrimeter) project, which aims at studying the feasibility of an innovative compact electromagnetic calorimeter based on oriented crystals.

The interaction dynamics of charged particles with a crystalline structure are influenced by the angle between the particle direction and the symmetry axis of the crystal lattice. In particular, in the Strong Field regime, both the radiation emission by electrons and positrons and the photon conversion into charged pairs are enhanced compared to the case of amorphous materials. This results in the acceleration of the electromagnetic shower development, which can be seen as a reduction of the radiation length X_0. This feature could enable the development of more compact calorimeters without compromising, and potentially even improving, their performance. Such properties are particularly advantageous for high-energy physics experiments and satellite-borne applications, where reducing the size and weight of detectors is crucial. Moreover, while the effective radiation length X_0 is influenced by the lattice orientation, the nuclear interaction length λ_I remains unaffected. This could improve the discrimination efficiency between leptons and hadrons.

The material chosen for the OREO project is Ultra Fast $PbWO_4$ (PWO-UF). PWO is one of the densest and fastest inorganic scintillators, commonly used as the active medium in homogeneous electromagnetic calorimeters. Recent studies on the luminescence of PWO have highlighted the presence of a very fast scintillation component, which can be enhanced with high precision doping techniques, achieving a decay time of approximately 640 ps. Oriented PWO-UF could combine the reduced X_0 already observed with standard oriented PWO with faster light emission. The final prototype will consist of two layers: the first layer will be a 3×3 matrix of crystals with a thickness of approximately $5X_0$ and a transverse section of $2.5 \times 2.5\,\mathrm{cm}^2$. All the crystals in this layer will be axially oriented. The second layer will be a 3×3 matrix of non-aligned crystals with a thickness of approximately $11.2X_0$ and the same transverse section as those in the first layer. The longitudinal segmentation, typically absent in scintillating homogeneous calorimeters, would be an interesting feature. Indeed, longitudinal and transverse segmentation can provide valuable information for particle identification.

This thesis focuses on testing the first OREO prototype, consisting of three crystals arranged in a 3×1 row. The main challenge of the project is the transition from single crystals to a matrix of crystals aligned with each other. Therefore, building and testing this first prototype is a crucial step in the feasibility study. The photodetection system is based on Silicon PhotoMultipliers (SiPMs) read out by custom front-end electronics, a system previously used in the STORM collaboration. The layer was tested in August 2023 at CERN, on the T9 and H2 beamlines, with energies ranging up to 150 GeV. The experimental setups on both beamlines included a plastic scintillator to generate the trigger, two silicon chambers to reconstruct the incident particle trajectories, a high-precision goniometer to accurately orient the crystals with respect to the incident particle beam, and a Lead Glass calorimeter to measure the particles energy at the end of the line. On the T9 beamline, two Cherenkov counters already in place were used to discriminate electrons from other particles.

Before characterizing the layers, the particle beams used in the beamtests were characterized to determine their size and angular divergence. The beam size was larger on the T9 beamline, completely covering the three crystals, whereas optimal positioning with respect to the beam is crucial on the H2 beamline, given that the beam size is smaller than the single crystal dimensions. The beam divergence on the T9 beamline ranges from approximately 0.5 mrad to 2 mrad, whereas on the H2 beamline, it is even smaller, around 250 µrad. This divergence is small enough to acquire a large amount of data in a short time, since the Strong Field acceptance is of the order of ~ 1 mrad.

The crystals were aligned with respect to the beam through a two-step procedure. Initially, a pre-alignment was performed without the beam, using a laser, a pentaprism, and a mirror. Then, a more precise alignment was achieved using the goniometer and measuring the variation of the SiPMs pulse height as a function of the beam-crystal angle.

Since the crystal thickness was too small to fully contain the particle shower, converting the SiPM signals to GeV was not possible using standard calibration methods. Instead, an alternative approach was employed, exploiting Minimum Ionizing Particles (MIPs) and their characteristic of depositing the same energy per unit length.

The enhancement of the energy deposit in the axial orientation compared to the random orientation was studied across the three crystals. The observed enhancements were compatible, suggesting that the three crystals were properly aligned with each other.

The energy deposit enhancement was then studied as a function of the energy considering the whole layer. The enhancements obtained with the PWO-UF prototype ranged from ~ 1.15 at 6 GeV to ~ 1.75 at 120 GeV and were smaller compared to those previously achieved with standard PWO (~ 2 at 120 GeV). Additionally, the sum of the responses of the Lead Glass calorimeter and the OREO layer was considered to gain preliminary insight into the complete prototype, composed of a first oriented layer and a second non-oriented layer. In the OREO + Lead Glass system, a fraction of the energy was found to be missing, ranging from 9% to 24%, with higher losses observed in the axially oriented case compared to the random orientation. The missing energy could stem from various factors, such as the physical separation of the two detectors, the OREO prototype lateral leakage and calibration with MIPs. Moreover, the increased missing energy observed in the axial orientation, as compared to the random orientation, can be attributed to the larger expected leakage, resulting from the earlier shower development in the Strong Field regime. This aspect requires further investigation in future tests.

The angular dependence was also studied during the transition from random to axial orientation. The enhancement was analyzed separately for each of the three crystals and for the complete prototype.

Finally, a preliminary estimate of the energy resolution was performed. In the axial orientation it ranges from 4.36% to 5.21%, while in the random orientation from 2.81% to 4.25%. The higher values observed in the axial orientation may be attributed to the larger missing energy in the combined LG and OREO system in the axial orientation compared to the random one. However, when computing the same quantity for the OREO layer alone, the results suggest that the axial orientation might improve energy resolution. It is important to note that the OREO prototype is not a calorimeter and thus does not fully contain the shower.

This thesis work has experimentally confirmed that the three crystals composing the prototype have their lattices aligned with each other and thus the technique employed to build the layer is suitable for the final prototype. A new material was tested, and despite the smaller increase in radiation compared to that obtained with standard PWO, an increase in the energy deposit and the consequent reduction in the effective radiation length were observed. The next step involves building and characterizing the complete prototype. The first test was performed in June 2024 at CERN and the preliminary results appear promising.

Acronyms

ADC	Analog to Digital Converter
AGILE	Astrorivelatore Gamma a Immagini LEggero - Light Imager for Gamma-ray Astrophysics
ALICE	A Large Ion Collider Experiment
ASCII	American Standard Code for Information Interchange
ASI	Agenzia Spaziale Italiana
ASIC	Application Specific Integrated Circuit
AXIAL	Axial and quasi-axial coherent interaction between charged particle beams and crystals
BGA	Ball Grid Array
CERN	Conseil Europeen purl la Recherche Nucleaire - European Organization for Nuclear Research
CFA	Constant Field Approximation
CMS	Compact Muon Solenoid
COG	Center Of Gravity
CSA	Charge Sensitive Preamplifier
DAMPE	DArk Matter Particle Explorer
DAQ	Data AcQuisition
DCR	Dark Count Rate
ELIOT	ELectromagnetic processes In Oriented crysTals
FCC	Future Circular Collider
FWHM	Full Width Half Maximum
HEP	High Energy Physics
INFN	Istituto Nazionale di Fisica Nucleare
LAT	Large Area Telescope
LEP	Large Electron-Positron collider
LG	Lead Glass
LINAC	LINear ACcelerator
LHC	Large Hadron Collider
$\overline{\mathbf{P}}$ANDA	antiProton ANihilation at DArmstad

MIP	Minimum Ionizing Particle
MPV	Most Probable Value
OPAL	Omni-Purpose Apparatus at LEP
OREO	ORiEnted calOrimeter
PCB	Printed Circuit Board
PDE	Photon Detection Efficiency
PH	Pulse Height
PMT	PhotoMultiplier Tube
PS	Proton Synchrotron
PSB	Proton Synchrotron Booster
PWO-UF	$PbWO_4$-Ultra Fast
QED	Quantum ElectroDynamics
RAM	Random Access Memory
S&H	Sample & Hold
SiPM	Silicon PhotoMultiplier
SPAD	Single-Photon Avalanche Diode
SPS	Super Proton Synchrotron
STORM	STrOng cRystalline electroMagnetic field
VHE	Very High Energy
VME	VERSAbus Module Eurocard
VRB	VME Readout Boards
XRD	X-Ray Diffractometer

List of Figures

List of Tables

Bibliography

[1] V. M. Biryukov, Y. A. Chesnokov, and V. I. Kotov. *Crystal channeling and its application at high-energy accelerators.* 1997. ISBN: 978-3-642-08238-2.

[2] M. T. Robinson and O. S. Oen. “Computer Studies of the Slowing Down of Energetic Atoms in Crystals”. In: *Phys. Rev.* 132 (6 1963), pp. 2385–2398. DOI: 10.1103/PhysRev.132.2385.

[3] G. R. Piercy et al. “Experimental Evidence for the Increase of Heavy Ion Ranges by Channeling in Crystalline Structure”. In: *Phys. Rev. Lett.* 10 (9 1963), pp. 399–400. DOI: 10.1103/PhysRevLett.10.399.

[4] J. Lindhard. “Influence of crystal lattice on motion of energetic charged particles”. In: *Kongel. Dan. Vidensk. Selsk., Mat.-Fys. Medd.* Vol: 34: No. 14 (Jan. 1965).

[5] E. Bøgh and E. Uggerhøj. “Orientation dependence of Rutherford scattering yields in single crystals”. In: *Physics Letters* 17.2 (1965), pp. 116–118. ISSN: 0031-9163. DOI: https://doi.org/10.1016/0031-9163(65)90265-9.

[6] J. U. Andersen et al. “An experimental study of the orientation dependence of (ρ,γ) yields in monocrystalline aluminum”. In: *Nuclear Instruments and Methods* 38 (1965), pp. 210–215. ISSN: 0029-554X. DOI: https://doi.org/10.1016/0029-554X(65)90140-0.

[7] R. L. Walker et al. “Channeling and Coherent Bremsstrahlung Effects for Relativistic Positrons and Electrons”. In: *Phys. Rev. Lett.* 25 (1 1970), pp. 5–8. DOI: 10.1103/PhysRevLett.25.5.

[8] M. A. Kumakhov. “On the theory of electromagnetic radiation of charged particles in a crystal”. In: *Physics Letters A* 57 (1976), pp. 17–18. DOI: 10.1016/0375-9601(76)90438-2.

[9] R. W. Terhune and R. H. Pantell. “X-ray and γ-ray emission from channeled relativistic electrons and positrons”. In: *Applied Physics Letters* 30.6 (1977), pp. 265–268. ISSN: 0003-6951. DOI: 10.1063/1.89379.

[10] A. H. Sørensen. “Channeling, bremsstrahlung and pair creation in single crystals”. In: *Nuclear Instruments and Methods in Physics Research Section B: Beam Interactions with Materials and Atoms* 119.1 (1996), pp. 2–29. ISSN: 0168-583X. DOI: https://doi.org/10.1016/0168-583X(96)00349-7.

[11] J. U. Andersen, E. Bonderup, and R. H. Pantell. “Channeling Radiation”. In: *Annual Review of Nuclear and Particle Science* 33.1 (1983), pp. 453–504. DOI: 10.1146/annurev.ns.33.120183.002321.

[12] N. W. Ashcroft and N. D. Mermin. *Solid State Physics*. HRW international editions. Holt, Rinehart and Winston, 1976.

[13] *The Miller Index Notation*. URL: https://www.iue.tuwien.ac.at/phd/ungersboeck/node24.html.

[14] A. Selmi. “Electromagnetic Shower Development in Oriented Crystals”. MA thesis. Università degli Studi dell’Insubria, 2020-2021. URL: https://cds.cern.ch/record/2814582.

[15] E. H. Lieb. “Thomas-Fermi and Related Theories of Atoms and Molecules”. In: *Rev. Mod. Phys.* 53 (4 1981), pp. 603–641. DOI: 10.1103/RevModPhys.53.603.

[16] J. U. Andersen. *Notes on Channeling*. Lecture Notes. Aahrus University, 2014. URL: https://phys.au.dk/fileadmin/site_files/publikationer/Lecture_notes/Channeling_notes_2018.pdf.

[17] V. Guidi et al. “Silicon crystal for channelling of negatively charged particles”. In: *Journal of Physics D: Applied Physics* 42.18 (2009). DOI: 10.1088/0022-3727/42/18/182005.

[18] V. Biryukov. “Computer simulation of beam steering by crystal channeling”. In: *Physical Review. E, Statistical Physics, Plasmas, Fluids, and Related Interdisciplinary Topics* 51.4 (Apr. 1995). DOI: 10.1103/PhysRevE.51.3522.

[19] U. I. Uggerhøj. “The interaction of relativistic particles with strong crystalline fields”. In: *Rev. Mod. Phys.* 77 (4 2005), pp. 1131–1171. DOI: 10.1103/RevModPhys.77.1131.

[20] J. U. Andersen, K. R. Eriksen, and E. Lægsgaard. “Planar-Channeling Radiation and Coherent Bremsstrahlung for MeV Electrons”. In: *Physica Scripta* 24.3 (1981), p. 588. DOI: 10.1088/0031-8949/24/3/015.

[21] M. Soldani. “Innovative applications of strong crystalline field effects to particle accelerators and detectors”. PhD thesis. Università degli Studi di Ferrara, 2023. URL: https://cds.cern.ch/record/2864634.

[22] H. Bethe and W. Heitler. “On the Stopping of Fast Particles and on the Creation of Positive Electrons”. In: *Proceedings of the Royal Society of London Series A* 146.856 (1934), pp. 83–112. DOI: 10.1098/rspa.1934.0140.

[23] J. D. Jackson. “Electrodynamics, Classical”. In: *Encyclopedia of Applied Physics*. John Wiley & Sons, Ltd, 2003. ISBN: 9783527600434. DOI: https://doi.org/10.1002/3527600434.eap109.

[24] Y. Tsai. “Pair production and bremsstrahlung of charged leptons”. In: *Rev. Mod. Phys.* 46 (4 1974), pp. 815–851. DOI: 10.1103/RevModPhys.46.815.

[25] J. Li, X. Wang, and T. Wang. “On the Validity of Born Approximation”. In: *Progress In Electromagnetics Research* 107 (2010), pp. 219–237. DOI: 10.2528/PIER10070504.

[26] J. Bak et al. “Channeling radiation from 2 - 55 GeV/c electrons and positrons ; 1, planar case”. In: *Nucl. Phys. B* 254 (1985), pp. 491–527. DOI: 10.1016/0550-3213(85)90230-5.

[27] V. N. Baier, V. M. Katkov, and V. M. Strakhovenko. “Radiation of relativistic particles moving quasiperiodically”. In: *Zh. Eksp. Teor. Fiz.* 80 (1981), pp. 1348–1360.

[28] M. Kh. Khokonov. “On the status of channeling radiation and laser based radiation sources”. In: *Phys. Lett. B* 846 (2023), p. 138208. DOI: 10.1016/j.physletb.2023.138208. arXiv: 2301.12440 [physics.atom-ph].

[29] Particle Data Group et al. “Review of Particle Physics”. In: *Progress of Theoretical and Experimental Physics* 2022.8 (Aug. 2022), p. 083C01. ISSN: 2050-3911. DOI: 10.1093/ptep/ptac097.

[30] A. H. Sørensen and E. Uggerhøj. “Channelling and channelling radiation”. In: *Nature* 325 (1987), pp. 311–318. DOI: 10.1038/325311a0.

[31] L. Bandiera et al. “A highly-compact and ultra-fast homogeneous electromagnetic calorimeter based on oriented lead tungstate crystals”. In: *Frontiers in Physics* 11 (2023). ISSN: 2296-424X. DOI: 10.3389/fphy.2023.1254020.

[32] C. W. Fabjan and F. Gianotti. "Calorimetry for particle physics". In: *Rev. Mod. Phys.* 75 (4 2003), pp. 1243–1286. DOI: 10.1103/RevModPhys.75.1243.

[33] L. Bandiera, V. Haurylavets, and V. Tikhomirov. "Compact electromagnetic calorimeters based on oriented scintillator crystals". In: *Nuclear Instruments and Methods in Physics Research Section A: Accelerators, Spectrometers, Detectors and Associated Equipment* 936 (2019). Frontier Detectors for Frontier Physics: 14th Pisa Meeting on Advanced Detectors, pp. 124–126. ISSN: 0168-9002. DOI: https://doi.org/10.1016/j.nima.2018.07.085.

[34] W. B. Atwood et al. "The Large Area Telescope on the Fermi Gamma-Ray Space Telescope Mission". In: *The Astrophysical Journal* 697.2 (May 2009), p. 1071. DOI: 10.1088/0004-637X/697/2/1071.

[35] P. Fusco and on behalf of the DAMPE Collaboration. "The DAMPE experiment and its latest results". In: *Journal of Physics: Conference Series* 1390.1 (2019), p. 012063. DOI: 10.1088/1742-6596/1390/1/012063.

[36] F. Sefkow and F. Simon. "Calorimeters". In: *Handbook of Particle Detection and Imaging*. Ed. by I. Fleck et al. Cham: Springer International Publishing, 2021, pp. 635–667. ISBN: 978-3-319-93785-4. DOI: 10.1007/978-3-319-93785-4_53.

[37] U. Fano. "Ionization Yield of Radiations. II. The Fluctuations of the Number of Ions". In: *Phys. Rev.* 72 (1 1947), pp. 26–29. DOI: 10.1103/PhysRev.72.26.

[38] W. R. Leo. *Techniques for Nuclear and Particle Physics Experiments: A How-to Approach*. Springer, 1994. ISBN: 9780387173863. DOI: https://doi.org/10.1007/978-3-642-57920-2.

[39] T. Sakuma. "Cutaway diagrams of CMS detector". In: (2019). URL: https://cds.cern.ch/record/2665537.

[40] CMS. *Energy of electrons and photons (ECAL)*. URL: https://cms.cern/detector/measuring-energy/energy-electrons-and-photons-ecal.

[41] P. Monti-Guarnieri et al. "Beam test characterization of oriented crystals in strong field conditions". In: *Proceedings of 41st International Conference on High Energy physics — PoS(ICHEP2022)*. Vol. 414. 2022, p. 342. DOI: 10.22323/1.414.0342.

[42] A. Selmi et al. "Experimental layout for the direct measurement of electromagnetic shower acceleration in an oriented crystal scintillator". In: *Nuclear Instruments and Methods in Physics Research Section A: Accelerators, Spectrometers, Detectors and Associated Equipment* 1048 (2023), p. 167948. ISSN: 0168-9002. DOI: https://doi.org/10.1016/j.nima.2022.167948.

[43] L. Bandiera et al. "Strong Reduction of the Effective Radiation Length in an Axially Oriented Scintillator Crystal". In: *Phys. Rev. Lett.* 121 (2 July 2018), p. 021603. DOI: 10.1103/PhysRevLett.121.021603.

[44] L. Bandiera et al. "Crystal-based pair production for a lepton collider positron source". In: *The European Physical Journal C* 82 (8 2022), p. 699. DOI: 10.1140/epjc/s10052-022-10666-6.

[45] G. Ballerini. "Testing coherent channeling phenomena for the K_LEVER project". Università degli Studi dell'Insubria, 2019. URL: https://cds.cern.ch/record/2674207.

[46] M. Soldani et al. "Next-generation ultra-compact calorimeters based on oriented crystals". In: *PoS* ICHEP2020 (2021), p. 872. DOI: 10.22323/1.390.0872.

[47] M. Soldani et al. "Strong enhancement of electromagnetic shower development induced by high-energy photons in a thick oriented tungsten crystal". In: *The European Physical Journal C* 83.1 (2023). ISSN: 1434-6052. DOI: 10.1140/epjc/s10052-023-11247-x.

[48] M. Soldani et al. "A high-performance custom photodetection system to probe the light yield enhancement in oriented crystals". In: *Journal of Physics: Conference Series* 2374.1 (2022), p. 012112. DOI: 10.1088/1742-6596/2374/1/012112.

[49] L. Bandiera. *Direct measurement of e.m. shower acceleration in an oriented crystal scintillator*. 15th Pisa Meeting on Advanced Detectors, 2022. URL: https://agenda.infn.it/event/22092/contributions/167346/attachments/91418/124125/Bandiera-PisaMeeting2022.pdf.

[50] A. A. Annenkov, M. V Korzhik, and P. Lecoq. "Lead tungstate scintillation material". In: *Nuclear Instruments and Methods in Physics Research Section A: Accelerators, Spectrometers, Detectors and Associated Equipment* 490.1 (2002), pp. 30–50. ISSN: 0168-9002. DOI: https://doi.org/10.1016/S0168-9002(02)00916-6.

[51] M. Follin et al. “Scintillating properties of today available lead tungstate crystals”. In: *Journal of Instrumentation* 16.08 (2021), P08040. DOI: `10.1088/1748-0221/16/08/P08040`.

[52] M. Korzhik et al. “Ultrafast PWO scintillator for future high energy physics instrumentation”. In: *Nuclear Instruments and Methods in Physics Research Section A: Accelerators, Spectrometers, Detectors and Associated Equipment* 1034 (2022), p. 166781. ISSN: 0168-9002. DOI: `https://doi.org/10.1016/j.nima.2022.166781`.

[53] D. Banerjee et al. “Dark Matter Search in Missing Energy Events with NA64”. In: *Phys. Rev. Lett.* 123 (12 2019), p. 121801. DOI: `10.1103/PhysRevLett.123.121801`.

[54] A. Bouvier. *Gamma-Ray Burst Observations at High Energy with the Fermi Large Area Telescope.* 2010. arXiv: `1012.0558 [astro-ph.HE]`.

[55] *Thoralabs.* URL: `https://www.thorlabs.com/`.

[56] Eljen Technology. *Reflective Paint EJ-510.* URL: `https://eljentechnology.com/products/accessories/ej-510`.

[57] *Zygo Corporation.* URL: `https://www.zygo.com/`.

[58] C. Piemonte and A. Gola. “Overview on the main parameters and technology of modern Silicon Photomultipliers”. In: *Nuclear Instruments and Methods in Physics Research Section A: Accelerators, Spectrometers, Detectors and Associated Equipment* 926 (2019). Silicon Photomultipliers: Technology, Characterisation and Applications, pp. 2–15. ISSN: 0168-9002. DOI: `https://doi.org/10.1016/j.nima.2018.11.119`.

[59] S. Gundacker and A. Heering. “The silicon photomultiplier: fundamentals and applications of a modern solid-state photon detector”. In: *Physics in Medicine & Biology* 65.17 (2020), 17TR01. DOI: `10.1088/1361-6560/ab7b2d`.

[60] A. Berra. “Silicon Photomultipliers in High Energy and Space Applications”. PhD thesis. Università degli Studi dell’Insubria, 2012. URL: `https://cds.cern.ch/record/1458946`.

[61] Onsemi. *ArrayC Series data sheet.* URL: `https://www.onsemi.com/download/data-sheet/pdf/arrayc-series-d.pdf`.

[62] *Onsemi, semiconductor supplier company.* URL: `https://www.onsemi.com/`.

[63] Onsemi. *C-Series SiPM Sensors data sheet.* URL: `https://www.onsemi.com/download/data-sheet/pdf/microc-series-d.pdf`.

[64] *SCEN s.r.l.* URL: https://www.scen.it/.

[65] *Hirose Electric.* URL: https://www.hirose.com/.

[66] CERN accelerator complex. URL: https://home.cern/science/accelerators/accelerator-complex.

[67] J. Bernhard et al., eds. *CERN Proton Synchrotron East Area Facility: Upgrades and renovation during Long Shutdown 2.* Vol. 4/2021. CERN Yellow Reports: Monographs. Geneva: CERN, 2021. ISBN: 978-92-9083-608-7, 978-92-9083-609-4. DOI: 10.23731/CYRM-2021-004.

[68] S. Aretz et al. "An Overview of the CERN Beamline for Schools Competition". In: *The Physics Educator* 02.01 (2020), p. 2050001. DOI: 10.1142/S2661339520500018.

[69] D. Banerjee et al. "The North Experimental Area at the Cern Super Proton Synchrotron". In: (2021). DOI: 10.17181/CERN.GP3K.0S1Y. URL: https://cds.cern.ch/record/2774716.

[70] M. Prest et al. "The AGILE silicon tracker: an innovative γ-ray instrument for space". In: *Nuclear Instruments and Methods in Physics Research Section A: Accelerators, Spectrometers, Detectors and Associated Equipment* 501.1 (2003). Proceedings of the 10th International Workshop on Vertex Detectors, pp. 280–287. ISSN: 0168-9002. DOI: https://doi.org/10.1016/S0168-9002(02)02047-8.

[71] G. Barbiellini et al. *The Agile Silicon Tracker: Architectural Design and Prototype Test Beam Results.* 2001. DOI: 10.15161/oar.it/1449011376.29.

[72] G. Barbiellini et al. "The AGILE silicon tracker: testbeam results of the prototype silicon detector". In: *Nuclear Instruments and Methods in Physics Research Section A: Accelerators, Spectrometers, Detectors and Associated Equipment* 490.1 (2002), pp. 146–158. ISSN: 0168-9002. DOI: https://doi.org/10.1016/S0168-9002(02)01062-8.

[73] P. Monti-Guarnieri. "Beamtest characterization of oriented crystals for the KLEVER Small Angle Calorimeter". Insubria U., Como, 2023. URL: https://cds.cern.ch/record/2850897.

[74] *Physik Instrumente.* URL: https://www.pionline.it/it/.

[75] W. Scandale et al. "Apparatus to study crystal channeling and volume reflection phenomena at the SPS H8 beamline". In: *Rev. Sci. Instrum.* 79 (2008), p. 023303. DOI: 10.1063/1.2832638.

[76] F. Ambrosino et al. "The large-angle photon veto system for the NA62 experiment at CERN". In: *2011 IEEE Nuclear Science Symposium Conference Record*. 2011, pp. 1159–1166. DOI: 10.1109/NSSMIC.2011.6154594.

[77] M. Akrawy et al. "Development studies for the OPAL end cap electromagnetic calorimeter using vacuum photo triode instrumented lead-glass". In: *Nuclear Instruments and Methods in Physics Research Section A: Accelerators, Spectrometers, Detectors and Associated Equipment* 290.1 (1990), pp. 76–94. ISSN: 0168-9002. DOI: https://doi.org/10.1016/0168-9002(90)90346-8.

[78] *CAEN 730S Digitizer Family*. URL: https://www.caen.it/subfamilies/730-digitizer-family/.

[79] L. Perna. "Development of compact electromagnetic calorimeters with oriented crystals: STORM 2022 beamtest". Università degli Studi dell'Insubria, 2024. URL: https://cds.cern.ch/record/2897301.

[80] J.E. Moyal. "XXX. Theory of ionization fluctuations". In: *The London, Edinburgh, and Dublin Philosophical Magazine and Journal of Science* 46.374 (1955), pp. 263–280. DOI: 10.1080/14786440308521076.